SLAC TRANS -79

PHOTOPRODUCTION OF ρ^{o}-MESONS IN A HYDROGEN BUBBLE CHAMBER AT PHOTON ENERGY LEVELS UP TO 5.8 GeV

(Photoproduktion von ρ^{o}-Mesonen in einer Wasserstoffblasenkammer bei Photonenenergien bis zu 5.8 GeV)

by

H. Spitzer

Physikalisches Staatsinstitute
II. Institut für Experimentalphysik, Hamburg

Deutsches Elektronen-Synchrotron DESY
Internal Report DESY F 1/4
November, 1967

TRANSLATED FOR
STANFORD LINEAR ACCELERATOR CENTER

Translated by
Leo Kanner Associates
Redwood City, California
January, 1968

The present study began as a dissertation within the framework of an experiment of the Aachen-Berlin-Bonn-Hamburg-Heidelberg-Munich collaboration group on the German electron synchrotron in Hamburg. The members of the collaboration group are:

U. Brall, R. Erbe, H.G. Hilpert, G. Reimann and E. Schüttler (I. Physikalisches Institut der Technischen Hochschule, Aachen);

H. Böttcher, W. Bothin, K. Lanius, A. Meyer, A. Pose and W. Schreiber (Forschungsstelle für Physik hoher Energien der Deutschen Akademie der Wissenschaften, Berlin-Zeuthen);

K. Böckmann, W. Johnssen, J. Moebes, H. Mück, B. Nellen and W. Tejessy (Physikalisches Institut der Universität Bonn and KFA Jülich, Bonn);

G. Harigel, G. Horlitz, E. Lohrmann, H. Meyer, W.P.Swanson, M.W. Teucher, G. Wolf and S. Wolff (Deutsches Elektronen-Synchrotron DESY, Hamburg);

D. Lüke, D. Mönkemeyer, D. Pollmann, W. Rau, H. Seebeck, P. Söding, H. Spitzer and W. Woidtke (Physikalisches Staatsinstitut, II. Institut für Experimentalphysik, Hamburg);

H. Beisel, H. Filthuth, H. Kolar and P. Steffen (Institut für Hochenergiephysik der Universität Heidelberg, Heidelberg);

P. Freund, K. Gottstein, N. Schmitz, P. Seyboth and J. Seyerlein (Max-Planck-Institut für Physik und Astrophysik, Munich).

ABSTRACT

The photoproduction of ρ^o-mesons has been investigated at photon energies from threshold up to 5.8 GeV with the help of the 85-cm hydrogen bubble chamber at DESY. About 8400 reactions of the type $\gamma p \rightarrow p\pi^+\pi^-$ were analysed in 640,000 pictures; ρ^o-production is the dominant process in this reaction above 1.1 GeV.

Results on the total cross sections, differential cross sections and decay matrix elements are given for various photon energy intervals. The total cross section rises above threshold to 20 μb and falls slowly to about 16 μb at 5 GeV. The magnitude and the energy dependence of the total cross section are successfully explained by a combined vector-dominance and quark model.

The forward differential cross section at 4.5 GeV agrees with the results of Crouch et al. [2] but not with the work of Lanzerotti et al. [3]. Both the cross sections and the decay distributions indicate a mainly diffractive production mechanism.

At high energies the ρ peak is distorted and shifted to low mass values. These features are explained by the interference of a resonant ρ amplitude with a coherent Drell-type background as proposed by Söding.

We find several effects of the interference, e.g. a strong variation of the diffraction slope with the invariant $\pi^+\pi^-$ mass near the resonance and a dependence of the ρ mass distribution on the production angle.

In the first part (section II) of this work we describe the experimental procedure in detail. In the second part (section III) we present the results on ρ-production and give a short discussion. The appendix contains a description of the fitting procedure applied. The reader mainly interested in the results is referred to section III.

TABLE OF CONTENTS

PHOTOPRODUCTION OF ρ^o-MESONS IN A HYDROGEN BUBBLE CHAMBER AT PHOTON ENERGY LEVELS UP TO 5.8 GeV

I. INTRODUCTION

The photoproduction of ρ^o-mesons on hydrogen was first observed in 1961 on the Cornell Synchrotron [1]. The experiments of Crouch et al. [2] and Lanzerotti et al. [3] on the electron-accelerator in Cambridge showed that the ρ^o-photoproduction is a dominant process up to energies of 6 GeV. The cross-section as a function of energy and the behavior of the angular distribution for production and decay showed characteristics similar to diffraction scattering by Hadronen. This suggested the explanation of the ρ-production by a diffractive production mechanism.

However, further evaluation of the experiments indicated some difficulties:

1. The mean value of the ρ-mass appeared at 730-740 MeV and not at 760-770 MeV as in experiments using π-mesons as primary particles.

2. The results of the two groups [2] and [3] for the ρ-scattering on hydrogen differed by a factor of two.

3. Similar reactions such as the photoproduction of other vector-mesons ω and Φ were not at all observed or only with a small cross-section.

Therefore a photoproduction experiment with good statistics was started as soon as the 85-cm hydrogen bubble chamber at the German Electron Synchrotron in Hamburg was operational.

The bubble chamber is especially suitable to study the photoproduction of ρ^o-mesons. All particles of the production reaction $\gamma p \rightarrow p\pi^+\pi^-$ are visible in the bubble chamber. The reaction is kinetically threefold overdetermined. The dimensions of the 85-cm bubble chamber were selected such that the events can be measured with high accuracy up to the maximum available photon energies of approximately 6 GeV.

The experiment was started in the spring of 1965. The evaluation of the films was made by the bubble chamber groups

in Aachen, Berlin, Bonn, Hamburg, Heidelberg and Munich [4].

This work is based on approximately 8,400 events of the reaction $\gamma p \rightarrow p\pi^+\pi^-$. The statistics available for the final report will be doubled.

This report consists of two parts:

In the first part the experimental procedure is described in detail. The second part contains the cross-sections for multiple pion production (III 1) and for ρ^o-production (III 3). We compare the total cross-sections with the predictions on a combined vector-dominance quark model. The spin density matrix elements of the ρ^o-decay are discussed in (III 4).

The form of the ρ-mass distribution is examined in (III 2). The behavior and the location of the resonance curve can be explained by the interference of a resonant ρ-amplitude with a coherent background suggested by Söding [5].

The influences of the interference on the angular distribution for production and decay are demonstrated in (III 5) and they are compared to the predictions of the interference model by Krass [6]. The multidimensional fitting procedures to determine the resonance contributions and the density matrix elements are described in the Appendix.

II. DESCRIPTION OF THE EXPERIMENTAL PROCEDURE

1. Beam Setup

In order to examine the photoproduction with a bubble chamber one needs a parallel photon beam of sufficiently low, easily variable intensity. The beam profile must be such that the events are uniformly distributed across the width of the bubble chamber.

The Bremsstrahlung produced by an electron beam of the synchrotron in an internal target does not usually meet these specifications. The photon beam for the bubble chamber was therefore obtained as follows [7]:

Using a primary photon beam one produces an electron beam of different momentum and desired profile. The Bremsstrahlung produced by this electron beam in a thin target serves then as a

source for the bubble chamber.

Fig. 1 shows the beam setup. The electron beam which was accelerated to 6 GeV is incident on a metal target in the vacuum chamber of the synchrotron. The Bremsstrahlung emanating tangentially produces high-energy electrons in target T1 (3-6 mm Cu) by pair production. The electrons are focussed by means of the quadrupoledoublet QB1-QB2 and the bending magnet MB1. They are momentum-analyzed by the collimator K2 (full aperture opening ~1.5 cm). A momentum resolution of $(\Delta p)/p \simeq \pm 1\%$ is achieved.

The desired beam shape is achieved by an additional doublet of quadrupole magnets QD1-QD2. The following bending magnet MB2 deflects the beam in the direction of the bubble chamber. After passing through the beam-hardener (60 and 80 cm respectively of crystalline LiH, with 10-cm Ø) and the horizontal collimator K3 (full aperture opening 3 cm) the bremsstrahlung produced a. Target T2 (1-1.5 mm Cu) reaches the bubble chamber. The residual electron beam is deflected by the magnet MB3.

The beam is cleaned of secondary particles by two bending magnets MA1 and MB4 which contain the beam-hardener and the collimator K3 respectively.

The aperture opening of the collimator K1 and the thickness of the targets T1 and T2 can be remotely adjusted. A quick variation of the intensity is possible in this manner. The photon flux is limited by the number of electron-positron pairs and by the Compton electrons which can be tolerated for a reliable evaluation of the photoproduction results in the bubble chamber. A beam intensity of 70 equivalent quantas* ($E_\gamma > 0.1$ GeV) per picture at a maximum energy of 5.8 GeV appeared to be favorable. This corresponds to approximately 11 pairs (with energies > 0.1 GeV) in a chamber region of 47 cm length.

---

*Number of equivalent quantas =

$$\frac{\text{Total energy transported by the } \gamma\text{-beam}}{\text{maximum beam energy}}$$

On the average one finds one photoproduction event with three or more resulting tracks for each 30 pictures.

The energy of the electron beam could be adjusted to an accuracy of approximately 0.8%. Momentum measurements on electrons of nominal energy which were directly deflected into the chamber were used to verify the adjusted energy values.

The accurate positioning and the field values of the magnets were tabulated with the analog computer at DESY. Fig. 2 shows the particle trajectory envelopes in the horizontal and vertical plane. In the horizontal plane the beam is focussed at the location of the bubble chamber, whereas it is kept broad in the vertical plane which is parallel to the picture plane of the camera. The latter is done to achieve a uniform distribution of tracks over the picture width. Based on calculations, and taking into consideration multiple scattering in Target T2, one expects a photon beam in the chamber with the diameters (foot-breadth) $Dy = 17$ cm

$Dz = 3.6$ cm

and divergences $y' = \pm 2.5$ mrad

$z' = \pm 1.2$ mrad

(see Fig. 3a for definition of the reference frame).

The given values depend on the emittance of the electron beam in the synchrotron at the machine target. The properties of the photon beam can be determined experimentally by measuring the tracks produced in the bubble chamber.

Figs. 4 and 5 show the spatial distribution of the origins of production and the directions λ and Φ of electron pairs in the chamber. In this case λ and Φ are essentially the projected angles in the xz- and xy plane respectively.

The widths of the given distributions of λ and Φ

$$\sigma_\lambda = \pm 3.2 \text{ mrad}$$

$$\sigma_\Phi = \pm 2.1 \text{ mrad}$$

are mainly determined by the measuring errors. The distributions are compatible with the beam transport calculations and its assumed initial conditions.

The energy spectrum of the photon beam was calculated from

the energy distribution of the measured electron pairs. Fig. 6 shows two photon spectra with maximum energies of 5.45 GeV and 5.8 GeV respectively. Deviations from the theoretical radiation spectrum (full line) are apparent.* The location of the upper radiation edge is flattened at high energies by the finite measuring accuracy $((\Delta E_\gamma)/E_\gamma = \pm 6\%$ at 5.5 GeV). At low energies the spectrum is exaggerated. The measured spectrum can be reproduced above 3 GeV (dotted line) if one folds the energy resolution into the theoretical radiation spectrum.

Furthermore, deviations show up at low energies as a result of multiple processes (cascades) in the beam-hardener.

Beam-hardeners are used in photoproduction experiments with bubble chambers in order to reduce the contents of low-energy γ-quanta ($E_\gamma < 10$ MeV).

Low-energy quanta suffer especially high scattering losses in the beam-hardener due to the highly energy-dependent Compton process.

Crouch et al. [2d] obtained a spectrum of similar distribution in a bubble-chamber experiment at the electron accelerator in Cambridge, Massachusetts. They used a beam-hardener consisting of 1.8 radiation length beryllium which were distributed in a 72-in-long magnetic field in the form of 1-in-thick plates. Based on the data given in [2d] one expects that a LiH beam-hardener of 0.3-0.5 radiation lengths thickness, placed the form of plates in a magnetic field, will result in an even-more-favorable spectrum distribution than the arrangements used so far.

The experiments were carried out in four parts from February 1965 to June 1966. A total of 1,730,000 pictures

---

*The finite thickness of the second conversion-target T2 and the collimation of the photon beam were taken into consideration in the calculation of the theoretical photon spectrum [8]. The finite target thickness (0.065 and 0.1 radiation lengths respectively) had a relatively small influence on the spectrum distribution above 5 GeV.

were taken. Table I shows a summary of the operating conditions during the different stages.

Table I: Summary of the Four Experimental Parts

Part	Date	No. of pictures		Beam Energy GeV		Beam Direction [rad]	
		taken	evaluated	nominal	measured	λ	Φ
I	Feb.-March 1965	58,000	33,200	5.5		0.0025 $\pm$0.003	3.1428 $\pm$0.002
II	May 1965	396,000	278,700	5.45	5.44 $\pm$0.10	-0.0015 $\pm$0.003	3.1428 $\pm$0.002
III	Nov.-Dec. 1965	580,000	1) 331,670	5.8	5.83 $\pm$0.08	-0.002 $\pm$0.0035 -0.002 $\pm$0.0035	3.1413 $\pm$0.0021 3.1435 $\pm$0.0021
IV	June 1966	696,000	1)	5.8	5.80 $\pm$0.12	-0.00296 $\pm$0.0032	3.1416 $\pm$0.0021
	Sum	1730,000	643,570				

cont'd next page

1) Evaluation not yet completed
2) Given values are average values in the chamber center

Average thickness of the second conversion target:
Part I and II 1 mm Cu
Part III and IV 1.5 mm Cu

Continued on page 8.

Table I (continued)

Part	Beam Hardener	Bubble Chamber		Average length of scanning vol. [cm]	No. of tracks in scanned events	Average no. of tracks in scanning vol.
		Magnetic field [kG] 2)	Exposure rate [sec^{-1}]			
I	80 cm LiH B=0	21.3	1	47	≥ 1	13.3
II	60 cm LiH B=8.6kG	20.9	1	47	≥ 1 ≥ 3	8.4
III	60 cm LiH B=8.6kG	22.6	1 1.43	47 43	≥ 3	1) 11.3
IV	60 cm LiH B=8.6kG	20.9	1 1.43 1.67	43	≥ 3	1)

2. Bubble Chamber

The experiments were carried out with the 85-cm bubble chamber at DESY. The bubble chamber was built during 1961 to 1964 closely following the design of the 81-cm bubble chamber of the Ecole Polytechnique in Saclay [9]. The chamber depth was enlarged and the optical system [10] including the cameras was completely redesigned. The hydrogen supply was changed from a dewar operation to a liquifier.

Figs. 3a and 3b show a schematic layout of the elements of the chamber.* The maximum useful inside extension of the chamber body is 85 cm by 40 cm by 40 cm.** The limiting planes at the two narrow sides are rounded off in semicircular fashion. The useful volume is 110 liters hydrogen.

Two 7.5-cm-thick glass windows located on the broad sides allow illumination of the chamber from the flash side and also observation of the tracks through the cameras.

The chamber is operated at approximately $26^{\circ}K$. A chamber mantle, scavenged by liquid hydrogen, is used to regulate the temperature. Heat losses by radiation are minimized by two heat shields around the chamber body. The temperatures of these heat shields are approximately $27^{\circ}K$ and $77^{\circ}K$ respectively. The chamber body with the heat shields is supported in a safety tank. Heat transfer by conduction and convection is mostly prevented by the vacuum of 10^{-6} torr which exists in this tank.

The expansion system is located above the chamber. The liquid hydrogen is brought into a supercritical condition by an almost adiabatic expansion from a rest pressure $p_o = 5.5$ kg/cm^2 to approximately 3.5 kg/cm^2. This supercritical state allows formation of bubbles along the tracks of ionizing particles.

---

*Technical details are found in DESY Report 67/14 (1967) by G. Harigel, G. Horlitz, S. Wolff.

**The width between the inner walls of the two small sides (beam entrance and beam exit) is 85 cm. The window gaskets limit the free length to 81 cm).

The coils of the electromagnet are located on either side of the chamber around the second heat shield. The magnet produces a magnetic field in the chamber of approximately 22 kG.

The safety tank and the chamber body contain at the beam-entrance location two thin metal windows (10-cm wide, 20-cm high, material: on the safety tank 0.5 mm steel, on the chamber body 3 mm aluminum). The particles produced in reactions in the outer beam-entrance window are deflected by a premagnet with a field of 11 kG. Particles with momentum $\leq$ 2 GeV/c do not reach the chamber.

The lighting of the bubble chamber is according to the principle of dark-field illumination (see Fig. 7). The light of four high-performance xenon flashbulbs is imaged by two banks of condensors at a location outside the camera opening. Only the light scattered under small angles from the vapor bubbles reaches the diaphragms of the cameras. An optimum illumination of the chamber is achieved with this arrangement.

The extension of the visible volume depends on the location of the cameras and the flashbulbs (see Table II). A visible region of approximately 77 cm length is covered by a combination of three cameras. The region covered by all three cameras simultaneously is 62 cm long.

Table II: Maximum Extension of the Visible Region in the Bubble Chamber at Normal Positioning of the Flashbulbs. (For definition of the coordinate systems see Fig. 3a.)

Camera 1	-39 cm $\leq$ x $\leq$ 31 cm	-16 cm $\leq$ y $\leq$ 18 cm	-40 cm $\leq$ z $\leq$ 0 cm
2	-31 cm $\leq$ x $\leq$ 38.5 cm	-17 cm $\leq$ y $\leq$ 17 cm	
3	-39 cm $\leq$ x $\leq$ 31 cm	-18 cm $\leq$ y $\leq$ 16 cm	

The cameras are built for an exposure frequency of 5 pictures/sec. At this velocity one cannot reliably fix the film with a suction mechanism. The film is instead pressed against a 1.7-cm-thick glass plate by an upholstered metal plate.

The cameras work with a reduction of 1:15 in the midplane

of the chamber. Two 5.7-cm-thick glass plates are located between the cameras and the chamber body. They serve as windows between the safety tank and the outside heat shield.

A number of 3-cm-high cross-marks are etched into the glass on the two inside surfaces and on the flash-oriented outer surface of the camera window. They are photographed together with the tracks and serve as reference points for coordinate measurements on the film.

The values of the camera coordinates, the chamber depth and the distance between the front mainpoint and the front glass of the chamber can be determined to 0.1-0.3 mm accuracy using a procedure given by G. Wolf [11] which requires the measurement of the reference marks on the film. In addition to the coordinates of the reference marks measured on the film one also uses the special coordinates of the reference marks on the glass plates which were determined at room temperature. One obtains thus the desired parameters with an optimizing procedure. The contraction of the glass plates during cooling from room temperature to 31°K was fixed at $\frac{\Delta l}{l} = 10^{-3}$.

The hydrogen requirement for the filling of the chamber and for cooling purposes is fulfilled by a liquifier which is directly connected to the chamber. One uses parahydrogen to fill the chamber itself. The density of hydrogen was determined for the first section by measuring μ-meson tracks resulting from π^+-decays at rest. It is $\rho = 0.06204 \pm 0.00099$ g/cm^3. The magnetic field in the bubble chamber is homogeneous to good approximation. The vector $\vec{B}$ points in the z-direction. The absolute value of B depends on the location in the chamber to within $\pm 6\%$. The special distribution of the z-component of the field is taken into consideration in the evaluation procedures. The magnets could not be regulated for technical reasons, but had to be operated by direct control. Long-term fluctuations of the magnet current of approximately $\pm 2.5\%$ appeared during individual sections of the experiment. The magnetic field values were therefore read in regular intervals and averaged over each film (~ 3000 pictures). The fluctuations within one

film were less than $\pm 0.5\%$.

3. Scanning of the Films

The evaluation procedure of the Hamburg group is described in the following sections 3-6. The procedures of the other groups are similar.

Just as in bubble-chamber experiments with charged particles, the scanning procedure serves a double purpose, namely to find the expected interactions on the films and to determine the beam-particle flux at the same time.

The goal was to find all events which led to the production of strongly-interacting particles. Events appear with either 1,3,5,7.. charged tracks since the initial condition (γ + p) is positive and singly charged. Strange particles can be recognized due to their characteristic decay. The high electromagnetic background can be separated because of the requirement of a positive total charge. The background is made up of Compton electrons (appearing as single negative tracks), of electron-positron pairs with a total charge of -1 which are produced in an interaction with the electron, and of pairs produced in interactions with the nucleus (visible total charge 0).

Furthermore, the strongly-interacting particles are most often emitted at larger angles to the beam direction than the electrons and positrons which are close to the forward direction.

The films from two cameras are projected on projection tables with a magnification of 1.31 and 1.5 respectively (compared to the experimental setup). They are also scanned by a scanner.

The photoproduction events which are observed in a defined region of camera 2, i.e. the scanning volume, are noted in tables. Contact prints are made simultaneously using a scale of 1:1. The tracks and origins are labelled to allow identification during measuring and evaluation programs. The scanning volume is limited so as to allow measurements of the tracks of all events to a sufficient length (minimum length of 13 cm for

forward tracks and 10 cm for backward tracks). The extension of the scanning volume was selected differently by the various groups. It measured on the average 47 cm (-29 cm $\leq x \leq +18$ cm) for the films used in this work. The length of the scanning volume was reduced to 43 cm (-29 cm $\leq x \leq +14$ cm) in the second part of the evaluation. For a definition of the coordinate systems see Fig. 3a. In each case the scanner examines whether the end points of strongly-ionizing positive tracks are located in the chamber. If a positive particle comes to rest within the chamber without decay or annihilation it has to be a proton in this experiment. The end-points are specially labelled. In addition to measuring the momentum one measures also very accurately the range at the scanning tables. Secondary interactions of particles produced in the event are labelled and measured only if the momentum of the connecting track cannot be determined to better than 6% accuracy.

One uses the electromagnetic background of electron-positron pairs in order to count the beam flux in photoproduction experiments with bubble chambers. One can compute the number and energy distribution of the pairs, the photon spectrum and its intensity since the cross section for pair production is sufficiently well known.

Once every 100 frames one counts all the electron pairs including the pairs produced on the orbital electron which have a total energy larger than 50 MeV. They are also labelled on contact prints. The length of the scanning volume for pairs and events is already exactly the same and therefore does not enter into the calculation of the cross sections. If an unusable picture appears in between two pair counts, it is omitted. The following pair count is then shifted by one frame.

The following are termed unusable:

1. Pictures where either the camera or the flash did not work (even if only one camera missed).

2. Empty frames.

3. Pictures with a high pair density where a reliable pair count is not possible.

The results of unusable pictures are not noted.

The number of unusable pictures on the evaluated films is generally between 1 and 5%.

All films are scanned twice by independent observers. Contact prints of pictures with pair counts are made also in the second scanning procedure.

The tables of both scanning procedures are then fixed on keypunch cards. The results are then examined by a computer program [12] for agreement and a list of deviations is printed out.

Next, a careful scanning procedure examines and compares the deviations and a decision is made. The result is fixed on an additional scanning keypunch card. The combined scan quality α for both scanning procedures can be computed by:

$$\alpha = \frac{V(n_1 + n_2 - V)}{n_1 \cdot n_2}$$

where n_1 = number of events found in the first scanning procedure

n_2 = number of events found in the second scanning procedure

V = combined total = number of events found in the first and/or second scanning procedure

The scanning quality depends on the number of tracks and the presence of strongly-ionizing particles (protons).

It is for 1-track events with a proton	99.3%
1-track events without proton	97.1%
3-track events with a proton	99.8%
3-track events without proton	99.2%
$\geq$ 5-track events	~100 %

The scanning quality for pair production was approximately 99.6%. All cross sections are corrected for unobserved events and pairs.

4. Measurements

The measurements were carried out at Hamburg using two digital-measurement projectors of the Coknitron [13] and Messwolff [14] type.

Approximately 10 points are measured around each track. Furthermore, 4-5 reference marks are measured in each camera. They serve as reference points for the spatial reconstruction. The smallest measuring unit corresponds to approximately 70 μ in the chamber.

The measuring accuracy is limited by:

1. adjustment accuracy at the measuring table,
2. Coulomb scattering of the tracks,
3. projection errors at the measuring table,
4. projection errors and distortions in the bubble chamber.

In order to examine the two latter sources of errors, electron tracks at 5.8 GeV were measured. These tracks were measured while the magnetic field was B = 0 ("straight tracks"). The distortions in the optical system of the measuring table can be mostly eliminated by two sets of measures. First, the film is inserted in beam direction and then in the opposite direction. Table IIIa shows the results.

Table III: Measurement and Projection Errors

Location of the film during measurement	$\bar{\frac{1}{r}}$ ($10^{-5}cm^{-1}$)	$\sigma(\frac{1}{r})$ ($10^{-5}cm^{-1}$)	$\bar{\frac{1}{r}}$ chamber ($10^{-5}cm^{-1}$)	correction for distortion of measuring table optics
a) in beam direction	-1.2 $\pm$0.45	1.9	-0.37 $\pm$0.7	no
a) opposite direction	+0.83 $\pm$0.39	1.7		
b) in beam direction	-0.79 $\pm$0.39	1.8	-0.66 $\pm$0.7	yes
b) opp. direction	+0.13 $\pm$0.42	1.7		

The measured mean curvature $\bar{\frac{1}{r}}$ of the tracks is not zero ($\bar{\frac{1}{r}} \sim 10^{-5}cm^{-1}$) and the sign is opposite for the two measuring series. It is thus mainly due to distortions at the measuring

table. The difference between the two values $\overline{\frac{1}{r}}_{\text{chamber}}$, which is due to distortions in the bubble chamber and in the bubble-chamber optics is smaller and negligible. The scatter $\sigma(\frac{1}{r})$ of the distribution of $\frac{1}{r}$ is a measure of the adjustment accuracy. The latter is expressed by the maximum detectable momentum P_{MDM}. The error in the momentum due to adjustment accuracy is equal to p, for $p = p_{MDM}$ if the track is measured over the full length of the chamber (~60 cm per camera). The value of p_{MDM} is approximately 350 GeV/c for the measuring projectors.

The influence of the projection errors at the measuring tables can be reduced by a correction procedure. One uses approximately 100 grid-points of a quadratic grid which is used instead of a film. The grid-points are measured in each camera projection. A third-order correction polynomial is determined for both counting directions from the deviations of the measuring points from the exact grid. The measuring points of all track measurements in the geometry program can be corrected with the help of this correction polynomial. Table IIIb shows the corrected results of measurements for straight tracks.

The mean detectable curvatures are reduced to approximately one half ($\sim 0.5 \cdot 10^{-5} cm^{-1}$) and they do not contribute significantly to the measuring accuracy.* Thus the inaccuracies in the measurements are mainly due to adjustment errors and Coulomb-scattering errors.

5. Spatial and Kinematic Reconstruction of the Events

A series of computer programs evaluates the experimental data. First the behavior and the location of the measured tracks and points are reconstructed in space by means of a geometry program. Then a kinematic program assigns particle

---

*The correction procedure was used since early 1966 for the events measured at Hamburg. Only 1700 events with three or more tracks and all 1-track events measured in 1965 are not distortion corrected.

masses to the tracks and evaluates the kinematically-possible particle combinations for each event.

5.1. Spatial Reconstruction. The WELAGA program [15, 16] which was written by G. Wolf is used as geometry program. The geometrical ratios of the bubble chamber at DESY are taken into consideration.*

The geometry program provides for each track the spatial coordinates of the origin and end-points of the track, the curvature $\frac{1}{r}$ in the middle of the track, the angle of inclination λ and the projected angle Φ, and furthermore the errors $\Delta(\frac{1}{r})$, $\Delta\lambda$ and $\Delta\phi$.

We use the following definitions:

r = radius of the projection of the track into the xy-plane

λ = angle of inclination between the track and the xy-plane

Φ = angle between the x-direction and the projection of the track into the xy-plane

For definitions of the coordinate section see Fig. 3a.

The exact locations of the cameras, the bubble-chamber windows and the reference marks are determined for each section of the experiment according to a procedure described in [11]. They are then introduced into the geometry program.

A new section of the experiment begins after each warmup of the bubble chamber to the boiling point of nitrogen.

If there are several measurements for one event the HERAK program begins after completion of the WELAGA. The HERAK program searches the different measurements of each event for the points having the smaller errors in location (minimum Δz) and the tracks with the smallest errors in radius of curvature. It produces a "new" event from these data. Since only individual

---

* The influence of the glass plates in front of the film plane must be equalized [17].

tracks have to be remeasured in general, the HERAK program reduces the effort for remeasurements.

5.2. Kinematic Reconstruction. The GRIND program [18] written at CERN is used for the kinematic matching.

In addition to the results of the geometrical computation the following experimental data are reduced in GRIND program:

1. energy-range table in hydrogen,
2. magnetic field table,
   a. spatial distribution of the magnetic field,
   b. average values of the field in the evaluated films,
3. direction of the γ-beam for the various sections of the experiment.

The beam direction is determined from the direction of electron pairs having energies larger than 500 MeV. The values are listed in Table I.

Using the magnetic field table the GRIND program calculates first the momentum for each track in the middle of the track. Then particle masses are assigned and the momenta at the track origin are calculated. The contribution of the Coulomb scattering to the errors is introduced.

The particle combinations shown in Table IV are calculated for the assignment of the mass. The individual particle combinations are called hypotheses.

Table IV: List of Hypotheses Calculated with GRIND

1-track events	$\gamma p \rightarrow p\pi^o$	OF
	$n\pi^+$	OF
3-track events	$\gamma p \rightarrow p\pi^+\pi^-$	3F
	$p\pi^+\pi^-\pi^o$	OF
	$n\pi^+\pi^+\pi^-$	OF
	pK^+K^-	3F
	$pK^+K^-\pi^o$	OF
5-track events	$\gamma p \rightarrow p\pi^+\pi^+\pi^-\pi^-$	3F
	$p\pi^+\pi^+\pi^-\pi^-\pi^o$	OF

	$n\pi^+\pi^+\pi^+\pi^-\pi^-$	OF
	$pK^+K^-\pi^+\pi^-$	3F
	$pK^+K^-\pi^+\pi^-\pi^o$	OF
7-track events	$p\ 3\pi^+3\pi^-$	3F
	$p\ 3\pi^+3\pi^-\pi^o$	OF
	$n\ 4\pi^+3\pi^-$	OF

3F hypotheses with 3 degrees of freedom

OF hypotheses with 0 degrees of freedom

Furthermore there are numerous hypotheses for events of visibly decaying strange particles.

The following is known for computation:

The momenta and angles of the resulting charged particles, the angles of the incoming photons and the masses of the incoming and resulting particles. Four conservation theorems must fulfilled as secondary conditions. For the case of hypotheses without neutral particles in the final condition one computes first the only unknown, namely the momentum of the incoming photon, by means of the secondary conditions. The event is then still threefold overdetermined (χ^2-distribution with three degree of freedom). The track data p, λ and Φ are improved by means of an optimization procedure and the quality of the fitting is examined. The following expression is minimized:

$$M(x_1^{Fit}, \ldots, x_{3n}^{Fit}, a_1, a_2, a_3) =$$

$$\sum_{k,j=1}^{3n} \left(x_j^G - x_j^{Fit}\right) G_{jk} \left(x_k^G - x_k^{Fit}\right) + \sum_{m=1}^{3} a_m F_m \left(x_1^{Fit} \ldots x_{3n}^{Fit}\right) \qquad (1)$$

where n = the number of incoming and outgoing particles

x_{3i-2}, x_{3i-1}, x_{3i} = values of $\frac{1}{p}$, λ, Φ of the i-th particle

x_i^G = measured values

x_i^{Fit} = fitted and improved values

G_{jk} = inverse matrix of the errox matrix G_{jk}^{-1}

The sum $\Sigma a_m F_m$ serves that the quantities x_i^{Fit} fulfill the energy and momentum equations. Only hypotheses whose momenta

and energies are within the physical region are accepted. M has a χ^2-distribution with three degrees of freedom if the experimental data have a Gaussian distribution. Thus M is also denoted as χ^2.

For the case of hypotheses with one resulting neutral particle one can compute the momentum of the photon and the three momentum components of the neutral particle by means of the four secondary conditions. No other secondary conditions are available to kinematically rule out the possible participation of two and more neutral particles (0 degrees of freedom).

In this experiment events with two or more resulting neutral particles are treated as if they contained only one neutral particle. They represent a mixing amongst the true events with one neutral particle.

5.3. Error Treatment in the GRIND Program. The treatment of errors in the GRIND program was completely revamped by G. Wolf. Whereas in the original version of GRIND the errors are determined only by the track length and the angle of inclination and independently of the quality of the single measurement, one takes in the Hamburg version of GRIND the experimental errors for each single track from the geometry program. The treatment of errors was described in detail by G. Wolf in [16].*

The χ^2-distribution serves as test for the error treatment.

The χ^2-distribution of the events with three degrees of freedom should follow the theoretical χ^2-distribution if the error treatment is correct and the experimental data have a Gaussian distribution.

---

*Only the error due to Coulomb scattering was not treated as given in [16], p. 27, but according to Eq. (4) of this report.

The histogram in Fig. 8 shows the experimental χ^2-distribution for 8373 events of the type $\gamma p \rightarrow p\pi^+\pi^-$. Agreement with the theoretical curve is satisfactory.

The TASTE program gives a clear print-out of the results of GRIND.

The GRIND program examines the measuring quality in order to simplify selection of the hypotheses.

The requirement for each point of an event having measuring errors Δx, Δy, Δz is that the sum of the errors squared is $\Delta x^2 + \Delta y^2 + \Delta z^2 \leq 1\ cm^2$.

The requirement for the momentum error of each track is:

$$\left(\frac{\Delta p}{p}\right)_{Geom} \leq \left[f_M \left(\frac{\Delta p}{p}\right)^2_M + f_c \left(\frac{\Delta p}{p}\right)^2_c\right]^{1/2} \qquad (2)$$

where

$$\left(\frac{\Delta p}{p}\right)_M = \frac{p}{P_{MDM}} \left(\frac{60\ cm}{L \cos \lambda}\right)^2 . \qquad (3)$$

$(\frac{\Delta p}{p})_{geom}$ = relative momentum error in the middle of the track before the kinematic fitting

$(\frac{\Delta p}{p})_M$ = contribution of the adjustment errors to the momentum error

P_{MDM} = 300 GeV/c

L = track length in cm

$f_c(\frac{\Delta p}{p})^2_c$ = contribution of the Coulomb scattering to the measuring error

$$\left(\frac{\Delta p}{p}\right)^2_c = \left(\frac{k}{\beta}\right)^2 \left[\frac{2}{3}\left(\frac{r}{p}\right)^2 \frac{1}{L \cos^4 \lambda} + \frac{1}{6} \frac{L \sin^2 \lambda}{p^2}\right] \qquad (4)$$

$\beta = \frac{v}{c}$

r = track radius in cm

$k = 0.675\ GeV/c \cdot cm^{-\frac{1}{2}}$

λ = angle of inclination

The values for f_M and f_c were selected as $f_M = 4$ and $f_c = 0.25$.

Table 5 shows the error limits for tracks having $\cos \lambda = 1$ and a length of 30 cm.

Table 5: Error Limits for Tracks with $\cos \lambda = 1$ and L = 30 cm

P [GeV/c]	$\left(\frac{\Delta p}{p}\right)_M$	$\left(\frac{\Delta p}{p}\right)_c$	Limit for $\left(\frac{\Delta p}{p}\right)_{geom}$
0.1	0.0013	0.0252	0.013
0.2	0.0027	0.0180	0.010
0.5	0.0067	0.0154	0.015
1.0	0.0133	0.0151	0.028
2.0	0.0266	0.0149	0.054
5.0	0.0666	0.0148	0.133

The error limits given by Eq. (4) can be reduced for almost all events by taking one or several measurements.

6. Selection of Hypotheses and Test of the Decision Criteria with the FAKE Program

Before going on with the contents of this section the reader is once more referred to the list of hypotheses computed by the GRIND program (Table 4).

The kinematic program can assign several hypotheses to each event due to the finite measuring accuracy. One must therefore find the most likely amongst the various hypotheses. The decisions are made by physicists to whom contact prints of the events are available in addition to the print-outs of the GRIND program. First, the measuring quality is examined individually for each track. The following decision criteria are applied in sequence to well-measured tracks:

1. Hypotheses with three degrees of freedom are printed out by the GRIND program only if the value of $\chi^2 \leq 16$. The limitation of $\chi^2 \leq 16$ in case that the experimental and the theoretical χ^2-distributions are in agreement means that less than 0.1% of the true events with three degrees of freedom

are thrown out.

However, the experimental χ^2-distribution is above the theoretical distribution for $\chi^2 \geq 10$ as shown in Fig. 8. Due to this behavior we estimate that the possible loss of true events with three degrees of freedom due to the limitation on χ^2 is less than 1%.

2. Only hypotheses are accepted for which the calculated and the observed ionization of the tracks is compatible. The ionization of the tracks is estimated on contact prints and in difficult cases at the scanning table. Based on the varying bubble density one can usually distinguish π-mesons from protons for momenta up to $p \leq 1.4$ GeV/c and K-mesons from protons for momenta $0.4 \leq p \leq 1.1$ GeV/c.

3. Hypotheses with a photon energy $E_\gamma > E_{max} + 3\,\Delta E_\gamma$ are thrown out (E_{max} is the maximum energy of the photon beam and ΔE_γ is the error of E_γ). Thus the hypotheses whose photon energies have a 99.7% probability of not being included in the maximum possible energy are neglected.

4. If one of the remaining hypotheses has three degrees of freedom it is accepted as the only hypothesis of the event. Monte Carlo calculations have shown that this procedure introduces an error of less than 1%. The calculations will be described below. If two hypotheses with three degrees of freedom are possible they are treated as being equal. We thus prevent the loss of the rare reactions $\gamma p \rightarrow pK^+K^-$ in which the Φ-meson can be produced.

5. Only events with 0 degrees of freedom remain at this point. If after application of the criteria (1) through (4) exactly one hypothesis is possible it will be accepted. If several hypotheses are possible they are treated as being equal. The event is then considered ambiguous. Ambiguity usually occurs only above photon energies of 2.5 GeV where in some kinematic regions a separation of the hypotheses based on the ionization is not possible. However, if one of the possible hypotheses is of the type $pK^+K^-\pi^o$, $pK^+K^-\pi^+\pi^-\pi^o$, it is neglected. The rate of production of charged K-mesons is very small

compared to the rate for π-mesons. The procedure thus introduces a small addition of $\leq$ 1% to the group OF hypotheses which has π-production.

6. A small group of events (1.5%) yields neither a hypothesis with three nor a hypothesis with 0 degrees of freedom. They are classified as no-fit events.

7. The number of events which are not measurable due to technical or geometrical reasons is 1.8% for 3-track events and approximately 5% for events with 5 tracks. Events which show decaying strange particles are computed and decided in a special procedure. This procedure is described in [4h] and [19].

The criteria (1) to (3) and (5) have already been explained above. The criterion (4) was obtained based on calculations with the FAKE program.

We utilized a version of the FAKE program [20] which was worked out by E. Raubold.

Using Monte Carlo procedures the FAKE program generates events with up to six resulting tracks. A characteristic angular distribution can be assigned to one of the particles. The track parameters $(\frac{1}{r}, \lambda, \Phi)$ are played within the measuring accuracy and realistic errors are attached. Thereafter the events are treated as normal events by the GRIND program.

The FAKE program thus simulates the results of the geometry program and enables it to test the quality of the fit in the kinematic program.

Various parameters of the FAKE program were first assimilated to the experimental conditions (expansion of the bubble chamber, measuring accuracy, etc.). We examined the accuracy of this assimilation by means of two test quantities. Fig. 8 shows the χ^2-distribution for both measured and FAKE-produced events of the type $\gamma p \rightarrow p\pi^+\pi^-$. The distributions agree satisfactorily. This means that the FAKE program simulates the scattering of the track parameters of the actually-measured events.

The second test quantity is M_γ^2. One computes M_γ^2 from:

5-Track Events

$$M_\gamma^2 = \left[\sum_{i=1}^{n} p_i - p_o \right]^2$$

where p_i = four-momentum of the n resulting charged particle (before the fitting in GRIND)

p_o = four-momentum of the target proton

M_γ^2 corresponds to the square of the photon mass for events with three degrees of freedom. M_γ^2 is distributed about 0 due to the finite measuring accuracy. The width of the distribution is a measure for the measuring accuracy.

Fig. 9 shows two distributions of M_γ^2 for both measured and FAKE-produced events of the type $\gamma p \rightarrow p\pi^+\pi^-$. The widths of the distributions agree well.

As a result of this agreement 3- and 5-track events were produced with the FAKE program. These events are first analyzed with the GRIND program. The selection of the hypotheses is according to criteria (1) through (6).

The results are summarized in Table 6. The left-hand side of the table shows the number of events produced, the angular distribution of the out-coming nucleon in the center-of-mass system, the photon energy and the type of event. The right-hand side presents the hypotheses accepted for reasons of criteria (1)-(6).

The results can be briefly summarized as follows:

1. Events with three degrees of freedom simulate in less than 1% of the cases a hypothesis with 0 degrees of freedom.

2. Events with 0 degrees of freedom of the type $p\pi^+\pi^-\pi^o$ simulate in approximately 1% of the cases a hypothesis with three degrees of freedom.

3. Events of the type $n\pi^+\pi^+\pi^-$ do not simulate hypotheses with three degrees of freedom within the available statistics.

W. Tejessy obtained similar results in Bonn [22]. He used the original version of the FAKE program from Berkeley [20].

Table 6: Branching Ratios of the Events Produced by the FAKE Program

N produced	Angular distribution of nucleons	E_γ [GeV]	Final State Produced	Assumed Hypotheses (%)								
				$p\pi^+\pi^-$	$p\pi^+\pi^-$ / $\pi^+p\pi^-$	$p\pi^+\pi^-\pi^o$	$n\pi^+\pi^+\pi^-$	$p\pi^+\pi^-\pi^o$ / $n\pi^+\pi^+\pi^-$	Nofit p	pK^+K^-	pK^+K^- / K^+pK^-	$p\pi^+\pi^-$ / pK^+K^-
3-Track Events												
100	isotrop	0,75	$p\pi^+\pi^-$	100								
200	isotrop	0,75		99		0,5			0,5			
100	~f(cosθcm)+)	1,6		100								
100	isotrop	2,0		100								
100	~f(cosθcm)	3,0		97	2				1			
100	~f(cosθcm)	4,0		92	8							
100	e^{+10t} ++)	2,0	$p\pi^+\pi^-\pi^o$			100						
90	~f(cosθcm)	4,0		2,2		70		27,8				
100	isotrop	2,0	$n\pi^+\pi^+\pi^-$				100					
100	isotrop	3,0	pK^+K^-							98	2	
100	e^{+10t}	3,0								100		
100	e^{+10t}	1,6	pe^+e^-	16					84			
100	e^{+3t}	0,75	$pe^+e^-\gamma$	1		35			64			

5-Spur-Ereigniss				$p\pi^+\pi^-\pi^-\pi^+$	$p\pi^+\pi^+\pi^-\pi^-$ / $\pi^+p\pi^+\pi^-\pi^-$	$p2\pi^+2\pi^-\pi^o$	$n3\pi^+2\pi^-$	$p2\pi^+2\pi^-\pi^o$ / $n3\pi^+2\pi^-$	$pK^+K^-\pi^+\pi^-$
100	isotrop	4,0	$p\pi^+\pi^+\pi^-\pi^-$	92	8				
100	isotrop	4,0	$p\pi^+\pi^+\pi^-\pi^-\pi^o$	1		35	3	61	
50	~f(cosθcm)	4,5				62		38	
50	isotrop	4,0	$n\pi^+\pi^+\pi^+\pi^-\pi^-$				86	14	
50	~f(cosθcm)	4,5					69	31	

++) The angular distribution of the nucleon is determined by e^{+10t}. $|t|$ = (momentum transfer (proton/proton))^2

+) An experimentally-determined angular distribution was imprinted on the nucleon.

*Tr. Note: Commas in numerical material indicate decimal points.

If we transpose the results of the FAKE program to the measured events the following results:

1. The probability that an event with three degrees of freedom is lost or simulated is less than 1% based on the true number of events with three degrees of freedom, if the 4th criterion is applied.

The reaction $\gamma p \rightarrow pe^+e^-$ with a visible proton is an exception.

The events pe^+e^- simulate in approximately 15% of the cases a hypothesis of the type $p\pi^+\pi^-$. Part of the events pe^+e^- can be separated out due to ionization. The remaining events supply a negligible contribution to the group $p\pi^+\pi^-$ due to the small cross section ($\sigma^{pair}(p_p > 100$ MeV/c) ≤ 0.1 μb).

The results of the FAKE program can only conditionally explain the distribution of the ambiguous events.

Ambiguity appears if two hypotheses cannot be separated based on the ionization. It is not possible to exactly simulate the experimental momentum distributions of all resulting particles with the existing version of the FAKE program. The distributions of the ionization values of produced and true events therefore show differences.

The true ratios can be approximated if one imprints an experimentally-determined angular distribution onto the resulting nucleons.

7. Organization of Data for the Physical Analysis

After selection of the hypothesis one puts the most important kinematic quantities of all events onto magnetic tape. They are thus available to compute the distributions of the interesting quantities.

The CUT 1 program [23] sorts the results of the GRIND program for the assumed hypotheses. The CUT 2 program produces a data tape which serves as input for the plotting program HYBRID-ULTRAN [24]. The CUT 3 program combines the hypotheses of the individual events with the scanning information which is also stored on tape. By comparing scanning information and

assumed hypotheses one can easily find misinterpretations which occur in the scanning procedure. In addition one obtains from this comparison a convenient and reliable survey of how many of the events found in the scanning procedure have gone through the chain of analysis from the measurement to the production of the data tape for the plotting program. Repeated application of this comparison rules out the possibility that events "get lost" during evaluation.

The HYBRID-ULTRAN plotting program [24] produces distributions of the kinematic and geometric quantities which can be determined from the experiments. In addition to different target thicknesses the program plots mainly one- and two-dimensional distributions of effective masses and of angular distributions for production and decay for the various photon-energy regions. For simple cases one calculates such experimental results as the total cross section and the decay correlations directly from the distributions. Extensive statistical analyses are carried out for some reactions with the aid of computer programs, for example to determine resonance production.

The procedures to determine the resonance production are described in the Appendix.

8. Measuring Accuracy

In the following section we discuss the accuracy of the reconstruction procedure and of the energy resolution for the reaction $\gamma p \rightarrow p\pi^+\pi^-$ and $\gamma p \rightarrow p\pi^+\pi^-\pi^o$.

The calculation of the particle masses from the measured (not yet improved by GRIND) track data allows a sensitive test of the accuracy of the total reconstruction procedure. The masses of the strange particles Λ^o and K^o, of the photon and of the ω-mesons are determined from the track data.

From 165 decays of K^o-mesons and 428 decays of Λ-hyperons one obtains the values of the masses $M_{K^o} = 500 \pm 0.3$ MeV, $M_{\Lambda o} = 1{,}116.2 \pm 0.13$ MeV [19]. The masses are slightly above values given in the tables ($M_{K^o} = 497.87 \pm 0.16$ MeV, $M_{\Lambda o} = 1115.58 \pm 0.10$ MeV) [25].

Fig. 10a shows the mean square value of the photon mass M_γ^2 in the reaction $\gamma p \rightarrow p\pi^+\pi^-$ for various regions of the chamber. The values are compatible with zero except for a point at the end of the chamber. The widths of the distributions of M_γ^2 represent a measure for the measuring accuracy. They are plotted in Fig. 10 as a function of the x-direction (beam direction) for two photon-energy intervals. The events in the rear part of the chamber (positive x-values of the event points) have on the average smaller track lengths than the events in the front part.

The width of the distribution of M_γ^2 does not depend on the location within the chamber for photon energies < 1.8 GeV, whereas for photon energies of $1.8 \text{ GeV} < E_\gamma < 5.8$ GeV the measuring accuracy decreases with increasing distance from the chamber entrance window.

Thus, the scanning region should be decreased for experiments with primary energies > 2 GeV.

The small deviations of M_γ^2, M_Λ and M_{K^o} from the nominal values are probably due to small irregularities in the measured values of the spatial magnetic field distribution in the bubble chamber.

The events of the reaction $\gamma p \rightarrow p\pi^+\pi^-\pi^o$ were recalculated with an improved magnetic field matrix. Table 7a shows the widths and masses of the ω-mesons which are produced in this reaction. The masses agree within the uncertainties with the table values (738.4 ± 0.7 MeV) [25]. The experimental half-width of approximately 40 MeV can be reproduced by FAKE calculations.

The mass resolution in the reaction $\gamma p \rightarrow p\pi^+\pi^-$ was examined with FAKE calculations (production of a narrow $\pi\pi$-resonance at 760 MeV). It is 17 MeV and is only weakly dependent on the photon energy.

The resolution of the photon energy in the reactions $\gamma p \rightarrow p\pi^+\pi^-$ and $\gamma p \rightarrow p\pi^+\pi^-\pi^o$ are shown in Table 7b for various primary energies. The resolution of the photon energy is 2-3% for the reaction $\gamma p \rightarrow p\pi^+\pi^-$ (full half-width).

Table 7: Mass- and Photon-Energy-Resolution in the Reactions $\gamma p \rightarrow p\pi^+\pi^-$, $\gamma p \rightarrow p\pi^+\pi^-\pi^o$

a. Mass Resolution

Final state	E_γ [GeV]	M Resonance Mass	Γ Full Width at Half Height [MeV]	ΔM Mass Resolution (full Width) [MeV]	Evaluation Method
$\underbrace{p\pi^+\pi^-}_{\rho}$	2			16	FAKE
	4			18.5	FAKE
$\underbrace{p\pi^+\pi^-\pi^o}_{\omega}$	1.1-1.4	784 $\pm$ 2.5	45 $\pm$ 5.8		Fitting to the Experiment+)
	1.4-1.8	789.5 $\pm$ 2	37 $\pm$ 4.6		
	1.8-2.5	786.8 $\pm$ 1.6	35 $\pm$ 3.4		
	2.5-3.5	784.1 $\pm$ 2.7	43 $\pm$ 6.2		
	3.5-5.8	791.6 $\pm$ 2.5	34 $\pm$ 5.9		
$\underbrace{p\pi^+\pi^-\pi^o}_{\eta}$	0.75 u. 0.9			15	FAKE
$\underbrace{p\pi^+\pi^-\pi^o}_{\omega}$	2		39		FAKE
	4		48		FAKE

b. Photon-Energy Resolution

Final State	E_γ [GeV]	ΔE_γ Full Width at Half Height [MeV]	Evaluation Method
$p\pi^+\pi^-$	0.75	25	
	2.0	40	FAKE
	4.0	100	
$p\pi^+\pi^-\pi^o$	0.75	30	
	2.0	90	FAKE
	4.0	270	

Table 7: continued

+) The mass distribution was fitted with a Gaussian function. In addition to the given statistical errors a systematic error enters during the evaluation of the mass values because the flanks of the experimental mass distribution do not have a Gaussian distribution and because the behavior of the background is not accurately known. Note the correlation between the fitted mass values and the fitted width.

9. Computation of the Cross Sections

9.1. Procedure. The cross sections must be averaged over photon energy intervals since the photons do have a continuous energy spectrum.

If N events of a certain type are produced in the photon energy interval $(E_\gamma, \Delta E_\gamma)$ then the cross section for the reaction becomes

$$\sigma(E_\gamma) = \frac{N(E_\gamma, \Delta E_\gamma)\cdot \Delta E_\gamma}{N_\gamma(E_\gamma, \Delta E_\gamma)\cdot M\cdot L\cdot \Delta E_\gamma} \qquad (5)$$

where $\sigma(E_\gamma)$ = cross section averaged over the energy intervals $(E_\gamma, \Delta E_\gamma)$

$N(E_\gamma, \Delta E_\gamma)$ = number of events in the energy intervals $(E_\gamma, \Delta E_\gamma)$

$N_\gamma(E_\gamma, \Delta E_\gamma)$ = number of incoming γ-quanta in the energy intervals $(E_\gamma, \Delta E_\gamma)$

M = number of protons/cm^3

L = length of the scanning region (cm)

The γ-flux $N_\gamma(E_\gamma, \Delta E_\gamma)$ is obtained by measuring and counting electron-positron pairs.

$$N_\gamma(E_\gamma, \Delta E_\gamma) = \frac{N_{pair}(E_\gamma, \Delta E_{pair})}{\sigma_{pair}(E_\gamma)\cdot M\cdot L}\ \frac{\Delta E_\gamma}{\Delta E_{pair}} \qquad (6)$$

where $N_{pair}(E_\gamma, \Delta E_{pair})$ = total number of pairs in the energy interval $(E_\gamma, \Delta E_{pair})$

$\sigma_{pair}(E_\gamma)$ = cross section for pair production in hydrogen

The cross section for pair production can be computed by means of quantum electrodynamics to an accuracy of a few per cent. The calculation is described in the next section.

From Eqs. (5) and (6) follows:

$$\sigma(E_\gamma) = \frac{N(E_\gamma, \Delta E_\gamma)\ \Delta E_{pair}}{N_{pair}(E_\gamma, \Delta E_{pair})\ \Delta E_\gamma} \cdot \sigma_{pair}(E_\gamma) \quad . \tag{7}$$

The proton density and the length of the scanning region cancel.

It is not necessary to determine the number and energy distribution of pairs on each single picture. One obtains the average number of pairs per picture $\bar{n}_{pair}$ sufficiently accurately by counting the pairs in each 100th useful picture. The number of pairs on Z pictures is then

$$Z \cdot \bar{n}_{pair}.$$

The energy distribution of the pairs is obtained from the energy distribution of the measured pairs normalized to one pair:

$$N_{pair}(E\gamma, \Delta E_{pair}) = Z \cdot \bar{n}_{pair} \frac{N_{pair}^{meas}(E_\gamma, \Delta E_{pair})}{N_{pair}^{meas,\ tot}} \tag{8}$$

where Z = number of evaluated pictures

$\bar{n}_{pair}$ = average number of pairs per picture

$N_{pair}^{meas}(E_\gamma, \Delta E_{pair})$ = number of measured pairs in the energy interval $(E_\gamma, \Delta E_{pair})$

$N_{pair}^{meas,\ tot}$ = total number of measured pairs.

The substitution of Eq. (8) into (7) yields the cross section.

$$\sigma(E_\gamma) = \frac{N(E_\gamma,\ \Delta E_\gamma)}{Z\ \bar{n}_{pair}\Delta E_\gamma} \quad \frac{N_{pair}^{meas,\ tot}\ \sigma_{pair}(E_\gamma)\ \Delta E_{pair}}{N_{pair}^{meas}\ (E_\gamma,\ \Delta E_{pair})}$$

One can define a flux function F (E_γ).

$$F\ (E_\gamma) = \frac{N_{pair}^{meas,\ tot}\ \sigma_{pair}\ (E_\gamma)\ \Delta E_{pair}}{N_{pair}^{meas}\ (E_\gamma,\ \Delta E_{pair})} \qquad (9)$$

F (E_γ) represents essentially the reciprocal of the γ-flux. One obtains then

$$\left\| \sigma(E_\gamma) = \frac{N(E_\gamma,\ \Delta E_\gamma)\quad F\ (E_\gamma)}{Z\ \bar{n}_{paar}\quad \Delta E_\gamma} \cdot \right\| \qquad (10)$$

Eq. 10 is sufficiently accurate for small energy intervals ΔE_γ if one uses the value of F at the center of the interval. For larger energy intervals one has to weight $F(E_\gamma)$ with the energy distribution of the events:

$$\overline{F\ (E_\gamma)} = \frac{\int_{E_\gamma - \Delta E_\gamma/2}^{E_\gamma + \Delta E_\gamma/2} \frac{dN\ (E)}{dE}\ F\ (E)\ dE}{\int_{E_\gamma - \frac{\Delta E_\gamma}{2}}^{E_\gamma + \Delta E_\gamma/2} \frac{dN\ (E)}{dE}\ dE}$$

9.2. Cross Sections for Electron-Positron Pair Production.

9.2.1. Cross Sections According to Wheeler and Lamb.

The interactions with the nuclear field (coherent production) and the interactions with the field of the shell electron (incoherent production)* contribute approximately equally to pair

*Incoherent production exists if during pair production the shell electron is raised to an excited state.

in hydrogen. In principle the processes can be exactly calculated by means of quantum electrodynamics.

However, the numerical treatment of the higher order corrections presents difficulties. There exists extensive literature on this subject.

We have calculated the cross section for pair production according to Wheeler and Lamb [26].

Wheeler and Lamb consider the contributions of the Bethe-Heitler graphs

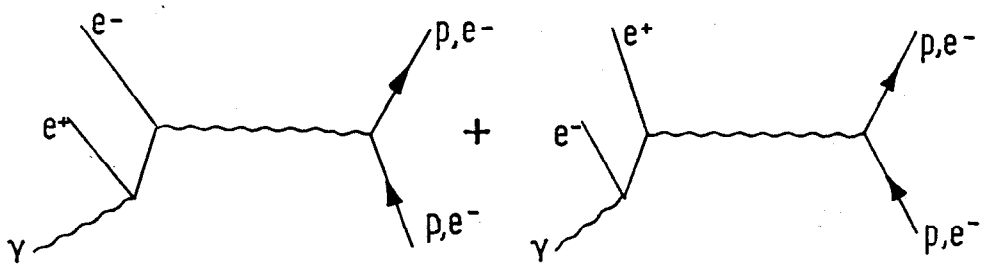

for pair production in hydrogen and they introduce the reciprocal screening of shell and nucleus by means of hydrogen form factors.

Wheeler and Lamb gave the differential cross sections Φ_p, Φ_e for coherent and incoherent pair production in hydrogen as follows:

$$\phi_p = Z^2 \alpha r_o^2 \frac{dE_+}{E_\gamma^3} \left\{ \left[E_+^2 + E_-^2 \right] \left[\phi_1(\gamma) - \frac{4}{3} \ln Z \right] + \frac{2}{3} E_+ E_- \left[\phi_2(\gamma) - \frac{4}{3} \ln Z \right] \right\} \tag{11}$$

$$\phi_e = Z \alpha r_o^2 \frac{dE_+}{E_\gamma^3} \left\{ \left[E_+^2 + E_-^2 \right] \left[\psi_1(\varepsilon) - \frac{8}{3} \ln Z \right] + \frac{2 E_+ E_-}{3} \left[\psi_2(\varepsilon) - \frac{8}{3} \ln Z \right] \right\} \tag{12}$$

with Z = 1 nuclear charge

$\alpha \simeq \frac{1}{137}$

$r_o = \frac{e^2}{mc^2}$ classical electron radius

$E \pm$ = total energy of $e^{\pm}$

E_γ = photon energy

$$\left.\begin{aligned} \gamma &= \frac{100\ mc^2\ E_\gamma}{E_+ E_-\ Z^{1/3}} \\ \epsilon &= \frac{100\ mc^2 E_\gamma}{E_+ E_-\ Z^{2/3}} \end{aligned}\right\} \quad \text{Screening parameter}$$

m = electron mass

The distribution of $\Phi(\gamma)$ and $\Psi(\epsilon)$ is given in [26] for $\gamma \leq 1.5$, $\epsilon \leq 1.5$. For $\epsilon >> 1.5$, $\gamma >> 1.5$, one has according to Rossi [27]

$$\phi_{e,p} = \alpha r_o^2 \frac{dE_+}{E_\gamma^3}\ 4 \left[E_+^2 + E_-^2 + \frac{2}{3} E_+ E_-\right] \left[\ln \frac{2E_\gamma}{m}\ E_+ E_- - \frac{1}{2}\right]. \qquad (13)$$

The total cross sections for pair production, σ_p and σ_e, on the proton and the electron respectively are obtained by numerical integration of Eqs. (11), (12) and (13).

Fig. 11 and Table 8 show the behavior of σ_e and σ_p and the sum $\sigma_p + \sigma_p$ for photon energies from 100 MeV to 6 GeV.

The curve $\sigma_p + \sigma_e$ agrees within the experimental uncertainty of 3-5% with the measurements of Gates et al. [28] and Malamud [29].

The uncertainty of the theoretical cross sections is also of this order of magnitude.

In the following we discuss the effects neglected by Wheeler and Lamb.

Table 8: Cross Sections for Coherent (σ_p) and Incoherent (σ_e) Pair Production on Hydrogen according to Wheeler and Lamb

E_γ [GeV]	σ_p [mb]	σ_p acc. to Sørenssen (31)	σ_e [mb]	$\sigma_p+\sigma_e$ [mb]
0.1	6.09	5.99	6.09	12.19
0.15	6.76		6.81	13.57
0.2	7.15		7.30	14.45
0.25	7.45		7.66	15.11
0.3	7.66		7.95	15.61
0.35	7.84		8.18	16.02
0.4	7.97		8.39	16.36
0.45	8.09		8.56	16.65
0.5	8.19	8.12	8.70	16.88
0.6	8.33		8.93	17.27
0.7	8.45		9.12	17.57
0.8	8.55		9.27	17.82
0.9	8.63		9.39	18.02
1.0	8.69	8.63	9.50	18.20
1.5	8.90		9.86	18.77
2.0	9.00		10.07	19.08
2.5	9.07		10.21	19.28
3.0	9.11		10.30	19.42
3.5	9.15		10.38	19.52
4.0	9.17		10.43	19.60
4.5	9.19		10.47	19.66
5.0	9.21	9.19	10.51	19.72
5.5	9.22		10.54	19.76
6.0	9.23		10.57	19.80
6.5	9.24		10.59	19.83

9.2.2. Corrections to the Coherent and Incoherent Pair Production.

9.2.2.1. Screening and Molecular Structure. The accuracy of the screening correction depends on how accurate one can consider the wave functions of the atomic shell.

Wheeler and Lamb used wave functions for the hydrogen atom which were determined according to the principle of variation [30]. A. Sørenssen [31] has calculated the cross section for pair production on the proton using Hartree-Fock-Slater wave functions. The total cross sections obtained by Sørenssen agree within 1% with our values calculated according to Wheeler and Lamb.

Since molecular hydrogen was used in this experiment one must use wave functions of the H_2-molecule for an exact treatment.

Bernstein and Panofsky [32] have made an assessment of the reciprocal screening of electrons and nuclei in the H_2-molecule. They obtained a correction to the cross section for Bremsstrahlung as given by Wheeler and Lamb using molecular wave functions in the Heitler-London approximation for Bremsstrahlung.

$$\frac{\sigma\ (H_2) - 2\sigma(H)}{2\sigma\ (H)} = 0.027$$

where $\sigma\ (H_2)$ = cross section for Bremsstrahlung on H_2-molecule
$\sigma\ (H)$ = cross section for Bremsstrahlung on the H-atom according to Wheeler and Lamb for complete screening

The correction is supposed to be independent of energy for complete screening. For hydrogen one can calculate with complete screening above 500 MeV.

Molecular effects in pair production have not yet been calculated.

In this report we do not consider a correction for the molecular effects. The uncertainty thus introduced into the theoretical cross section is of the order of 2%.

9.2.2.2. Radiative Corrections. Contributions to the cross section due to higher order graphs are called radiative corrections. Mork and Olsen [33] have computed the radiative corrections for pair production according to the Weizsäcker-Williams method. For high energies they obtained a correction of +0.93% for all elements.

9.2.3. Corrections Influencing Only Incoherent Pair Production.

9.2.3.1. Treatment of the Recoil Electrons. Reactions with small momentum transfer $q \ll mc$ give the main contribution to the cross section at high energies. Wheeler and Lamb assumed that for $q \leq mc$ protons and electrons have the same recoil momentum distribution. They integrated only up recoil momenta of $q = mc$. Suh and Bethe [36] have shown, meanwhile, that the first assumption is justified.

9.2.3.2. Exchange Effects and γe-Interaction. Two electrons appear in the final state for pair production on the electron. The Pauli principle prohibits the two electrons from occupying the same state in the phase space. The cross section can be reduced due to that. This is effect is called the exchange effect. At high energies the exchange effect should only give a contribution for high momentum transfers $q \geq mc$. For small momentum transfers the struck electron and the pair electron are so far apart in phase space that the probability for reaction is not affected.

The contribution of the two Compton diagrams is denoted as γe-interaction:

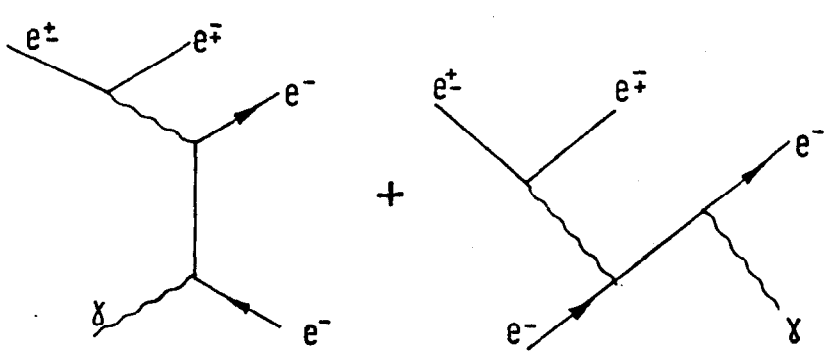

The γe-interaction increases the cross section. At high energies it gives significant contributions only for large momentum transfers.

Votruba [37] has treated the pair production on free electrons exactly. His treatment includes the exchange effects and the γe-interation but omits the screening. It is very difficult to integrate the multidifferential cross sections of Votruba without large approximations.

An exact treatment of the recoil distribution is essential.

Joseph and Rohrlich [38] have derived a recoil distribution for small momenta $q \ll mc$ using Votruba's treatment. For large momenta the results give an approximation.

Taking into consideration the screening on the H-atom Joseph and Rohrlich have computed cross sections for the electron by integration over the recoil momentum distribution from q_{min} to q_{max} which are significantly below the ones given by Wheeler and Lamb.

$$\frac{\sigma_{JR} - \sigma_{WL}}{\sigma_{WL}} = \frac{16 - 19}{19} = 0.16$$

where σ_{JR} = cross section for incoherent pair production according to Joseph and Rohrlich

σ_{WL} = cross section for incoherent pair production according to Wheeler and Lamb

This would mean a decrease of the total cross section for hydrogen by approximately 8.5% at $E_\gamma = 1$ GeV.

On the other hand, Suh and Bethe [36] estimate the relative contribution to the incoherent pair production for high energies from the exchange effect and the γe-interaction with $[\ln E_\gamma/mc^2]/[E_\gamma/mc^2]$. The expression is $< 1\%$ for $E_\gamma > 0.35$ GeV.

9.2.4. Summary. The cross section for pair production on the hydrogen atom was computed according to Wheeler and Lamb using the Born approximation. The effects neglected by Wheeler and Lamb (molecular effect, radiative corrections,

exchange effect, γe-interaction) have opposite signs and partly cancel each other.

The error in the cross section used should be less than 4% for the energies of interest in this report, $E_\gamma > 350$ MeV.

9.3. Determination of the Flux. The total flux is obtained by counting the total number of pairs on one in every 100 pictures. All films are scanned twice independently. The scanning losses for pairs are less than 0.5%. They are corrected for.

The statistical error in the counting of the pairs is less than 0.5% for the amount of film used in this work.

For the determination of the energy distribution of the pairs the following pair measurements were available: 1,940 measurements from section I of the experiment, 8,710 measurements from section II and 17,670 measurements from sections III and IV. The momentum resolution of the electron beam was 1%. The values of the beam energy were verified to less than 2% (standard deviation) by measuring beam tracks.

Two corrections must be introduced before a flux curve can be calculated:

1. Cut-off at $E_\gamma = 0.1$ GeV. The lower energy limit (~ 50 MeV) of the counted pairs was subject to fluctuations for technical reasons. Therefore, an abrupt limit was selected for the flux and pair spectra at 100 MeV. The flux is normalized (separately for each Institute) to energies larger than 100 MeV by means of the measured spectrum. The statistical uncertainty of the correction is approximately 0.8%.

2. Correction for pairs outside of the beam region. The beam region is defined by the size of the entrance window.

$$-10 \text{ cm} \leq y \leq +10 \text{ cm}$$
$$-25 \text{ cm} \leq z \leq -15 \text{ cm}$$

Events and pairs outside the beam region are due to secondary particles.

Approximately 1% of all pairs are located outside the beam region, compared to only 0.2% of all 3-track events. The total flux is therefore corrected for the pairs located outside. For reasons of simplification one combines the pair spectra from section I and II according to the flux ratio.

The measured pair spectra must be smooth in order to assure that the flux curve is steady.

The pair spectra in photon spectra are calculated by:

$$N_\gamma E_\gamma = \frac{N_{pair}^{meas}(E_\gamma, \Delta E_{pair})E_\gamma}{\sigma_{pair}(E_\gamma) N_{pair}^{meas,\ tot}} \cdot \frac{flux}{const}$$

$$flux = \bar{n}_{pair} \cdot Z$$

The pairs located above the cut-off energy due to the finite measuring accuracy are folded back. Next, the photon spectra are smoothed using continuous curves which have approximately the same behavior at the energy limit as the theoretical radiation spectrum.

The smooth curves are added (according to the flux ratio). Using Eq. (9) one obtains the flux function from the sum.

Fig. 12 shows the behavior of the flux functions. The steep increase between 5.4 and 5.5 GeV is due to the "Brems edge" of the spectrum from section I and II.

The uncertainty of the flux function due to limited statistics in the pair measurements and due to blurriness of the limiting energy is approximately 2% for $E_\gamma < 3.5$ GeV, 5% for 3.5 GeV $< E_\gamma \leq 5$ GeV and 10% for $E_\gamma > 5$ GeV.

9.4. Corrections and Systematic Errors. In the following section we discuss the possible sources of errors in the calculation of cross sections. The estimates for the errors are summarized in Table 9. They are separated for the flux determination and the selection of events.

The accuracy of the pair-production cross section enters most strongly into the error of the flux determination with

3-5%. Furthermore, at high energies the uncertainty due to smoothing of the measured pair spectrum enters with approximately 5-10%. The remaining sources of errors, however, are negligible.

The contamination of the bubble chamber with heavy elements (mainly N_2, O_2, Ne, Ar with a frequency of $\leq$ 0.005 % by volume [39]) gives a small contribution of $\leq$ 0.25% to the pair production; it can be neglected.

Statistical errors generally predominate in the selection of events. They are not shown in Table 9.

For the discussion of the remaining sources of errors we concentrate on the 3-track events.

Table 9: Error Estimation for the Calculation of the Cross Sections

1. Flux Determination

Statistical error for pair production	$\leq$ 0.5%
Accuracy for normalization to pairs above 0.1 GeV	0.8%
Systematic errors in the counting of pairs:	
a. Scanning losses	$\leq$ 0.5%
b. Pair production in heavy nuclei	$\leq$ 0.25%
Uncertainty of the γ-spectrum:	
a. Uncertainty due to the smoothing of the measured pair spectrum	2% for E_γ < 3.5 GeV 5% for 3.5<E_γ<5 GeV 10% for E_γ < 5 GeV
b. Accuracy of the pair-production cross section	3-5%

2. Selection of Events

3-Track Events	Final State			
	All 3-Track Events	$p\pi^+\pi^-$	$p\pi^+\pi^-\pi^o(\pi^o..)$	$n\pi^+\pi^+\pi^-(\pi^o..)$
a. Scanning losses*	< 0.5 %	< 0.5 %	< 0.5 %	< 0.8 %
b. Events on heavy nuclei	0.1 %	< 0.1 %	$\leq$ 0.3 %	$\leq$ 0.1 %
c. Reactions of neutrons	$\lesssim$ 0.25 %	< 0.1 %	$\leq$ 0.6 %	$\leq$ 0.3 %

	All 3-Track Events	$p\pi^+\pi^-$	$p\pi^+\pi^-\pi^o(\pi^o..)$	$n\pi^+\pi^+\pi^-(\pi^o..)$
d. Electron pairs and μ-pairs with visible protons	0.5 %	< 0.1 %	-	-
e. Events with neutrally decaying strange particles	0.5 %	< 0.1 %	≤ 1 %	≤ 0.5 %
f. Addition from $pK^+K^-\pi^o$ to group $p\pi^+\pi^-\pi^o$	-	-	≤ 1 %	-
g. Simulation and loss of hypotheses during the kinematic fitting		< 1 %	~1 %	< 1 %
h. Uncertainty in the division of no-fit events		0.3 %	~1 %	~1 %
i. Uncertainty in the division of unmeasurable events.		≤ 1.5 %	≤ 4 %	≤ 5 %
j. Portion of multi-neutral events			20-50 %	20-50 %
k. Portion of the true events $p\pi^+\pi^-\pi^o$ with wronly calculated photon energy			(10-15 %)	

The portions are based on the number of events in the corresponding final state.

5-Track Events

	$p\pi^+\pi^+\pi^-\pi^-$	$p\pi^+\pi^+\pi^-\pi^-\pi^o(\pi^o..)$	$n\,3\pi^+\,2\pi^-(\pi^o..)$
Uncertainty in the division of unmeasurable events	~5 %	~5 %	~5 %
Simulation and loss of hypotheses during kinematic fitting	< 1 %	~1 %	< 1 %
Portion of the multi-neutral events	-	20-50 %	20-50 %

*Except for scanning losses from events with very short proton tracks. These losses are discussed on page 64.

a. After two scanning procedures the scanning losses are 0.3-0.5% for events with a proton and 0.8-1% for events without a proton. They will be corrected.

b. Events on heavy nuclei. Based on impurities in the bubble chamber one expects 0.1% 3-track events on heavy nuclei. The number of reactions found with even track numbers which cannot occur on the proton is compatible with the indicated rate.

c. Events due to neutrons. The neutron flux is only interesting above the π-production threshold at 800 McV/c.

The neutron flux from the beam-hardener is negligible due to the small acceptance of approximately 6 mrad. The latter is fixed by the distance and the aperture of cleaning and bending magnets. The neutron flux due to photon reactions in the entrance window and in the fluid of the chamber can be estimated if one assumes that the neutrons above 800 MeV/c have a momentum and angular distribution similar to that of the protons produced in the chamber. One expects that less than 0.25% 3-track reactions were due to neutrons.

d. Electron pairs and μ-meson pairs with visible proton. High-energy electron pairs and μ-meson pairs with visible recoil proton cannot be separated based on the ionization. FAKE calculations have shown that a small part of these events is interpreted by the kinematic program with the hypothesis $p\pi^+\pi^-$. The remaining events do not fit any hypothesis and enter into the no-fit group.

The cross section for both processes is estimated at $\leq$ 0.2 μb. This effect is negligible since only a part of the events receives the hypothesis $p\pi^+\pi^-$.

e. Events with neutrally-decaying strange particles constitute approximately 0.5% of the 3-track events.

f. The portion of the reactions $pK^+K^-\pi^o$ which cannot be separated from the group $p\pi^+\pi^-\pi^o$ based on the ionization is less than 1%.

g. The losses and the simulation of hypotheses during the kinematic fitting was estimated by means of FAKE calculations.

The effects are less than 1% for the reaction $\gamma p \rightarrow p\pi^+\pi^-$.

h. Division of the no-fit events. The effective mass distributions $M_{p\pi^+}$, $M_{p\pi^-}$, $M_{\pi^+\pi^-}$ of the no-fit events were examined to subdivide them. One observes the weak production of the resonances N^{*++} and ρ^o. Since the resonances N^{*++} and ρ^o are frequent in the channel $p\pi^+\pi^-$ and since they are hardly produced at all in the other channels one can estimate the portion of the final state of $p\pi^+\pi^-$ using the no-fit events. It comes to $(25 \pm 12)\%$. Of the remaining no-fit events with the proton $(35 \pm 15)\%$ were classified as reactions of the type $p\pi^+\pi^-\pi^o(\pi^o..)$ and 40% as electron pairs. The no-fit events without the proton were added to the group $n\pi^+\pi^+\pi^-(\pi^o..)$.

i. The unmeasureable events are split up according to the branching ratios of the measurable events.* The errors thus introduced are $\leq 1.5\%$ for the channel $p\pi^+\pi^-$ and $\leq 4\%$ for the channel $p\pi^+\pi^-\pi^o$.

j. Portion of the multineutral events. The principal difficulty in this experiment is due to the fact that one cannot kinematically distinguish between the final states with one or several neutral particles. Only one neutral particle is fitted even for multineutral events. The photon energy is then computed wrong -- generally too low. Events with one neutral particle are calculated properly, however, especially if a resonance is produced. Crouch et al. [2d] have tried to evaluate the portion of the events with several π^o-mesons among those events which were decided as being $p\pi^+\pi^-\pi^o(\pi^o..)$. They used statistical analyses of the

*A sufficiently accurate measurement is often not possible due to technical or geometrical reasons (such as steep tracks, secondary interactions). The effect should not depend strongly on the type of event in the case of 3- and 5-track events since the resulting tracks have similar angular distributions and cross sections.

angular distribution of the π-mesons in the laboratory. Crouch et al. report a contribution of 47%.

We do not try to make a separation of this contribution due to the uncertainty of the method and we give only upper limits for the cross sections of the reaction $\gamma p \rightarrow p\pi^+\pi^-\pi^o$.

The portion of the multineutral events in a bubble chamber experiment can be determined with energy-tagged photons.

Similar considerations hold for the reaction $\gamma p \rightarrow n\pi^+\pi^+\pi^-(\pi^o..)$.

k. Falsification of the photon energy for events $\gamma p \rightarrow p\pi^+\pi^-\pi^o$.

The energy of the π^o-meson and the photon is calculated wrong for part of the events $\gamma p \rightarrow p\pi^+\pi^-\pi^o$ if the π-meson is emitted close to the forward direction, i.e. with small cross momentum. The relative error of the calculated cross momentum of the π^o-meson $\Delta p+/p+$ can assume large values for such events due to measuring errors of the charged tracks and due to lack of knowledge about the exact photon direction. Since the measured values of the charged tracks are at the same time scattered about the true value one can get under certain circumstances significant deviations of the cross- and the total momentum of the π^o-meson from the true value.

We have reproduced this effect with FAKE calculations and we estimate the portion of the events with a wrongly-calculated photon energy at 10-15%, based on the number of true $p\pi^+\pi^-\pi^o$ events.

Only the most important sources of errors are given for the 5-track events.

An uncertainty of 5% appears for the reaction $\gamma p \rightarrow p\pi^+\pi^+\pi^-\pi^-$ due to the division of the unmeasurable events according to the branching ratios of the measurable events.

Based on the number of 7-track events we estimate the portion of multineutral events for the reactions

$\gamma p \rightarrow p\pi^+\pi^+\pi^-\pi^-\pi^o(\pi^o..)$ and $\gamma p \rightarrow n\pi^+\pi^+\pi^+\pi^-\pi^-(\pi^o..)$ at 20-50%.

We summarize:

1. The cross sections for the reactions $\gamma p \rightarrow p\pi^+\pi^-$ and $\gamma p \rightarrow p\pi^+\pi^+\pi^-\pi^-$ can be determined relatively accurately. Below 5 GeV the systematic errors are $\leq 7\%$.
2. Only upper limits can be given for the total cross sections of the reactions $\gamma p \rightarrow$
   $p\pi^+\pi^-\pi^o$
   $n\pi^+\pi^+\pi^-$
   $p\pi^+\pi^+\pi^-\pi^-\pi^o$
   $n\pi^+\pi^+\pi^+\pi^-\pi^-$
   due to the uncertainty of the contribution from multineutral events.

The accuracy with which the cross section for the reaction $\gamma p \rightarrow p\pi^+\pi^-$ can be determined is essentially limited by the uncertainty of the cross section for pair production. It would be desirable if the cross section for pair production could be measured with higher accuracy in future bubble-chamber experiments with high statistics (for example, examination of higher nucleon resonances in the reaction $\gamma p \rightarrow p\pi^+\pi^-$ with polarized γ-beams). An apparatus similar to the one given by E. Malamud [29] could be used (hydrogen target, pair spectrometer and absolutely-calibrated quantameter).

III. RESULTS: PHOTOPRODUCTION OF ρ^o-MESONS ON PROTONS

The following five sections contain the experimental results. The cross sections for multiple pion production are given in III.1. The effective mass distributions of the reaction $\gamma p \rightarrow p\pi^+\pi^-$ are examined in III.2. Section III.3 contains the total and differential cross sections for the ρ^o-production. The angular decay distributions of the ρ^o-mesons are given in III.4 and various interference effects are analyzed in III.5. The results are always discussed in the second part of each section.

1. Total Cross Sections

Table 10 shows the number and the branching ratios for events with 3 and more resulting tracks. Only the amount of film fully evaluated by June 1966 is considered (except for the 7-track events). The total cross sections of the individual final states* are computed according to the procedure described in II.9. The errors were discussed in detail in II.9.4.

Table 10: Number and Branching Ratios of the 3-, 5- and 7-Track Events without Strange Particles

Event Numbers

3-Track Events		5-Track Events	7-Track Events	No. of Pertinent Pairs with $E_\gamma > 0.1$ GeV	No. of Equivalent+quanta with $E_\gamma > 0.1$GeV
Found	Corrected **				
14,740	14,800	807		$5.636 \cdot 10^6$	$4.07 \cdot 10^7$
			52	$11.407 \cdot 10^6$	

+calculated with:
radiation length of H_2 = 58 g/cm^2 ≙ 990 cm
length of scanning region = 47 cm

---

*Upper limits for the cross sections of the reactions $\gamma p \rightarrow p\pi^o$, $\gamma p \rightarrow n\pi^+$ were given [4] in a preliminary evaluation of 1-track events. For the latter there exists the principal difficulty that one cannot kinematically rule out the production of several neutral particles. Meanwhile, the results of counts with high statistics for the reactions $\gamma p \rightarrow p\pi^o$ and $\gamma p \rightarrow n\pi^+$ exist [40]. Therefore, we do not further treat the 1-track events. The values published in [4b] are corrected for scanning losses and events outside the beam region (by secondary neutrons).

**Without correction of the scanning losses of events with very short proton tracks. These losses are discussed on p. 64.

Table 10: continued

Branching Ratios

3-Track Events*

Final State	Portion %	Portion without Nonmeasurables after Division of No-Fits	Number	Available for Plots
a) $p\pi^+\pi^-$	60.03	61.91	9,163	8,445
b) $p\pi^+\pi^-\pi^o(\pi^o..)$	22.46	23.56	3,487	
c) $n\pi^+\pi^+\pi^-(\pi^o..)$	9.99	10.32	1,527	
d) Ambiguity b)/c)	4.11	4.21	623	
e) No-fit with proton	1.53			
f) No-fit without proton	0.08			
g) Not measurable	1.8			
Sum	100.	100.	14,800	

5-Track Events

Final State	Portion (%)	Portion (%) without Nonmeasurables after Division of No-Fits
a) $p\pi^+\pi^+\pi^-\pi^-$	30.51	32.8
b) $p\pi^+\pi^+\pi^-\pi^-\pi^o(\pi^o..)$	32.73	35.15
c) $n\pi^+\pi^+\pi^+\pi^-\pi^-(\pi^o..)$	16.15	17.28
d) Ambiguous between b) and c)	13.92	14.77
e) No-fit with proton	0.79	
f) No-fit without proton	0.13	
g) Not measurable	5.77	
Sum	100.	100.

*Without correction for the scanning losses of events with very short proton tracks. These losses are discussed on p. 64.

1.1. The reactions $\gamma p \rightarrow p\pi^+\pi^-$, $\gamma p \rightarrow p\pi^+\pi^+\pi^-\pi^-$, $\gamma p \rightarrow p3\pi^+3\pi^-$.
The reactions without neutral particles in the final state are kinematically overdetermined by three secondary conditions. Their photon energy and the other kinematic quantities can be evaluated with high accuracy. Figs. 13 and 14c, f, show the behavior of the cross section for the reaction $\gamma p \rightarrow p\pi^+\pi^-$, $\gamma p \rightarrow p\pi^+\pi^+\pi^-\pi^-$ and $\gamma p \rightarrow p3\pi^+3\pi^-$. The given errors are statistical. The systematic errors are below 7% for $E_\gamma < 5$ GeV and approximately 10% for $E_\gamma > 5$GeV.

The cross section for reactions $\gamma p \rightarrow p\pi^+\pi^-$ increases above the threshold of 80 μb and shows a weak structure between $E_\gamma = 0.6$ and 1.0 GeV. The steep increase in mainly caused by the threshold behavior of the reaction $\gamma p \rightarrow N^{*++}_{1236}\pi^-$ (dotted curve in Fig. 13) [4e]. The structure could depend on the formation of higher nuclear resonances in the s-channel [41]. Our photon-energy resolution is 25 MeV in this region. Earlier measurements of the total cross section $\gamma p \rightarrow p\pi^+\pi^-$ by Crouch et al. [2d] and Hauser [42] are compatible with our results, whereas the measurements by Allaby et al. [43] between 0.6 and 0.9 GeV do not agree.

The cross sections for $\gamma p \rightarrow p\pi^+\pi^+\pi^-\pi^-$ and $\gamma p \rightarrow p3\pi^+3\pi^-$ increase slightly above the threshold and reach 5 and 0.6 μb respectively at 5 GeV.

1.2. Cross Sections for Events with Neutral Particles in the Final State. The photon energy can only be computed correctly in this experiment if not more than one neutral particle is emitted. Only one neutral track is fitted for events with more than one neutral particle. The photon energy is then computed incorrectly -- generally too low. One cannot not separate the multi-neutral events from events with one neutral particle. Therefore we report only upper limits for the cross sections of the reactions $\gamma p \rightarrow p\pi^+\pi^-\pi^0$, $\gamma p \rightarrow n\pi^+\pi^+\pi^-$, $\gamma p \rightarrow p\pi^+\pi^+\pi^-\pi^-\pi^0$, $\gamma p \rightarrow n\pi^+\pi^+\pi^+\pi^-\pi^-$. The portion of the multi-neutral events in the given cross-sections is at 20-50%. Figs. 14a, b, d, e, show the upper limits for the cross sections of the four mentioned reactions.

The ambiguous events were split up according to the ratio of the unequivocal events. No ambiguous events exist below E_γ = = 1.5 GeV. The portion of the multi-neutral events should be small in this case. Below 1.5 GeV we have entered instead of upper limits the values with statistical errors for the cross sections $\gamma p \rightarrow p\pi^+\pi^-\pi^o$ and $\gamma p \rightarrow n\pi^+\pi^+\pi^-$.

The cross section for $\gamma p \rightarrow p\pi^+\pi^-\pi^o$ increases steeply at 0.71 GeV. This is the location where the reaction $\gamma p \rightarrow p\eta$ has its threshold and supplies the main contribution to the cross section [4d]. On the other hand, the cross section of the reaction $\gamma p \rightarrow n\pi^+\pi^+\pi^-$ has a flat increase.

1.3. Predictions of the Vector-Dominance Model. The cross sections for the final state with equal particle numbers can be compared to each other and to corresponding cross sections for π^+-p reactions.

According to the vector-dominance model [44] (VDM) the electromagnetic current j_μ couples to the vector-meson currents of the form:

$$j_\mu(x) = e \cdot \sum_V \frac{m_V^2}{2\gamma_V} j_\mu^V(x) \quad .$$

where: $V = \rho, \omega, \varphi$

m_V = mass of the vector mesons ρ^o, ω, φ

$\gamma_V^2/4\pi$ = γV coupling constant

In the VDM the photoproduction reactions are attributed to interactions of vector mesons on the nucleon.

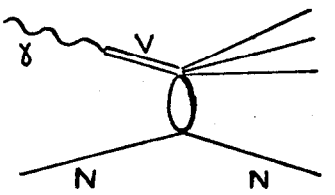

The total cross sections of vector mesons on the proton can be calculated by means of a quark model with spin-independent additive amplitudes [44]:

$$\sigma_{tot}(\rho^0 p) = \sigma_{tot}(\omega p) = \frac{1}{2}\left[\sigma_{tot}(\pi^+ p) + \sigma_{tot}(\pi^- p)\right] = \sigma_{tot}(\pi^0 p)$$

$$\sigma_{tot}(\varphi p) = 2\,\sigma_{tot}(K^+ p) + \sigma_{tot}(\pi^- p) - 2\,\sigma_{tot}(\pi^+ p)$$

The following values are obtained from the experimental $\pi^{\pm}p$ cross sections at 6 GeV [44]:

$$\sigma_{tot}(\rho^0 p) = \sigma_{tot}(\omega p) = \sigma_{tot}(\pi^0 p) = 27{,}3 \text{ mb}$$

$$\sigma_{tot}(\varphi p) = 10{,}1 \text{ mb}$$

[Tr. Note: commas in numerical material indicate decimal points.]

One neglects the small contribution of the φp-reactions and one can join the total cross section for photoproduction directly to the total π^0-cross section.

$$\sigma(\gamma p) \simeq \alpha\pi\left(\frac{1}{\gamma_\rho^2} + \frac{1}{\gamma_\omega^2}\right)\sigma(\pi^0 p) \qquad (14)$$

$$\alpha \simeq \frac{1}{137}$$

If one assumes further that the relationship $\sigma(\gamma p) \sim \sigma(\pi^0 p)$ holds not only for the total cross sections but also for the cross sections of equal final states, one can calculate the relative frequency of various particle combinations (N, π..) in the final states with equal particle numbers by means of the isospin invariance [45]. For the initial state one uses the isospin mixture $|\pi^0 p\rangle = \sqrt{\frac{2}{3}}\left|\frac{3}{2}\frac{1}{2}\right\rangle + \sqrt{\frac{1}{3}}\left|\frac{1}{2}\frac{1}{2}\right\rangle$.

We have calculated the isospin rates for the final states of γp-reactions with up to eight resulting particles according to Eq. (5) of [45]. Table 11 contains the numerical values. Resonance production was not considered.

The isospin rates for an initial isospin state $\sqrt{\frac{1}{2}}\left|\frac{3}{2}\frac{1}{2}\right\rangle + \sqrt{\frac{1}{2}}\left|\frac{1}{2}\frac{1}{2}\right\rangle$ differ by less than 5% for the given rates except for 2-particle reactions. The reported isospin rates thus depend

only weakly on the assumptions made above.

Table 11: Isospin Weights for Final States with Equal Number of Particles

A mixture of $\sqrt{\frac{2}{3}}\left|\frac{3}{2}\,\frac{1}{2}\right\rangle + \sqrt{\frac{1}{3}}\left|\frac{1}{2}\,\frac{1}{2}\right\rangle$ was assumed as initial isospin state (γp).

p = proton, n = neutron, + = π^+-meson, - = π^--meson, o = π^o-meson

Final State	Weight	Final State	Weight
po	55.5	poo	14.4
n+	44.5	p+-	43.4
		n+o	42.2
pooo	7.1	poooo	2.0
p+-o	47.1	p+-oo	32.0
n+oo	20.0	p++--	20.0
n++-	25.8	n+ooo	10.0
		n++-o	36.0
pooooo	0.8	poooooo	0.3
p+-ooo	18.7	p+-oooo	9.7
p++--o	33.5	p++--oo	33.8
n+oooo	4.2	p+++---	9.0
n++-oo	30.4	n+ooooo	1.8
n+++--	12.4	n++-ooo	20.8
		n+++--o	24.6
poooooo	0.1		
p+-ooooo	4.7		
p++--ooo	26.7		
p+++---o	20.8		
n+oooooo	0.7		
n++-oooo	12.5		
n+++--oo	28.8		
n+++----	5.7		

For primary energies above 3 GeV one obtains generally good predictions [46] for the final states with more than four particles using the isospin invariance. By means of the weights shown in Table 11 and the cross sections for the reactions $\gamma p \rightarrow p\pi^+\pi^+\pi^-\pi^-$ and $\gamma p \rightarrow 3\pi^+3\pi^-$ it is thus possible to estimate the contamination of the reactions a), b), d) and e) given in Fig. 14 by multi-neutral events. These questions are not further discussed. Extensive examinations of the cross sections for multi-particle production can be done in an experiment using energy-marked photons.

H. Satz [46] has combined the cross sections of γp- and $\pi^{\pm}p$-reactions using Eq. (14) and the assumptions made above. One obtains the cross sections for special $\pi^o p$-reactions, for example $\pi^o p \rightarrow p\pi^+\pi^+\pi^-\pi^-$, from the measured $\pi^{\pm}p$-cross sections by means of the isospin invariance. Good agreement is obtained between the values calculated according to Eq. (14) (dotted curves in Figs. 14c and 14f) and the values measured by us for the reactions $\gamma p \rightarrow p\pi^+\pi^+\pi^-\pi^-$ and $\gamma p \rightarrow p3\pi^+3\pi^-$.

2. Effective Mass Distributions

2.1. Determination of the Resonance Production. In the following, we limit ourselves to the reaction $\gamma p \rightarrow p\pi^+\pi^-$.

Figs. 15-17 show the distributions of the three invariant 2-particle masses $M_{p\pi+}$, $M_{p\pi-}$, and $M_{\pi+\pi-}$ for five energy intervals above 1.1 GeV. The curves denoted by the short dots give the mass dependency of the Lorentz invariant phase space. One observes strong reduction of the resonances N^{*++} and ρ^o in the $p\pi^+$- and $\pi^+\pi^-$-mass combinations respectively. Only weak indications exist in the $M_{p\pi^-}$-distribution for the resonance $N^{*o}(1236)$. Small deviations from the $\pi^+\pi^-$ phase space appear for the mass of the f^o-meson (1250 MeV). No sure evidence exists for the production of higher nuclear resonances.

The portions of the ρ^o- and N^*-production are determined by fitting procedures.

One observes the distribution of the events in the Dalitz

diagram, $M^2_{p\pi^+}$ vs. $M^2_{\pi^+\pi^-}$. One can write the following equation for the density distribution of the events having the photon energy E_γ in the Dalitz diagram:

$$dW = \left[A_{N^*} f_{N^*} (M_{p\pi^+}) + A_\rho f_\rho (M_{\pi^+\pi^-}) + A_{ps} f_{ps} \right] \frac{\pi^2}{4E^{*2}} dM^2_{p\pi^+} dM^2_{\pi^+\pi^-} dE_\gamma \qquad (15)$$

E^* = total energy in the center of mass system

The parameters A_{N^*}, A_ρ and A_{ps} are the portions of the N^*-, ρ^o- and background events ($A_{N^*} + A_\rho + A_{ps} = 1$). Relativistic Breit-Wigner expressions with energy-dependent widths* are used for the terms f_{N^*}, f_ρ according to Jackson [47]. The term f_{ps} reproduces the Lorentz invariant phase space distribution. One assumes for this statement that the various amplitudes contributing to the final state do not interfere with each other.

The expressions f_{N^*}, f_ρ, and f_{ps} are averaged over fixed photon energy intervals and normalized to 1.

We use the values $M_{N^*} = 1{,}236$ MeV and $\Gamma_{N^*} = 123$ MeV for the mass and width of the N^{*++} respectively.

The desired parameters are determined by fitting of the distributions to the experimental results. For this purpose we use both the maximum likelihood method and least squares fitting. The procedure is described in detail in the Appendix (A.3-A.5).

The fitting can be improved if one considers the angular decay distribution of the ρ-mesons in the helicity system. The helicity angle Θ_H is the angle between the resulting π^+-meson and the opposite direction of the resulting proton (i.e. the ρ-flight direction) in the rest system of the $\pi\pi$-mass combination. The cosine of the helicity angle can be expressed by the photon energy and the effective masses $M_{p\pi^+}$ and $M_{\pi^+\pi^-}$ (Appendix Eq. A.18).

$W(\Theta_H)$ is multiplied by the term f_ρ. The form of the

---

*The resonance production in πp and $K^+ p$ experiments can generally be well described with similar expressions. See, for example, [48, 49].

distribution of the helicity angle is relatively strongly influenced by the parameters A_{ps}, A_{N^*} and A_ρ below E_γ = 2 GeV. We use the experimentally-determined distributions of the decay angle for $W(\theta)$.

For the calculations in five photon energy intervals one initially retains as variables the mass and the width of the ρ-mesons, both separately and together. The values for the width fluctuate for the various fits between 112 and 198 MeV. In the following we will always use a fixed mean width of 146 MeV since the fitting of the ρ-width is strongly dependent on the behavior of the background, the resonance form of the ρ-meson, and the interference effects.

Figs. 15-17 show the fits with variable ρ-mass and fixed ρ-width. The dotted curve represents in each case the behavior of the Lorentz invariant phase space. The broken line is the sum of phase space and kinematic reflection of the resonances in the other mass combinations. The full curve gives the sum of all contributions.

Table 12 gives for each fit the corresponding resonance contributions, the values of the ρ^o-mass , χ^2, and the number of degrees of freedom.

The fitted values of the ρ^o-mass decrease from 760 MeV below 1.8 GeV to 726 MeV between 3.5 and 5.5 GeV. Similar effects were observed in other photoproduction experiments [2, 3].

We would like to emphasize however that the calculation of the ρ-mass values depends on the form of the resonance curve used and on the treatment of the background. Therefore, one cannot immediately compare the numbers from the various experiments.

The fits do not give good χ^2-values above 1.8 GeV. One observes that for the $\pi^+\pi^-$-mass distribution the experimental events are systematically above and below the fitted curves on the two flanks of the resonance respectively. First, above 1.8 GeV the resonance form according to Jackson does not give a good description of the photoproduction of ρ^o-mesons on hydrogen.

Some explanations of this effect are discussed in the following section.

Table 12: Portions of the Resonance Production for Fitting of Relativistic Breit-Wigner Expressions with Energy-Dependent Width (RESGAM Program)

Portions (%)

E_γ (GeV)	No. of Events	Phase Space	N^{*++}	ρ^o	m_ρ (MeV)	Distribution of decay angle of the ρ	χ^2	NF
1.1-1.4	1070	33.7 ± 3.4	38.2 ± 3.7	28.1 ± 2.9	761 ± 8	isotrop	99.9	110
1.4-1.8	880	33 ± 4	28.8 ± 2.5	38.2 ± 3.4	760 ± 7	$0.3+0.55\cdot\sin^2\Theta_H$	142.6	134
1.8-2.5	800	32.5 ± 4	18.2 ± 2.1	49.3 ± 3.4	747 ± 7	$\sin^2\Theta_H$	157.4	89
2.5-3.5	537	15.2 ± 4.8	13.1 ± 2.1	70.9 ± 4.5	746 ± 6	$\sin^2\Theta_H$	168.7	115
3.5-5.5	461	10.3 ± 4	10.7 ± 2	77.8 ± 4.3	726 ± 5	$\sin^2\Theta_H$	203.9	145

Fixed parameters: $M_{N^*} = 1{,}236$ MeV, $\Gamma_{N^*} = 123$ MeV, $\Gamma_\rho = 146$ MeV
NF = number of degrees of freedom
The portions are not corrected for scanning losses of events with very short proton tracks.

2.2. The Mass Distribution of the ρ-Mesons. Meanwhile, various experimental results have shown that the photoproduction of ρ^o-mesons on hydrogen is mainly dominated by diffractive processes.[2-4]. The weak energy-dependency of the total cross section, the behavior of the differential cross section and the decay angle distributions can be described better with a diffraction process than with an single pion exchange model. Using this as a basis, P. Söding [5] suggested an interference mechanism which gives an explanation for the deformation of the ρ-mass distribution.

Söding assumes that the amplitude T_ρ for the ρ-production is mainly absorptive.

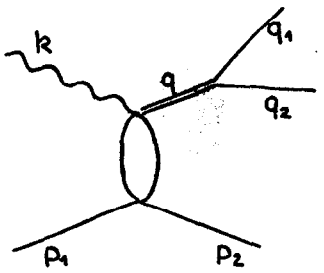

$$T_\rho \sim i \text{ const } \frac{1}{2}(s-m_N 2)\, e^{\frac{A}{2}t}$$

wo $s = (k + p_1)^2$

$t = (p_1 - p_2)^2$

m_N = proton mass

One can write the following for the matrix element:

$$M_1 \sim T_\rho \frac{1}{m_\rho{}^2 - m_{\pi\pi}{}^2 - i m_\rho \Gamma} \varepsilon_\mu^{(\gamma)}(k)\left[\delta_{\mu\nu} - \frac{q_\mu k_\nu}{(q\cdot k)}\right](q_{1\nu} - q_{2\nu}) \qquad (16)$$

where: Γ = energy-dependent width

m_ρ = ρ^o-mass

$m_{\pi\pi}^2 = (q_1 + q_2)^2$

$\varepsilon_\mu^{(\gamma)}(k)$ = polarization vector of the photon

One now considers Drell-type nonresonant processes in which $\pi\ \pi$ pairs are produced. Here the exchanged π-meson is scattered diffractively on the proton.

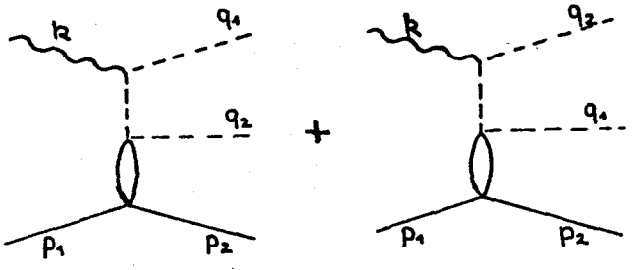

For the corresponding matrix elements one can write:

$$M_2 + M_3 \sim \varepsilon_\mu^{(\gamma)}(k)\left[\frac{T_-}{m_\pi^2 - t_1} q_{1\mu} - \frac{T_+}{m_\pi^2 - t_2} q_{2\mu}\right] . \qquad (17)$$

where $t_1 = (q_1 - k)^2$, $t_2 = (q_2 - k)^2$, m_π = π mass

$T_\pm$ are the amplitudes for the elastic $\pi^\pm$p-scattering:

$T_\pm \sim i e^{\frac{B}{2}t}$.

The diagrams M_2 and M_3 can interfere with the imaginary part of M_1.

$$\mathrm{Im}M_1 \sim \frac{m_\rho^2 - m_{\pi\pi}^2}{(m_\rho^2 - m_{\pi\pi}^2)^2 + m_\rho^2 \Gamma^2}$$

In the calculation of the cross section $d\sigma/dm_{\pi\pi}$ this leads to a contribution which changes rapidly close to the resonance mass and which produces a deformation of the ρ-mass distribution. The maximum appears at a smaller and larger value respectively due to the deformation (depending on the relative sign of the amplitudes T_ρ and $T_\pm$).

We have averaged the calculations of Söding for $d\sigma/dm_{\pi\pi}$ over various photon energy intervals. Furthermore, the mass dependency of the resonance, background and interference-term contributions were put in parameter form. The resulting expressions were fitted to the ππ-mass distribution. The portion of the background events (Dreel graph) was, for this case, not taken from the calculations by Söding but was fitted. We obtained a good description of the ρ-mass distribution at photon energies > 2.5 GeV. Especially the behavior on the flanks of the resonance is described correctly. Fig. 17a shows the fits for two photon-energy intervals above 2.5 GeV. The fits are not improved below 2 GeV. Moreover, one does not expect that the simplified assumptions of the Söding model still hold in this region.

If one also varies the ρ-mass* in the fits then a constant mass value of approximately 775 MeV is obtained above 1.4 GeV. The mass value does not vary with the photon energy. The mechanism suggested by Söding thus gives a qualitatively correct, consistent description of the experimental mass distribution.

Ross and Stodolsky [50] have examined the ρ^0-production

*Here the ρ-mass is the resonance mass, appearing in the matrix element M_1.

within the framework of the vector dominance model.

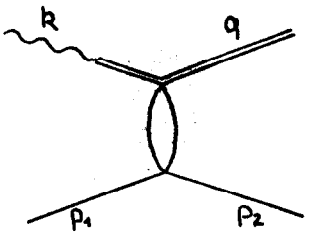

If one describes the coupling of the photon to the vector mesons by means of Feynman diagrams, a factor

$$-\frac{e m_V^2}{2\gamma_V}\,\frac{1}{K^2 - m_V^2}$$

where m_V = mass of the vector mesons, $K^2 = 0$, appears for the $\gamma\rho$-vertex and the ρ-line.

Ross and Stodolsky neglect the contributions of intermediate ω- and φ-mesons for the ρ-production. They limit themselves to small momentum transfers

$$\left|(p_1-p_2)^2\right| \ll m_V^2 .$$

They further assume that the effective $\pi^+\pi^-$-mass changes very little in the diffraction scattering of the incident virtual ρ-mesons on the proton. They write for the coupling

$$-\frac{e m_\rho^2}{2\gamma_\rho}\,\frac{1}{m_{\pi\pi}^2} .$$

A factor $m_\rho^4/m_{\pi\pi}^4$ appears then in the differential cross section $\frac{d\sigma}{dm_{\pi\pi}}$. The factor $m_\rho^4/m_{\pi\pi}^4$ leads to a deformation of the ρ-mass distribution and shifts the maximum to smaller values.

We have multiplied the Breit-Wigner resonance form by the factor $m_\rho^4/m_{\pi\pi}^4$ suggested by Ross and Stodolsky. One obtains good fits to the experimental $\pi^+\pi^-$-mass distribution for photon energies above 1.4 GeV. However, the fits do not give a fixed value of the ρ-mass which is independent of the photon energy.*

*We find decreasing mass values between (780 $\pm$4) MeV and (762 $\pm$5) MeV in the photon-energy intervals $1.4 < E_\gamma < 1.8$ GeV and $4.5 < E_\gamma < 5.8$ GeV, respectively.

The simplified formula by Ross and Stodolsky is not sufficient to consistently describe the experimental ρ-mass distributions at varying photon energies and for production angles outside the forward direction.

On the other hand, the mass distributions for the ρ-photoproduction on heavy nuclei and for small production angles are well described by the formulas suggested by Ross and Stodolsky, independently of the photon energy [65]. The following mass values are constant at 765-770 MeV which is in good agreement with the Table value [25].

If we limit ourselves to production angles close to the forward direction ($0.97 < \cos \theta_\rho^* < 0.99$) we obtain, using fits according to Ross and Stodolsky, mass values of 755 ±7 MeV for $2.5 < E_\gamma < 3.5$ GeV and 750 ±5 MeV for $3.5 < E_\gamma < 5.8$ GeV for ρ-production on hydrogen. Thus, the masses are approximately 15 MeV lower than in the ρ-photoproduction on heavy nuclei.

3. Cross Sections for ρ-Production

3.1. Total and Differential Cross Sections. We determine the cross section for ρ-production using the fitting procedure described in the previous section.

We use a Breit-Wigner resonance form according to Jackson [47] for the ρ-mass distribution in order to give a description of the data which is as independent of a model as possible. For the width Γ one uses 146 MeV and for the mass M_ρ fixed values are introduced, which are given in Table 12.

Fig. 18 shows the cross section for ρ-production as a function of the photon energy (full points) determined in this fashion.

The values obtained by means of the Breit-Wigner form are the cross sections corresponding to the area of the ρ-maximum minus the phase space and background events. Contributions due to interference effects and non-phase-space-distributed background can in this case be included under the Breit-Wigner curve of the ρ.

For comparison we have also used the parametric form of the

Söding interference model in order to determine the ρ-portion at high energies. (M_ρ = 775 MeV and Γ_ρ = 146 MeV were fixed in the fits.)

The open points in Fig. 18 show the cross sections above 2.5 GeV calculated in this manner. These points contain only the contribution of the resonant ρ-amplitude (diagram M_1, Eq. (16)). The contributions due to interference and background are separated. The values are therefore lower than the ones determined by the Breit-Wigner form. However, both methods lead to the same energy dependency of the ρ-cross section. The discrepancy between the results of the two methods indicates that the systematic error for the determination of the ρ-cross section above 2 GeV is of the order of 10-15%.

Theshold effects and possibly also influences of resonances in the s-channel make the analysis below 2 GeV more difficult. The separation of the resonances contains large errors since the resonances and their reflections are kinematically located close together. Below 2.5 GeV we limit ourselves to giving cross sections which were determined with the Breit-Wigner form.

The differential cross sections $d\sigma_\rho/d\Delta^2$ and $d\sigma_\rho/d\Omega$ were determined with the same fitting procedure (Breit-Wigner resonance form with fixed masses and widths).

Figs. 19 and 20 show the differential cross sections for four photon-energy intervals. Table 13 contains the numerical values for $d\sigma/d\Omega$.

The events with very small proton recoil track contain scanning losses. Especially the events with a proton momentum less than ~ 90 MeV/c (corresponding to a range of approximately 2 mm in the bubble chamber) are not contained.

The scanning losses appear at production angles of $\cos \Theta\rho^* > 0.99$. For the differential cross section $d\sigma/d\Omega$ only the first point contains scanning losses. The points close to the forward direction are not corrected.

We calculate the number of lost events assuming that the differential cross section $d\sigma/d\Delta^2$ can be described by an exponential law $Ae^{-B\Delta^2}$ to the smallest possible momentum

Table 13: Differential Cross Sections $\frac{d\sigma}{d\Omega}$ for the Reaction $\gamma p \rightarrow p\rho^o$

(Determined by fitting of a Breit-Wigner resonance form)

1.4 GeV < Eγ < 1.8 GeV				1.8 GeV < Eγ < 2.5 GeV			
$\cos\Theta^*_{min}$	$\cos\Theta^*_{max}$	$\frac{d\sigma}{d\Omega}^o \left[\frac{\mu b}{sr}\right]$	$\Delta(\frac{d\sigma}{d\Omega})$	$\cos\Theta^*_{min}$	$\cos\Theta^*_{max}$	$\frac{d\sigma}{d\Omega}^o \left[\frac{\mu b}{sr}\right]$	$\Delta(\frac{d\sigma}{d\Omega})$
0.975	1.0	9.65	3.3	0.975	1.0	15.7	2.9
0.9375	0.975	11.2	2.6	0.95	0.975	17.6	3.0
0.9	0.9375	4.08	2.1	0.9	0.95	12.0	1.8
0.85	0.9	7.96	1.8	0.85	0.9	6.6	0.86
0.8	0.85	9.28	1.8	0.775	0.85	4.6	0.86
0.7	0.8	3.12	0.8	0.7	0.775	4.4	0.83
0.3	0.7	1.31	0.3	0.4	0.7	0.89	0.24
-0.2	0.3	0.83	0.22	-0.3	0.4	0.28	0.10
-1.0	-0.2	0.11	0.11	-1.0	-0.3	0.098	0.08

2.5 GeV < Eγ < 3.5 GeV				3.5 GeV < Eγ < 5.8 GeV			
$\cos\Theta^*_{min}$	$\cos\Theta^*_{max}$	$\frac{d\sigma}{d\Omega}^o \left[\frac{\mu b}{sr}\right]$	$\Delta(\frac{d\sigma}{d\Omega})$	$\cos\Theta^*_{min}$	$\cos\Theta^*_{max}$	$\frac{d\sigma}{d\Omega}^o \left[\frac{\mu b}{sr}\right]$	$\Delta(\frac{d\sigma}{d\Omega})$
0.975	1.0	24.6	3.05	0.985	1.0	36.5	4.1
0.95	0.975	26.6	4.2	0.975	0.985	53.0	6.4
0.9	0.95	13.4	1.65	0.95	0.975	24.0	2.6
0.85	0.90	7.01	1.15	0.9	0.95	9.4	1.4
0.7	0.85	2.32	0.45	0.825	0.9	3.03	0.6
0.3	0.7	0.272	0.12	0.5	0.825	0.29	0.1
-1.0	0.3	0.093	0.093	-1.0	0.5	0.03	0.03

Θ^* = production angle in the center of mass system

transfers. This assumption is confirmed by recent results of a spark-chamber experiment by Blechschmidt et al. [66].

We have examined the differential angular distribution $dN/d\Delta^2$ of all events in small photon energy intervals and we have compared them to the exponential law. The scanning losses become important only above 2.5 GeV. They reach (2.5 ± 0.5) μb at 3.5 GeV and remain then approximately constant. The corresponding corrections are contained in the calculation of the total cross section for the reactions $\gamma p \rightarrow p\pi^+\pi^-$ and $\gamma p \rightarrow p\rho^o$ (Figs. 13 and 18). In the earlier publications no corrections were made for the scanning losses of events with small proton tracks.

The differential cross section $d\sigma/d\Delta^2$ was fitted with a function $Ae^{-B\Delta^2}$ for $\Delta^2 < 0.5$ (GeV)^2. Table 14 contains the results of the fitting.

Table 14: Fitting of $Ae^{-B\Delta^2}$ to the Differential Cross Section $d\sigma/d\Delta^2$ for $\Delta^2 < 0.5$ (GeV)^2

E_γ [GeV]	A [μb/(GeV)^2]	B (GeV)$^{-2}$
1.4 - 1.8	116.0 ± 15.4	5.98 ± 0.49
1.8 - 2.5	87.8 ± 9.8	4.38 ± 0.39
2.5 - 3.5	116.6 ± 12.4	5.72 ± 0.41
3.5 - 5.8	111.7 ± 11.4	7.29 ± 0.41

The given errors are statistical. The inclination B increases with increasing energy from approximately 5 to 7 GeV^{-2}. The determination of the inclination depends on the resonance form that was used. If one calculates the differential cross section by fitting with a resonance form according to Ross and Stodolsky, one obtains on the average values of B which are larger than 1 GeV^{-2}. The systematic error of the given inclinations is of this order of magnitude.

The differential cross section at 0^o is calculated from $Ae^{-B\Delta^2}_{min}$. Δ^2_{min} is the minimum momentum transfer. At high energies $\Delta^2_{min} \approx (m_\rho^2/2E_\gamma)^2$.

Using the transformation $d\Delta^2 = p_\gamma p_\rho d\Omega/\pi$ one obtains the cross section in the laboratory system.

$d\sigma_{lab}/d\Omega|_{0^o}$ = (0.70 ±0.071) mb/sr for 3.5 GeV < E_γ < 5.8 GeV. This value is in agreement with the value given by Crouch et al. [2c] for the same energy interval, i.e. $d\sigma/d\Omega|_{0^o}$ = $= (0.6 \pm 0.15)\frac{mb}{sr}$. However, there is no agreement with the results given by Lanzerotti et al. [3], i.e. $d\sigma/d\Omega|_{0^o}$ = $= (1.26 \pm 0.17)\frac{mb}{sr}$ at E_γ = 4.4 GeV.

3.2. Discussion of the Cross Sections. The total cross section for ρ-production decreases weakly with increasing photon energy above 1.4 GeV. This behavior can be explained with a dominantly diffractive production process.

Berman and Drell [51] have first suggested a diffraction model for the photoproduction of ρ-mesons. They coupled the ρ-production with the πN-diffraction scattering.

The model gives an approximately-constant ρ-cross section as a function of the photon energy for small momentum transfers.

The curves in Fig. 19 were calculated according to the model suggested by Berman and Drell. For that purpose the parameters of the model were normalized to the experimental total cross section for $\Delta^2 < 0.3$ (GeV)^2 and $E_\gamma > 2.5$ GeV. For the Δ^2-dependency of the πN-scattering, the following was set:

$$d\sigma/d\Delta^2 = \frac{\sigma_{tot}^2}{16\pi} e^{-B\Delta^2}$$

with $$\sigma_{tot} = (24.1 + \frac{26.8 \text{ GeV}}{P_{lab}}) \text{ mb}$$

$$B = 7.7 \text{ (GeV)}^{-2}$$

The differential cross section for $\Delta^2 < 0.5$ (GeV)^2 and $3.5 < E_\gamma < 5.8$ GeV is well represented with this normalization, whereas for smaller energies the experimental points decrease less than the calculated curves.

Despite the qualitative representation of energy- and

Δ^2-dependency of the ρ-cross sections, it is not possible to consistently describe the photoproduction of vector mesons by the model of Berman and Drell. The model is developed under assumptions which hold only for the forward direction. A.S. Krass has shown [6] that the model leads to similar decay angle distributions as the one-pion-exchange model whose predictions are in disagreement with the experiment (for production angles outside the forward direction). Moreover, difficulties appear if one tries to explain the experimental ratio of the ρ^o-, ω- and φ-photoproduction within the frame of the Berman-Drell model [52].

The energy dependency of the ρ-cross section can be compared to the predictions from a combined vector-dominance and quark model [44].

According to the vector-dominance model one has for the cross section of the photoproduction of vector mesons at high energies:

$$\sigma(\gamma p \to Vp) \approx \sum_V \frac{\alpha}{4} \left(\frac{4\pi}{\gamma_V^2}\right) \sigma(Vp \to Vp) \quad .$$

$$(V = \rho^o, \omega, \varphi)$$

The change from $\varphi p \to \rho p$ does not give a contribution in the quark model [53]. It is sufficient to observe the changes from $\omega p \to \rho p$ and $\rho p \to \rho p$.

One can set the following relationship for the differential cross section of the reaction $Vp \to Vp$ ($V = \rho, \omega$)

$$\frac{d\sigma}{dt} = \left.\frac{d\sigma}{dt}\right|_{t=o} \cdot e^{Bt} \quad .$$

One assumes that the elastic Vp-scattering is essentially diffractive. By means of the optical theorem one obtains

$$\sigma_{diff}(Vp \to Vp) = \frac{1}{16\pi B} \sigma_{tot}^2 (Vp) \quad .$$

The summation rule

$$\sigma_{tot}(\rho^o p) = \sigma_{tot}(\omega p) = \frac{1}{2}\left[\sigma_{tot}(\pi^+ p) + \sigma_{tot}(\pi^- p)\right]$$

couples then the cross section for ρ-photoproduction directly to the total π^+p- and π^-p-cross sections.

$$\sigma(\gamma p \to p\rho^o) = \text{const.}\cdot\left[\sigma_{tot}(\pi^+ p) + \sigma_{tot}(\pi^- p)\right]^2 \qquad (18)$$

Table 15 shows the values of $\sigma(\gamma p \to p\rho^o)$ calculated by means of Eq. (18).

Table 15: Comparison of the Energy Dependency of $\sigma(\gamma p \to p\rho^o)$ with a Combined Vector-Dominance/Quark Model

E_γ [GeV]	σ_ρ (exp.) [μb] Breit-Wigner	σ_ρ nach Söding	const.$\cdot\left[\sigma_{tot}(\pi^+ p) + \sigma_{tot}(\pi^- p)\right]^2$ (54)
2.5-3.5	20.5 ± 1.3	19.7 ± 1.3	19.0
3.5-4.5	18.4 ± 1.4	16 ± 1.2	17.0
4.5-5.8	17.1 ± 1.5	15 ± 1.3	15.0

The values calculated according to the vector-dominance and quark model give the energy dependency of the ρ-cross section within the error limits. If one calculates the absolute value for $\sigma(\gamma p \to p\rho^o)$ using $\gamma_\rho^2/4\pi = 0.55$ and $B = 8(\text{GeV})^{-2}$ and neglecting the change $\omega p \to p\rho$, one obtains a value of $\sigma(\gamma p \to p\rho^o) \simeq$ ≃ 16 μb at 5.2 GeV. This value is of the right order of magnitude. In addition to that, the vector-dominance/quark model can predict the proper ratio for the photoproduction of the vector mesons ρ^o, ω and φ [44]. However, the various assumptions and the parameters $\gamma_\rho^2/4\pi$ and B contain still a significant uncertainty.

4. Decay Angle Distributions

4.1. Definitions and Results

The decay angle distributions of a resonance contain information about the spin of the resonance and about the production process. We can use the decay angle distribution to obtain information about the production process since spin and parity of the ρ-meson $J^P = 1^-$ are known.

First, we define useful coordinate systems.

One observes the three-momentum vectors $\vec{\gamma}$, $\vec{p}_i$, $\vec{p}_f$, $\vec{\pi}^+$, $\vec{\pi}^-$ of the photon, the incoming and outgoing proton and the outgoing π-meson in the combined center of mass system. The two vectors $\vec{p}_i$ and $\vec{p}_f$ define the production plane for the reactions $\gamma p \rightarrow p\rho^o$.

Next, one transforms all momenta into the rest system of the $\pi^+\pi^-$ mass combination, i.e. one makes a transformation within the production plane along the flight direction $\vec{p}_f$ by the ρ^o-meson.

We distinguish two cases:

a) Jackson system. The following unit vectors are defined:

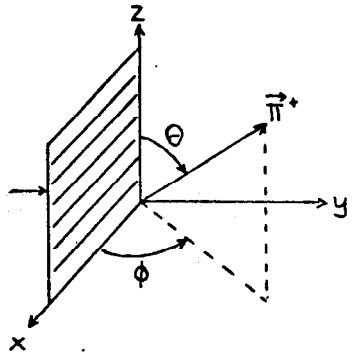

$$\vec{e}_z = \frac{\vec{\gamma}}{|\vec{\gamma}|}$$

photon direction in the rest system of the $\pi\pi$-combination

$$\vec{e}_y = \frac{\vec{p}_i \times \vec{p}_f}{|\vec{p}_i \times \vec{p}_f|}$$

normal to the production plane

$$\vec{e}_x = \vec{e}_y \; \vec{e}_z$$

Θ = polar angle of the resulting π^+-meson (angle between $\vec{\pi}^+$ and e_z)

ϕ = azimuth angle of the resulting π^+-meson (angle between $\vec{e}_x$ and the projection of $\vec{\pi}^+$ in the xy-plane)

The angles Θ and ϕ are called Jackson or OPE angles. They are used if one examines reactions with the one-pion-exchange model.

b. Helicity System. The reference direction is selected differently in the helicity system:

$\vec{e}_z = \frac{-\vec{p}_f}{|\vec{p}_f|}$ ρ-flight direction = direction opposite to the oncoming proton

$\vec{e}_y = \frac{\vec{p}_i \times \vec{p}_f}{|\vec{p}_i \times \vec{p}_f|}$ normal to the production plane

$\vec{e}_x = \vec{e}_y \times \vec{e}_z$

Θ_H = polar angle of the outcoming π^+-meson

ϕ_H = azimuth angle of the outcoming π^+-meson

The angles Θ_H and ϕ_H are called helicity angles. They are useful if one describes the production process in the helicity formalism.

The general decay angle distribution of a $J^P = 1^-$ particle has in both reference frames the following form [55]:

$$W(\cos\Theta,\phi) = \frac{3}{4\pi}\Big[\frac{1}{2}(1-\rho_{0,0}) + \frac{1}{2}(3\rho_{0,0}-1)\cos^2\Theta - \rho_{1,-1}\sin^2\Theta\cos 2\phi - \sqrt{2}\,\mathrm{Re}\rho_{1,0}\sin 2\Theta\cos\phi\Big] \qquad (20)$$

Information about the decay angle distribution is contained in the values $\rho_{0,0}$, $\rho_{1,-1}$, $\mathrm{Re}\rho_{1,0}$ of the spin density matrix.

In order to determine the density matrix element for the ρ-decay one multiplies the distribution (20) and suitable angular distributions for background and N*-events by the terms f of the density distribution in the Dalitz diagram (Eq. (15)). They are then fitted to the experimental distributions by means of the maximum-likelihood method.

Details are described in the Appendix (A.3, A.5).

Figs. 21 and 22 show the density matrix elements $\rho_{0,0}$, $\rho_{1,-1}$, $\mathrm{Re}\rho_{1,0}$ in the Jackson system and also the elements $\rho^H_{0,0}$, $\rho^H_{1,-1}$, and $\mathrm{Re}\rho^H_{1,0}$ in the helicity system for various photon-energy intervals as a function of the production angle. The given errors are statistical. The systematic errors due to the uncertainty in the background treatment are of the order of

the statistical errors.

4.2. Discussion of the Density Matrix Elements.

Thus, after the one-pion-exchange model one expects for the density matrix elements in the Jackson system $\rho_{0,0} = \rho_{1,-1} = \mathrm{Re}\rho_{1,0} = 0$, a $\sin^2\theta$-like distribution of the polar angle and an isotropic distribution of the azimuth angle. The values are only slightly changed by absorption corrections [56]. The data are not compatible with this fact.

Fig. 21 shows curves which result from the "Strong Absorption Model" (SAM) by Eisenberg et al. [57].

Diffractive processes such as the ρ-photoproduction are treated by a spin-independent central potential in the Strong Absorption Model. The four parameters of the model (R_o = radius of the absorbing sphere, ϵ = its transparency, d = blurred edge region, μ = strength of the real part of the potential) are determined simultaneously for various photon energies by fitting of the theoretical curves to the form of the differential reduction cross sections $d\sigma_\rho/d\Omega$. Once the parameters are calculated one obtains knowledge about the decay density matrix without further fitting. The values of the matrix elements are only weakly dependent on the parameters.

The curves shown in Fig. 21 were obtained by Eisenberg et al. from the evaluation of the bubble-chamber experiment of the Cambridge collaboration [2]. They are compatible with the experimental values.

The density matrix elements $\rho^H_{o,o}$ in the helicity system allow a statement about the spin direction of the ρ-meson along its flight direction. The value $\rho^H_{o,o} = 0$ means a complete straightening of the spin along the flight direction (parallel or non-parallel). The experimental points close to the forward direction $\cos\theta^*_\rho > 0.7$ are compatible with zero*), whereas for even

*Such a behavior is also expected within the framework of the vector-dominance model for high energies [58].

higher production angles the spin straightening decreases.

A.S. Krass [6] has recently examined the ρ-production with the interference mechanism suggested by Söding.

Krass used the ρ-amplitude of the Strong Absorption Model since the matrix element M_1 (Eq. (16)) used by Söding for the ρ-production leads to the same decay distributions as the one-pion-exchange model [6]. For the background graphs one uses similar matrix elements as for the diagrams M_2 and M_3 of the Söding calculation. It is thus possible to examine the influence of interference effects on the decay angle distributions. The curves in Fig. 22 show Krass' results for the density matrix elements in the helicity system [6]. The values are calculated at the resonance mass using the parameters* determined by Eisenberg et al. [57]. The dependence of the decay angle distributions on the mass of the ππ-combination is discussed in the next section.

The curves do not agree in all cases with the experimental points. However, due to the sytematic errors one cannot make a final judgment until the density matrix elements are determined with higher accuracy.

5. Interference Effects in the Angular Distributions for Production and Decay

Examination of the effective mass distributions has shown that one can explain the ρ-mass distribution for photon energies above 2 GeV if one introduces an interference of the ρ-amplitude with a coherent background.

The influences of the interference on production and decay of the ρ-meson will be discussed in the following.

Interference effects can be observed well if one plots various distributions as a function of the effective $\pi^+\pi^-$-mass.

Figs. 23 and 24 show the double differential cross section $d\sigma/d\Delta^2 dM\pi\pi$ for four intervals of the mass $M\pi\pi$.

---

*The density matrix elements and the resonance mass do not distinguish themselves from the values which one would obtain from the strong absorption model.

The points contain all ρ- and background events in the corresponding $M_{\pi\pi}$ interval. Only the N* events are subtracted. The cross sections show the characteristic exponential slope. However, the slope of the distributions varies strongly with the $\pi^+\pi^-$-mass. A fit with $Ae^{-B\Delta^2}$ for $\Delta^2 < 0.5\ (GeV)^2$ gives values for the slope B between

$$B = 9.5\ (GeV)^{-2} \text{ at } 0.56 < M_{\pi\pi} < 0.7\ GeV$$

and $$B = 5.4\ (GeV)^{-2} \text{ at } 0.82 < M_{\pi\pi} < 0.96\ GeV.$$

First the differential cross section falls off essentially more steeply for small $\pi^+\pi^-$-masses for which the ρ-mass distribution is increased due to the influence of the interference and the coherent background compared to the cross section averaged over all $\pi^+\pi^-$-masses (see Table 14). The situation is just the reverse for $\pi^+\pi^-$-masses above the resonance mass.

Söding has carried out explicit calculations of the mass dependency on B within the framework of his model [67]. The results agree qualitatively with the experimental values.

Due to the mass dependency of the form of the differential cross section, one expects inversely a variation of the ρ-mass distribution as a function of the production angle.

Fig. 25 shows the $\pi^+\pi^-$-mass distribution for three intervals of the production angle in the center of mass system and for two photon-energy intervals above 2.5 GeV.* The dotted lines at $M_{\pi\pi}$ = 760 MeV were introduced for convenience's sake.

One can see that the shift and deformation of the ρ-mass distribution is largest for small production angles, whereas it decreases for larger production angles.

Krass [6] has calculated values for the mass shift as a function of the production angle using his interference model (see III.4.2). The parameters $\sigma_{\pi^{\pm}N}$ = 30 mb and B_{π} = 8 $(GeV)^{-2}$ enter into the calculations. A nonrelativistic Breit-Wigner form with constant width of 125 MeV and a mass of 765 MeV was used for

---

*Fig. 25 is supported by the total statistics of the experiment which was evaluated in April 1967.

the ρ-mason. The results are summarized together with the experimental values in Table 16.

The experimental average mass values have the same angular dependency as predicted by Krass. However, the observed shifts are larger than one would expect from the calculations.

Table 16: Prediction of the Interference Model of Krass for the Shift of the ρ-Mass Distribution

$\bar{M}$ [MeV] according to Krass			$\bar{M}$ [MeV] Experiment (best estimation from various fits)		
$\cos\Theta_\rho^*$	E_γ=3GeV	E_γ=4.5GeV	$\cos\Theta_\rho^*$	2.5<E_γ<3.5GeV	3.5<E_γ<5.8GeV
0.985	749	747.5	0.96-1.0	732 ± 8	732 ± 8
0.94	753	754.5	0.90-0.96	745 ± 8	748 ± 8
0.866	757	760	0.8 -0.9	764 ± 10	780 ± 15

($\bar{M}$ is the mean mass at half height.)

Figs. 26 and 27 show the decay angle distributions $W(\Theta_H)$ and $W(\phi_H)$ in the helicity system for two $\pi^+\pi^-$-mass intervals as a function of the production angle. The histograms contain all events within the corresponding region of $M\pi^+\pi^-$. However, the N*-portion is separated in the fitting of the theoretical angular distribution (Eq. (20)). The curves in Fig. 27 show the fits normalized to the total number of events. The curves in Fig. 26 are only normalized to the number of the ρ- and background events. The N*-events which are located at $\cos\Theta_H$ = = -1.0 in the helicity system are shaded.

One can see that the density matrix elements are dependent on the $\pi^+\pi^-$-mass.

This behavior is expected due to the interference model of Krass. Table 17 contains the values calculated by Krass for the change of the density matrix elements $\rho^H_{o,o}$ and $\rho^H_{1,-1}$ above

and below the resonance mass.

Table 17: Change of the Density Matrix Elements for $\pi^+\pi^-$-Masses Above and Below the ρ-Mass

Prediction by Krass' Model for E_γ = 4 GeV			Experiment for 2.5 GeV < E_γ < 5.8 GeV		
$\Delta\rho_{m,n} = \rho_{m,n}(M=828) - \rho_{m,n}(M=702)$			$\Delta\rho_{m,n} = \rho_{m,n}(760\text{-}960) - \rho_{m,n}(560\text{-}760)$		
$\cos\Theta_\rho^*$	$\Delta\rho^H_{0,0}$	$\Delta\rho^H_{1,-1}$	$\cos\Theta_\rho^*$	$\Delta\rho^H_{0,0}$	$\Delta\rho^H_{1,-1}$
0.985 (10°)	0.004	-0.001	0.96-1.0	0.053 ± 0.080	-0.057 ± 0.110
0.94 (20°)	0.010	-0.008	0.9 -0.96	-0.026 ± 0.120	-0.001 ± 0.140
0.866 (30°)	0.011	-0.013	0.7 -0.9	0.023 ± 0.150	-0.238 ± 0.180

The experimental results are entered for comparison. However, the errors are too large to allow a conclusion. Yet the observed effects tend to go in the same direction as predicted by Krass.

6. Summary

The photoproduction of ρ-mesons on hydrogen can essentially be explained as a diffractive process.

The absolute magnitude of the total cross section and its energy dependence is quite compatible with the predictions of the vector-dominance model.

The behavior of the ρ-mass distribution above a photon energy of E_γ = 2 GeV and the dependency of the production and decay angle distributions on the $\pi^+\pi^-$-mass show distinct interference effects. These features can be explained qualitatively by the interference of a resonant ρ-amplitude with a coherent background as proposed by Söding.

IV. APPENDIX: FITTING PROCEDURE FOR DETERMINATION OF THE RESONANCE PRODUCTION

1. Introduction

In past years resonance production in bubble-chamber experiments has been generally examined by means of one- or two-dimensional mass and angle distributions. However, for a comprehensive analysis of a final state one has to simultaneously consider the behavior of all independent variables which describe the reaction. This would cause an extensive computational effort and would require experiments with very high numbers of events already for three outcoming particles.

We therefore limit ourselves to fits with three and four variables for final states with three and four outcoming particles respectively. For the fits one generally uses the maximum-likelihood method.

2. Fitting Procedures for the Reaction $\gamma p \rightarrow p\pi^+\pi^-\pi^o$

Let us consider a final state of four particles of known masses $M_1 \ldots M_4$. Let the total energy in the center of mass system be E. If the production process can be described by m Feynman diagrams, then the transition probability is given by

$$W = |A_1 + \ldots + A_m|^2 \qquad (A1)$$

$A_1, \ldots A_m$ are the individual transition amplitudes. In many bubble-chamber experiments one can represent the data sufficiently well if one assumes that the various amplitudes do not interfere with each other.

We make this assumption. Furthermore, we limit ourselves to the simple case for which the m-amplitudes describe the production of m-1 different resonances and of the background. The transition probability is then

$$W = |A_1|^2 + \ldots + |A_m|^2. \qquad (A2)$$

Example: m = 5, photoproduction of the resonances ρ^-, N^{*++} and ρ in a four-particle final state

$$A_1 = A\,(\gamma p \to N^{*+++}\pi^0\pi^-)$$
$$A_2 = A\,(\gamma p \to p\pi^+\rho^-)$$
$$A_3 = A\,(\gamma p \to N^{*+++}\rho^-)$$
$$A_4 = A\,(\gamma p \to p\omega^0)$$
$$A_5 = A\,(\gamma p \to p\pi^+\pi^-\pi^0)$$

The terms $|A_j|^2$ are comprised of a kinematic factor and of the square of the invariant matrix element F_j.

Next, one multiplies W with the density of the possible final states. The differential probability that a reaction leads via a resonance j to a final state, for which the i^{th} particle is in the momentum interval dp_i [59], is given by

$$d^{12}R_4 = \frac{d\vec{p}_1 d\vec{p}_2 d\vec{p}_3 d\vec{p}_4}{2^4 E_1E_2E_3E_4}\,\delta^3(\vec{p}_1+\vec{p}_2+\vec{p}_3+\vec{p}_4)\cdot\delta(E_1+E_2+E_3+E_4-E)\cdot F_j \qquad (A3)$$

$\vec{p}_1 \ldots \vec{p}_4$ three-momenta of the particles in the center of mass system

$E_1 \ldots E_4$ total energy of the particles in the center of mass system

F_j square of the inverse matrix elements

The twelve momentum variables are limited by four conservation theorems. The number of variables is reduced to eight by proper integration. If one now assumes that the F_j are independent of the orientation of the system, then one can eliminate three more variables by further integration. The system is then described by five independent variables.

The following five effective masses M_{12}^2, M_{34}^2, M_{14}^2, M_{124}^2 and M_{134}^2 are chosen as variables.

All other effective masses can be expressed by means of those five. The effective mass $M_{1\ldots k}$ is given by

$$M_{1..k}^2 = (p_1 + p_2 + \ldots + p_k)^2$$

$p_1 \ldots p_k$ = four-momenta of the k particles.

The probability that the five effective masses M_{12}^2, ... M_{134}^2 are within the interval $dM_{12}^2 \ldots dM_{134}^2$ for a reaction is given by

$$d^5R_4 = \frac{\pi^2}{8E^2}\frac{1}{B^{1/2}}\, dM_{12}^2 dM_{34}^2 dM_{14}^2 dM_{124}^2 dM_{134}^2 \cdot F_j \qquad (A4)$$

The expression B is given by Eq. (7) in [59].

Except for the factor F_j, d^5R_4 gives the distribution of the effective masses caused by conservation of momentum and energy. This distribution is also called phase space.

If one assumes further that the squares of the matrix elements F_j are independent of the masses M_{14} and M_{134}, then the differential probability is simplified by two integrations over M_{14}^2 and M_{134}^2.

$$d^3R_4 = \frac{\pi^3}{8E^2M_{12}^2}\sqrt{\left[M_{12}^2-(M_1+M_2)^2\right]\left[M_{12}^2-(M_1-M_2)^2\right]}\, dM_{12}^2 dM_{34}^2 \cdot dM_{124}^2 \cdot F_j \qquad (A5)$$

If no further information is available about the production process, then one can describe the effective mass distribution of a two-particle resonance according to Jackson [44] by multiplying the n-particle phase space (n = number of particles in the final state, n = 4) by

$$F(M_{ij}) = C\,\frac{M_{ij}}{q_{ij}(M_{ij})}\left[\frac{\Gamma(M_{ij})}{(M_{ij}^2-M_{ij}^{o2})^2 + M_{ij}^{o2}\Gamma^2(M_{ij})}\right] \qquad (A6)$$

where C is a constant

M_{ij}^o is the resonance mass

$\Gamma(M_{iu})$ is an energy-dependent width of the resonance

q_{ij} is the size of the three-momentum of the particles i or j in their common rest system

$$q_{ij}(M_{ij}) = \frac{\sqrt{\left[M_{ij}^2-(M_i+M_j)^2\right]\left[M_{ij}^2-(M_i-M_j)^2\right]}}{2M_{ij}}$$

$F(M_{ij})$ is essentially a relativistic Breit-Wigner expression.

In the final state $p\pi^+\pi^-\pi^o$ one observes most frequently the resonances ω^o, N^{*++} and ρ^-.

We set

$$M_1 = M_{\pi^-} \qquad M_{12} = M(\pi^-\pi^o)$$
$$M_2 = M_{\pi^o} \qquad M_{34} = M(p\pi^+)$$
$$M_3 = M_p \qquad M_{124} = M(\pi^-\pi^o\pi^+)\,.$$
$$M_4 = M_{\pi^+}$$

The production of the resonances ρ^- and N^{*++} is according to Eq. (A6) described by the expression $F^{\rho}(M_{12})$ and $F^{N^*}(M_{34})$.

We use the following widths [47]:

$$\Gamma(M_{12}) = \Gamma_\rho \frac{q_{12}^3(M_{12})}{q_{12}^3(M_{12}^o)} \cdot \frac{M_{12}^o}{M_{12}}\,, \tag{A7}$$

$$\Gamma(M_{34}) = \Gamma_{N^*} \frac{q_{34}^3(M_{34})}{q_{34}^3(M_{34}^o)} \left[\frac{(M_{34}+M_3)^2 - M_4^2}{M_{34}^2}\right]\left[\frac{M_{34}^{o2}}{(M_{34}^o+M_3)^2 - M_4^2}\right]$$

Γ_ρ = width of the ρ^-

Γ_{N^*} = width of the N^*

The ω-production is described by a Gaussian function since the width of the ω-meson is smaller than the experimental mass resolution Γ.

$$F(M_{124}) = \frac{1}{2\sqrt{2\pi}\Gamma M_{124}} \cdot e^{-\frac{(M_{124}-M_{124}^o)^2}{2\Gamma^2}} \tag{A8}$$

$$\sum_{i=1}^{n} \ln \rho^i$$

$F_j = 1$ for uncorrelated background events.

Before we form the combined probability for production of resonances we normalize the expression d^3R_4 to 1.

$$d^3R_4' = \frac{\frac{q_{12}}{E^2 M_{12}}\, dM_{12}^2\, dM_{34}^2\, dM_{124}^2\, F_j}{N_j} \tag{A9}$$

$$Nj = \int \frac{q_{12}}{E^2 M_{12}} dM_{12}^2 dM_{34}^2 dM_{124}^2 \cdot Fj$$

Next we introduce the frequency of the individual resonances:

A_1 = frequency of the reaction $\gamma p \rightarrow N^{*++}\pi^-\pi^o$
A_2 = frequency of the reaction $\gamma p \rightarrow p\pi^+\rho^-$
A_3 = frequency of the reaction $\gamma p \rightarrow p\omega^o$
A_4 = frequency of the reaction $\gamma p \rightarrow N^{*++}\rho^-$
$(1-A_1-A_2-A_3-A_4)$ = frequency of the reaction $\gamma p \rightarrow p\pi^+\pi^-\pi^o$

Then, the total probability that a reaction will lead to the five treated states, where the invariant masses M_{12}^2, M_{34}^2, M_{124}^2 are in the interval dm_{12}^2, dM_{34}^2, dM_{124}^2 is:

$$dW = \left[A_1 \cdot \frac{F^{N^*}(M_{34})}{N_1} + A_2 \frac{F^{\rho}(M_{12})}{N_2} + A_3 \frac{F^{\omega}(M_{124})}{N_3} + A_4 \frac{F^{\rho}(M_{12}) F^{N^*}(M_{34})}{N_4} + (1-A_1-A_2-A_3-A_4) \frac{1}{N_5} \right] \frac{q_{12}}{E^2 M_{12}} dM_{12}^2 dM_{34}^2 dM_{124}^2 \qquad (A10)$$

One must average over finite intervals of the photon energy E_γ since the events are produced by a continuous bremsspectrum.

One multiplies the various expressions F_j with an energy-dependent frequency distribution $h(E_\gamma)$ of the experimentally-found events of the type $\gamma p \rightarrow p\pi^+\pi^-\pi^o$;

$$dW' = \left[A_1 \frac{F(M_{34})}{N_1'} + A_2 \frac{F(M_{12})}{N_2'} + A_3 \frac{F(M_{124})}{N_3'} + A_4 \frac{F(M_{12}) \cdot F(M_{34})}{N_4'} + \frac{(1-A_1-A_2-A_3-A_4)}{N_5'} \right] h(E_\gamma) \frac{q_{12}}{E^2 M_{12}} dM_{12}^2 dM_{34}^2 dM_{124}^2 dE_\gamma \qquad (A11)$$

$$Nj' = \int F_j \, h(E_\gamma) \frac{q_{12}}{E^2 M_{12}} dM_{12}^2 dM_{34}^2 dM_{124}^2 dE_\gamma$$

$h(E_\gamma)$ = energy distribution of the events $\gamma p \rightarrow \pi^+\pi^- n$
E_γ = laboratory energy of the photon

i.e. one adds E_γ to the number of variables.

One assumes for this energy averaging that all terms of the sum have the same energy dependence. A more accurate mean of the energies can be obtained by an iteration if one determines the energy dependence of the individual terms of the sum by fitting in various photon-energy intervals.

The integration over each one of the mass variables can be carried out analytically. The integration limits were given by Nyborg et al. [59]. The remaining integrations are carried out numerically. The frequencies $A_1 \ldots A_5$ are determined in the SUPFIT program by means of the maximum-likelihood method by fitting of dW' to the distribution of the experimental events.

The differential probability dW'^i for each measured event with the effective masses M_{12}^i, M_{34}^i, M_{124}^i and the photon energy E_γ^i, is

$$dW'^i = dW' \left(M_{12}^i, M_{34}^i, M_{124}^i, E_\gamma^i\right)$$

The probability for n measured events is

$$L = \prod_{i=1}^{n} \frac{dW'^i}{dM_{12}^2\, dM_{34}^2\, dM_{124}^2\, dE_\gamma} = \prod_{i=1}^{n} \sum_{j=1}^{5} \left(A_j \frac{F_j^i}{N_j} \cdot \rho^i\right) \qquad \text{(A12)}$$

$$\text{where} \quad \rho^i = \frac{h(E_\gamma^i) q_{12}^i}{E^{i2} M_{12}^{i2}} .$$

The optimum values of the parameters are determined by maximizing the logarithm of L. L is called likelihood function.

$$\ln L = \sum_{i=1}^{n} \ln \sum_{j=1}^{5} \left(A_j \frac{F_j^i}{N_j} \rho^i\right) \qquad \text{(A13)}$$

$$= \sum_{i=1}^{n} \ln \sum_{j=1}^{5} A_j \frac{F_j^i}{N_j} + \sum_{i=1}^{n} \ln \rho^i$$

The expression is a constant for a given experiment and can be omitted.

The quality of the fit depends on how accurate the experimental conditions are represented by the theoretical

probability distribution for resonance and background events.

In the case of the reaction $\gamma p \rightarrow p\pi^+\pi^-\pi^o$ the fitting is made more difficult by the experimental addition of wrongly-interpreted reactions with several neutral particles. However, as Crouch et al. [2e] have shown with Monte Carlo calculations, these events have only slightly-shifted phase space distributions if they are interpreted in the kinematic program as hypotheses $\gamma p \rightarrow p\pi^+\pi^-\pi^o$.

The fitting procedure can be extended to arbitrary two- and three-particle resonances [60]. One starts with Eq. (A4) and substitutes the masses of interest instead of the five masses which are used as independent variables. One obtains for each resonance an additive term in the likelihood function.

3. Fitting Procedure for the Reaction $\gamma p \rightarrow p\pi^+\pi^-$

Several resonances are produced in the reaction $\gamma p \rightarrow p\pi^+\pi^-$.

One proceeds as in the previous section and assumes that the different possible transition amplitudes do not interfere.

The probability that a reaction will lead over a resonance j to a final state, in which the i^{th} particle is within the momentum interval $d\vec{p}_i$, is

$$d^9R_3 = \frac{d\vec{p}_1 d\vec{p}_2 d\vec{p}_3}{2^3 E_1 E_2 E_3}\,\delta^3(\vec{p}_1+\vec{p}_2+\vec{p}_3)\,\delta(E_1+E_2+E_3-E)\cdot F_j \qquad \text{(A14)}$$

F_j = square of the invariant matrix element

The nine momentum variables are limited by four conservation theorems. The reaction is determined by five independent variables. After integration over two angles and after fixing of the total energy E, the number of independent variables is reduced to two. One chooses as variables the two effective masses M_{13}^2 and M_{23}^2.

The probability distribution is then [61, 62]:

$$d^2R_3 = \frac{\pi^2}{4E^2}\,dM_{13}^2\,dM_{23}^2\,F_j \quad . \qquad \text{(A15)}$$

A distribution M_{13}^2 versus M_{23}^2 is called Dalitz diagram. Phase space events with equal total energy are equally distributed in the Dalitz diagram.

The resonances N^{*++}, ρ^o and f^o are mainly produced in the reaction $\gamma p \rightarrow p\pi^+\pi^-$. The contribution of the f^o-meson can be neglected in many fits since it appears only weakly.

We make the following assignment:

$$\begin{aligned} M_1 &= M_p & M_{13} &= M(p\pi^+) \\ M_2 &= M_{\pi^-} & M_{23} &= M(\pi^-\pi^+) \\ M_3 &= M_{\pi^+} & M_{12} &= M(p\pi^-) \end{aligned} \quad .$$

For the squares of the invariant matrix elements $F(M_{13})$, $F(M_{23})$ one uses again the relativistic Breit-Wigner expressions (Eq. (A6)) given by Jackson [47].

The empirically-obtained widths proposed by Jackson are introduced instead of the widths given in Eq. (A7). The latter are based on perturbation calculations. The widths obtained for the perturbation calculation distinguish themselves only slightly from the empirical widths.

$$N^{*++}: \quad \Gamma(M_{13}) = \Gamma_{N^*} \frac{q_{13}^3(M_{13})}{q_{13}^3(M_{13}^o)} \frac{(2.2M_\pi^2 + q_{13}^2(M_{13}^o))}{(2.2M_\pi^2 + q_{13}^2(M_{13}))} \qquad (A16)$$

$$\rho^o: \quad \Gamma(M_{23}) = \Gamma_\rho \frac{q_{23}^3(M_{23})}{q_{23}^3(M_{23}^o)} \frac{2q_{23}^2(M_{23}^o)}{q_{23}^2(M_{23}^o) + q_{23}^2(M_{23})}$$

$$f^o: \quad \Gamma(M_{23}) = \Gamma_f \frac{q_{23}^5(M_{23})}{q_{23}^5(M_{23}^o)}$$

Let N_j be the normalization integral.

$$Nj = \int Fj \frac{\pi^2}{4E^2} dM_{13}^2 dM_{23}^2$$

We now introduce the following frequencies:

A_1 = frequency of the reaction $\gamma p \rightarrow p\pi^+\pi^-$ (background)

A_2 = frequency of the reaction $\gamma p \rightarrow N^{*++}\pi^-$

A_3 = frequency of the reaction $\gamma p \rightarrow p\rho^o$

A_4 = frequency of the reaction $\gamma p \rightarrow pf^o$

with the secondary condition $A_1 + A_2 + A_3 + A_4 = 1$.

Then the probability that the four observed states are reduced in a reaction, where the effective masses M_{13}^2 and M_{23}^2 are in the interval dM_{13}^2 and dM_{23}^2, is:

$$dW = \left[A_1 \frac{1}{N_1} + A_2 \frac{F^{N^*}(M_{13})}{N_2} + A_3 \frac{F^{\rho}(M_{23})}{N_3} + A_4 \frac{F^{f}(M_{23})}{N_4} \right] \frac{\pi^2}{4E^2} dM_{13}^2 dM_{23}^2 \quad (A17)$$

The decay angle distribution of the ρ^o-meson is taken into consideration in the fit of the channel $\gamma p \rightarrow p\pi^+\pi^-$. The first results of this experiment [4c] have shown that the ρ^o-meson has a characteristic decay angle distribution with respect to its flight direction. The distribution goes approximately as $\sin^2\Theta_H$. The helicity angle Θ_H is the angle between the outcoming π^+-meson and the opposite direction of the outcoming proton in the rest system of the two π-mesons.

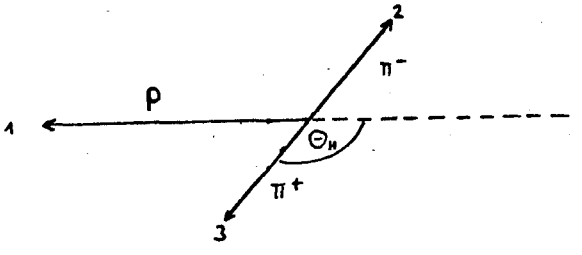

The cosine of the helicity angle can be expressed by M_{13}, M_{23} and the total energy E in the center of mass system of the three particles:

$$\cos\Theta_H = \frac{Mp^2 + M\pi^2 + 2E_1' \sqrt{q_{23}^{2} + M\pi^{2}} - M_{13}^2}{2\sqrt{E_1'^2 - Mp^2}\, q_{23}} \quad (A18)$$

with

$$E_1' = \frac{E^2 - Mp^2 - M_{23}^2}{2M_{23}}$$

$$q_{23} = \frac{\sqrt{\left[M_{23}^2 - (M_2+M_3)^2\right]\left[M_{23}^2 - (M_2-M_3)^2\right]}}{2M_{23}}$$

An angular distribution

$$W(\cos\Theta_H) = 1.5 \cdot (1-A_5 + (3A_5-1)\cos^2\Theta_H)$$

is multiplied by the matrix elements $F^{\rho}(M_{23})$.

The fit in the $p\pi^+$-mass distribution can be improved by this procedure. Fig. 28 shows the experimental mass distributions $M_{p\pi^+}$ in the photon-energy interval 1.8 GeV $< E_\gamma <$ 2.5 GeV with two fits: a) isotropic ρ^o-decay, b) ρ^o-decay proportional to $\sin^2\Theta_H$.

The fits to the experimental distributions were carried out with the RESGAM and MITOSIS computer programs. The two programs are treated separately as follows.

4. Fits with RESGAM

Among others, the RESGAM and MITOSIS programs distinguish themselves by the type of energy averaging. In the RESGAM program [63] the squares of the matrix elements F_j are multiplied by the energy-dependent frequency distribution $h(E_\gamma)$ of the experimentally-found events of the type $\gamma p \rightarrow p\pi^+\pi^-$ and they are then normalized.

This averaging makes sense for small photon-energy intervals and for intervals in which the various in-between states have a similar energy dependence.

The probability distribution is then:

$$dW' = \left[A_1 \frac{1}{N_1'} + A_2 \frac{F^{N^*}(M_{13})}{N_2'} + A_3 \frac{F^{\rho}(M_{23})}{N_3'} \cdot W(\cos\Theta_H) + A_4 \frac{F^{f}(M_{23})}{N_4'} \right] \quad (A19)$$

$$\cdot h(E_\gamma) \frac{\pi^2}{4E^2} dM_{13}^2 dM_{23}^2 dE_\gamma$$

$$N_j' = \int F_j h(E_\gamma) \frac{\pi^2}{4E^2} dM_{13}^2 dM_{23}^2 dE_\gamma$$

In the RESGAM program the parameters are determined by the method of least squares by successive fits to one-dimensional distributions of the experimental effective masses M_{13}, M_{23}, and M_{12}. One obtains the theoretical distributions dW'/dM_{13} and dW'/dM_{23} by integration over the other variables. The distribution dW'/dM_{12} can be obtained if one substitutes M_{12} for one or both variables M_{13} and M_{23}.

In order to determine differential cross sections, the data are read in in steps of the production angle Θ^* or the square of the four-momentum transfers Δ^2 and then separately fitted in the intervals. The kinematic limits for Δ^2 are taken into consideration.

The advantage of RESGAM is in its relatively high computation speed. It is due to the fact that only one-dimensional distributions are fitted. For a case where there are no limitations in Δ^2 the RESGAM program needs 0.5-3 min on the IBM 7044 for fitting with three variables. Thus, RESGAM is especially suitable for fitting masses and widths of resonances.

Changes in the theoretical probability distribution require a larger progamming effort than in the MITOSIS program.

5. Fits with MITOSIS

MITOSIS carries out a complete maximum-likelihood analysis [64].

The energy averaging is set up differently than in RESGAM. One takes into consideration that the energy-dependent frequency

distribution is proportional to the photon spectrum $N_\gamma(E_\gamma)$ and to the cross section. The cross section for N^{*++} and background events is proportional to $1/E_\gamma$ above the threshold. On the other hand, the cross section for ρ-production decreases only weakly above the threshold. The energy dependence of the f^o-production is not yet well known. Therefore, the following weighting is chosen:

for N^{*++}, f^o and background: frequency distribution $\sim \frac{N_\gamma(E_\gamma)}{E_\gamma}$

for ρ^o: frequency distribution $\sim \frac{N_\gamma(E_\gamma)}{E_\gamma} E_\gamma^{\,n}$

$$n = 0.74 \text{ (determined experimentally).}$$

The dependence of the squares of the matrix elements on the production angle can be introduced in the MITOSIS program by a factor $e^{-B\Delta^2}$. However, one obtains better fits for simultaneous determination of N^* and ρ^o-production if one sets the factors $B = 0$.

The probability distribution is then written as:

$$dW' = \left(A_1 \frac{1}{N_1'} + A_2 \frac{F^{N^*}(M_{13})}{N_2'} + A_3 \frac{F^{\rho}(M_{23}) \cdot W(\cos\Theta_H)}{N_3'} \cdot E_\gamma^{\,n} + A_4 \frac{F^{f}(M_{23})}{N_4'}\right) \cdot \frac{N_\gamma(E_\gamma)}{E_\gamma} \frac{\pi^2}{4E^2} \, dM_{13}^{\,2} \, dM_{23}^{\,2} \, dE_\gamma \qquad \text{(A20)}$$

with N_j' = normalization integral; or

$$dW' = \sum_{j=1}^{4} A_j \frac{F_j'}{N_j'} \cdot \rho \; dM_{13}^{\,2} \, dM_{23}^{\,2} \, dE_\gamma$$

with

$$\rho = \frac{N_\gamma(E_\gamma)}{E_\gamma} \frac{\pi^2}{4E^2} \; .$$

For n events with the measured values $M_{13}^{\,i}$, $M_{23}^{\,i}$, $\cos\Theta_H^{\,i}$ and $E_\gamma^{\,i}$ one obtains for the probability:

$$L = \prod_{i=1}^{n} \frac{dW^{i'}}{dM_{13}^{\,2} \, dM_{23}^{\,2} \, dE_\gamma} = \prod_{i=1}^{n} \sum_{j=1}^{4} A_j \frac{F_j^{\,i'}}{N_j'} \rho^{\,i} \; . \qquad \text{(A21)}$$

Then,

$$\ln L = \sum_{i=1}^{n} \ln \sum_{j=1}^{4} A_j \frac{F_j^{i'}}{N_j} \rho^i = \sum_{i=1}^{n} \ln \sum_{j=1}^{4} A_j \frac{F_j^{i'}}{N_j} + \sum_{i=1}^{n} \ln \rho^i .$$

The factor $\sum_{i=1}^{n} \ln\rho^i$ can again be omitted. One applies the expanded maximum-likelihood method [64]. One calculates with event numbers A_j instead of normalized frequencies. The expression

$$-\ln L = -\sum_{i=1}^{n} \ln \sum_{j=1}^{4} A_j \frac{F_j^{i'}}{N_j} + A_1 + A_2 + A_3 + A_4 \cdot \qquad (A22)$$

is minimized.

In order to determine the differential cross sections, the data are read in and fitted in intervals of $\cos\Theta^*$ or Δ^2.

In the MITOSIS program it is possible to simultaneously fit the spin-density matrix elements of the ρ^o-mesons.

The angular distributions $W(\Theta, \phi)$ for the ρ^o-decay and suitable angular distributions $W'(\Theta, \phi)$ for the background events are multiplied by the matrix elements. One has for the ρ^o-meson [55]

$$W(\Theta,\phi) = \frac{3}{4\pi} \left(\frac{1}{2}(1-A_5) \sin^2\Theta + A_5\cos^2\Theta - A_6\sin^2\Theta\cos2\phi - \sqrt{2}\, A_7 \sin2\Theta\cos\phi\right).$$

A distribution with asymmetric contributions in $\cos\Theta$ is chosen for the background.

$$W'(\Theta,\phi) = \frac{3}{4\pi}\left[\frac{1}{2}(1-A_8) \sin^2\Theta + A_8\cos^2\Theta - A_9\sin^2\Theta\cos2\phi - \sqrt{2}A_{10}\sin2\Theta\cos\phi\right] + \frac{\sqrt{3}}{4\pi} 2A_{11}\cos\Theta$$

with

$A_5 = \rho_{0,0}$
$A_6 = \rho_{1,-1}$
$A_7 = \mathrm{Re}\rho_{1,0}$

density matrix elements of ρ^o-meson

$$
\left.
\begin{aligned}
A_8 &= \rho_{0,\rho} \\
A_9 &= \rho_{1,-1} \\
A_{10} &= \mathrm{Re}\,\rho_{1,0}^{\mathrm{int}} \\
A_{11} &= \mathrm{Re}\,\rho_{0,0}
\end{aligned}
\right)
$$

Density matrix elements for the phenomenolistic description of the background

Θ = Jackson angle. The Jackson angle is the angle between the outcoming π^+-meson and the direction of the incoming photon in the rest system of the two π-mesons

ϕ = the corresponding azimuth angle

Θ_H = the helicity angle

ϕ_H = the corresponding azimuth angle.

The angular distribution of the background $W'(\Theta, \phi)$ is multiplied by the matrix element for f^o, N^{*++} and background events.

On the other hand, the distribution $W'(\Theta_H, \phi_H)$ is multiplied only by the matrix elements for background and f^o-production since the helicity angle for events with N^{*++}-production is already clearly fixed by Eq. (A18)and does not have to be fitted anymore. (The N*-matrix element is then multiplied only by an angular distribution $W'(\phi_H)$).

In order to fit the spin-density matrix elements, the frequencies $A_1 \ldots A_4$ from the previous calculation are introduced fixed. The fitting of seven parameters for a statistic of 250 events takes approximately 15-25 min computation time on the IBM 7044.

A subprogram prints out the experimental and fitted angular and mass distributions in the form of a histogram and a curve respectively, after each fitting. In this manner one obtains immediately a control for the quality of the fit.

ACKNOWLEDGMENTS

This report was accomplished within the framework of an experiment of the Aachen-Berlin-Bonn-Hamburg-Heidelberg-Munich Collaboration on the German electron synchrotron in Hamburg.

I would like to thank Prof. M. W. Teucher who generously supported this work. Through his never-tiring efforts Dr. E. Lohrmann provided the decisive drive. I would like to thank him for his continuous willingness to provide helpful criticism.

I would further like to thank the members of the Hamburg Bubble Chamber Group, especially D. Lüke, H. Meyer, Dr. P. Söding, Dr. W.P. Swanson, Dr. G. Wolf and all the diploma candidates of the gamma experiment for their willing cooperation and for the many useful discussions.

The Bubble Chamber Operations Group, the co-workers of the synchrotron, the plant services and the computer center and the scanners have significantly contributed to the success of the experiment through their reliable workmanship.

I would like to express my thanks to the physicists of the Groups in Aachen, Berlin, Bonn, Heidelberg and Munich for their fruitful cooperation and the opportunity to make use of their results.

I am indebted to Prof. A.S. Krass for the contribution of several as-yet-unpublished results.

This work was supported by the Federal Ministry for Scientific Research.

V. LITERATURE

(1) D. McLeod, S. Richert, A. Silverman, Phys. Rev. Letters 7, 383 (1961)

(2) Cambridge Bubble Chamber Group, H.R. Crouch et al.

a) Phys. Rev. Letters 13, 636 and 640 (1964)

b) Proc. Int. Symp. El. Photon Int., Hamburg (1965), Vol. II

c) Phys. Rev. 146, 994 (1966) (ρ-production)

d) Phys. Rev. 155, 1477 (1967) (total cross sections)

e) Phys. Rev. 155, 1468 (1967) (ω- production

f) Phys. Rev. 156, 1426 (1967) (Prod. Strange Particles)

g) Phys. Rev. (in print) (N^*-production)

(3) L.J. Lanzerotti, R.B. Blumenthal, D.C. Ehn, W.L. Faissler, P.M. Joseph, F.M. Pipkin, J.K. Randolph, J.J. Russel, D.G. Stairs, J. Tennenbaum, Phys. Rev. Letters 15, 210 (1965)

(4) Aachen-Berlin-Bonn-Hamburg-Heidelberg-Munich Collaboration:
U. Brall, R. Erbe, H.G. Hilpert, G. Reimann, E. Schüttler, H. Böttcher, W. Bothin, K. Lanius, A. Meyer, A. Pose, J. Schreiber, K. Böckmann, W. Johnssen, J. Moebes, H. Mück, B. Nellen, W. Tejessy, D. Cords, G. Knies, G. Harigel, G. Horlitz, E. Lohrmann, H. Meyer, W.P. Swanson, M.W. Teucher, G. Wolf, S. Wolff, D. Lüke, D. Mönkemeyer, D. Pollmann, W. Rau, E. Raubold, P. Söding, H. Spitzer, W. Woidtke, H. Beisel, E. Burkhardt, H. Filthuth, H. Kolar, P. Steffen, P. Freund, K. Gottstein, N. Schmitz, P. Seyboth, J. Seyerlein;
Progress Reports were published in:

a) Proc. Int. Symp. Electron Photon Int., Hamburg 1965, Vol. II

b) Nuovo Cim. 41, 270 (1966) (survey)

c) DESY Bericht 66/32 (1966) (survey)

d) Nuovo Cim. 46A, 795 (1966) (ω, ϕ, η, X^0-production)

e) Phys. Letters 23, 707 (1966) (N^{*++}-production)

f) Nuovo Cim. 48A, 262 (1967) (ρ--production)

g) Nuclear Phys. B1, 668 (1967) (momentum and angular distributions in the laboratory system)

h) DESY Bericht 67/6, (1967) (Prod. Strange Particles)
and Nuovo Cim. 49, 504 (1967)

(5) P. Söding, Phys. Letters 19, 702 (1965)

(6) A.S. Krass, "Interference Effects in Photoproduction of ρ-Mesons", Phys. Rev. 159, 1496 (1967)
and private communications.

(7) H. Meyer, H. Spitzer, Internal Report DESY F1-1 (1966)

(8) G. Lutz, Private Commun., G. Lutz, H.D. Schulz, DESY Report 7/29 (1967)
(9) L'Onde Électrique 41, 1001 (Dec. 1961)
(10) ZEISS Informationen 59, 15 (1966)
(11) G. Wolf, Internal Report, DESY F1-3 (1966)
(12) F. Storim, G. Wolf, INDEX Program, Internal Report BLA-KA A, Hamburg, 1967, F. Storim, Thesis, Hamburg, 1967
(13) D. Cords, Thesis, Hamburg, 1964; G. Knies, Thesis, ,Hamburg,1964
(14) S. Wolff, Thesis, Hamburg, 1965
(15) G. Wolf, WELAGA Program Description, Hamburg, 1963
(16) G. Wolf, Dissertation, Hamburg, 1964
(17) G. Wolf, "On the Optical System of the Bubble Chamber at DESY," Internal Report, Hamburg, 1964
(18) R. Böck, CERN 60-30 (1960), CERN 61-29 (1961), GRIND Manual, DD/EXP/62/10, CERN (1963)
(19) D. Mönkemeyer, Thesis, Hamburg 1967
(20) G.R. Lynch, UCRL 10335 (1962)
(21) E. Raubold, FAKE Manual, Hamburg (1966). The Hamburg FAKE version was changed such that the error treatment corresponds to the error treatment in the WELAGA geometry program.
(22) W. Tejessy, Private Communications
(23) H. Butenschön, CUT 1-CUT 2-CUT 3, Internal Report, BLAKA C Hamburg (1966)
(24) V. Blobel, H. Butenschön, P.v. Handel, P. Schilling, ULTRAN Description, Internal Report, Hamburg (1964)
H. Butenschön, DESY Report, 66/29 (1966)
(25) A.H. Rosenfeld, A. Barbaro-Galtieri, W.J. Podolsky, L.R. Price, M. Roos, P. Söding, W.J. Willis, C.G. Wohl, Rev. Mod. Phys. 39, 1 (1967)
(26) J.A. Wheeler, W.E. Lamb jr., Phys. Rev. 55, 858 (1939), Phys. Rev. 101, 1836 (1956)
(27) B. Rossi, High Energy Particles, New York 1952
(28) D.C. Gates, Berkeley UCRL 9390 (1960)
D.C. Gates, R.W. Kenney, W.P. Swanson, Phys. Rev. 125, 1310 (1962)
(29) E. Malamud, Phys. Rev.115, 687 (1959)
(30) P.M.Morse, L.A.Young, E.S.Haurwitz, Phys. Rev. 48, 948 (1935)
(31) A. Sørenssen, Nuovo Cim. 38, 745 (1965), Nuovo Cim. 41, 543 (1966)
(32) D. Bernstein,W.K.H.Panofsky, Phys. Rev. 102, 522 (1956)
(33) K. Mork, H. Olsen, Phys. Rev. 140, B1661 (1965)
(34) H.D. Schulz, DESY Report, 66/16 (1966)
(35) H.D. Schulz, private communications, Hamburg, 1967

(36) K.S. Suh, H.A. Bethe, Phys. Rev. 115, 672 (1959)

(37) V. Votruba, Phys. Rev. 72, 1468 (1948)
and Bull. Intern. acad. Tcheque Sci. 49, 19 (1948)

(38) J. Joseph, F. Rohrlich, Rev. Mod. Phys. 30, 354 (1958)

(39) G. Kessler, Private Communications, Hamburg, 1967

(40) Below 1.5 GeV: J.T. Beale, S.D. Ecklund, R.L. Walker, CALT-68-108 (1966)

Above 1.5 GeV:

a) $\gamma p \to p\pi^0$ M. Braunschweig, D. Husmann, K. Lübelsmeyer, D. Schmitz, Phys. Letters 22, 705 (1966), G.C. Bolon et al, Phys. Rev. Letters 18, 926 (1967)

b) $\gamma p \to n\pi^+$ V.B. Elings et al, Phys. Rev. Letters 16, 474 (1966), G. Buschhorn et al. Phys. Rev. Letters 17, 1027 (1966), Phys. Rev. Letters 18, 571 (1967)

(41) D. Lüke, Thesis, Hamburg, 1966

(42) M.G. Hauser, CALT-68-123 (1967) and Phys. Rev. 160, 1215 (1967)

(43) J.V. Allaby, H.L. Lynch, D.M. Ritson, Phys. Rev. 142, 887 (1966)

(44) H. Joos, Phys. Letters, 24B, 103 (1967); H. Joos, DESY Report 67/13 (1967) and literature quoted in that report.

(45) J. Shapiro, Suppl. Nuovo Cim. 18, 40 (1960)

(46) H. Satz, Phys. Letters 25 B, 27 (1967)

(47) J.D. Jackson, Nuovo Cim. 34, 1644 (1964)

(48) M. Ferro-Luzzi et al, Nuovo Cim. 39, 417 (1965)

(49) L.D. Jacobs, UCRL 16877 (1966)

(50) M. Ross, L. Stodolsky, Phys. Rev. 149, 1172 (1966)

(51) S.M. Berman, S.D. Drell, Phys. Rev. 133, B 791 (1964)

(52) H. Harari, Phys. Rev. 155, 1565 (1967)

(53) K. Kajantie, J.S. Trefil, Phys. Letters 24B, 106 (1967)

(54) A. Citron et al, Phys. Rev. 144, 1101 (1966)

(55) K. Gottfried, J.D. Jackson, Nuovo Cim. 33, 309 (1964)

(56) G. Kramer, K. Schilling, Z. Physik 191, 51 (1966) and private communications

(57) Y. Eisenberg, E.E. Ronat, A. Brandstetter, A. Levy, E. Gotsman, Phys. Letters 22, 217 and 223 (1966)

(58) D. Schildknecht, private Communications, Hamburg, 1967

(59) P. Nyborg et al, Phys. Rev. 140, B 914 (1965)

(60) P. Söding, Informal Description of the SUPFIT Program, Hamburg, 1966

(61) R. Hagedorn, Relativistic Kinematics, Benjamin Inc., New York, 1963, S.98

(62) O. Skjeggestad, CERN 64-13, Vol. II

(63) The RESGAM Program was developed by A. Meyer.

(64) W.P. Swanson, DESY Report 66/17, 1966

(65) J.G. Asbury et al, Phys. Rev. Letters in print.
S.C.C. Ting, Lecture given at the International School of Physics "Ettore Majorana", Erice 1967
and U. Becker, Private Communications, Hamburg, 1967

(66) H. Blechschmidt et al, DESY Internal Report, F32-2 (1967)

(67) P. Söding, private communications, 1967

VI. TABLE OF ILLUSTRATIONS

Fig. 1. Beam set-up.

Fig. 2. Particle-trajectory envelopes.
(Definition of the reference system, see Fig. 3).
Multiple scattering of the electrons in the target T2 was neglected in the calculation of the envelopes shown. The photon trajectories were assumed in the direction of the electron trajectories through target T2.

Fig. 3. Schematic layout of the bubble chamber.
a. Chamber body with side windows and cameras.
b. Construction elements of the bubble chamber.

Fig. 4. Spatial distribution of the origins of electron pairs in the chamber. A film from Part IV of the experiment was used.

Fig. 5. Distribution of the direction of electron pairs with energies $\geq$ 0.5 GeV (Part IV).

Fig. 6. Photon spectra for maximum energies of 5.45 and 5.8 GeV respectively. The spectra a) and b) are normalized to the photon flux (E_γ > 0.1 GeV) of the films from Part I, II and III which were taken into consideration in this work.

The full curve represents a Bethe-Heitler brems-spectrum [34] with corrections for the finite target thickness and the collimation of the photon beam [8]; the spectrum was calculated for a thin titanium target. The dashed curve takes into consideration the finite measuring accuracy (above 1 GeV the relative measuring error for electron pairs is $\Delta E_\gamma / E_\gamma = 0.019 + E_\gamma/\text{GeV} \cdot 0.008$). The full curve was normalized to an equal area with the experimental spectrum above 3 GeV.

Fig. 7. Optical schematic of the bubble chamber.

Fig. 8. χ^2-distribution for the reaction $\gamma p \rightarrow p\pi^+\pi^-$.

Fig. 9. Distribution of $M_{\gamma 2}$ for the reaction $\gamma p \rightarrow p\pi^+\pi^-$.

$M_{\gamma 2}$ is defined in the text.

Fig. 10. Dependence of the unfitted photon mass on location in the chamber (reaction $\gamma p \rightarrow p\pi^+\pi^-$):
a. Mean value of $M_{\gamma 2}$ for all photon energies
b. Width of the distribution of $M_{\gamma 2}$ for photon energies smaller and larger than 1.8 GeV; σ is the standard deviation of the fitted Gaussian function.

Fig. 11. Cross section for electron-pair production on hydrogen (according to Wheeler and Lamb [36]).

Fig. 12. Flux function. The flux function holds for the films which were evaluated up to June 1966.

Fig. 13. Total cross section for the reaction $\gamma p \rightarrow p\pi^+\pi^-$.

Fig. 14. Cross sections for multiple pion production. The dashed curves were calculated from corresponding cross sections for $\pi^{\pm}p$-reactions by means of the vector-dominance model, the quark model and the isospin invariance [46].

Fig. 15. Distributions of the effective mass $Mp\pi^+$ in the reaction $\gamma p \rightarrow p\pi^+\pi^-$. Relativistic Breit-Wigner expressions with energy-dependent width were used in the fits in Figs. 15-17.

Fig. 16. Distribution of the effective mass $Mp\pi^-$.

Fig. 17. Distribution of the effective mass $M_{\pi^+\pi^-}$.

Fig. 17a. Distributions of the effective mass $M_{\pi^+\pi^-}$ for two photon-energy intervals above 2.5 GeV. The fits were accomplished using interference terms according to Söding.

Fig. 18. Total cross section for the reaction $\gamma p \rightarrow p\rho^0$.

Fig. 19. Differential cross section $d\sigma_\rho/d\Delta^2$ for four photon-energy intervals.

Fig. 20. Differential cross section $d\sigma_\rho/d\Omega$ in the center of mass system for four photon-energy intervals; Θ_ρ^* is the production angle.

Fig. 21. Density matrix elements in the Jackson system. Θ_ρ^* = = production angle in the center of mass system. The curves are obtained from the strong absorption model [57].

Fig. 22. Density matrix elements in the helicity system as a function of the production angle. The curves result from the model by Krass [6].

Fig. 23. Differential cross sections $d\sigma/d\Delta^2 dM\pi\pi$ for two regions of $M\pi^+\pi^-$ below 760 MeV.

Fig. 24. Differential cross sections $d\sigma/d\Delta^2 dM\pi\pi$ for two regions of $M\pi^+\pi^-$ above 760 MeV.

Fig. 25. Dependence of the $\pi^+\pi^-$-mass distribution on the production angle $\cos\Theta^*_\rho$ in the center of mass system for two photon-energy regions.

Fig. 26. Decay angle distributions W $(\cos\Theta_H)$ in the helicity system for two $\pi^+\pi^-$-mass regions. The curves are fitted. See report p. 73.

Fig. 27. Decay angle distribution W (ϕ_H) in the helicity system for two $\pi^+\pi^-$-mass regions. The curves are fitted.

Fig. 28. Dependence of the fit in the $p\pi^+$-mass distribution on the decay angle distribution of the ρ-meson.

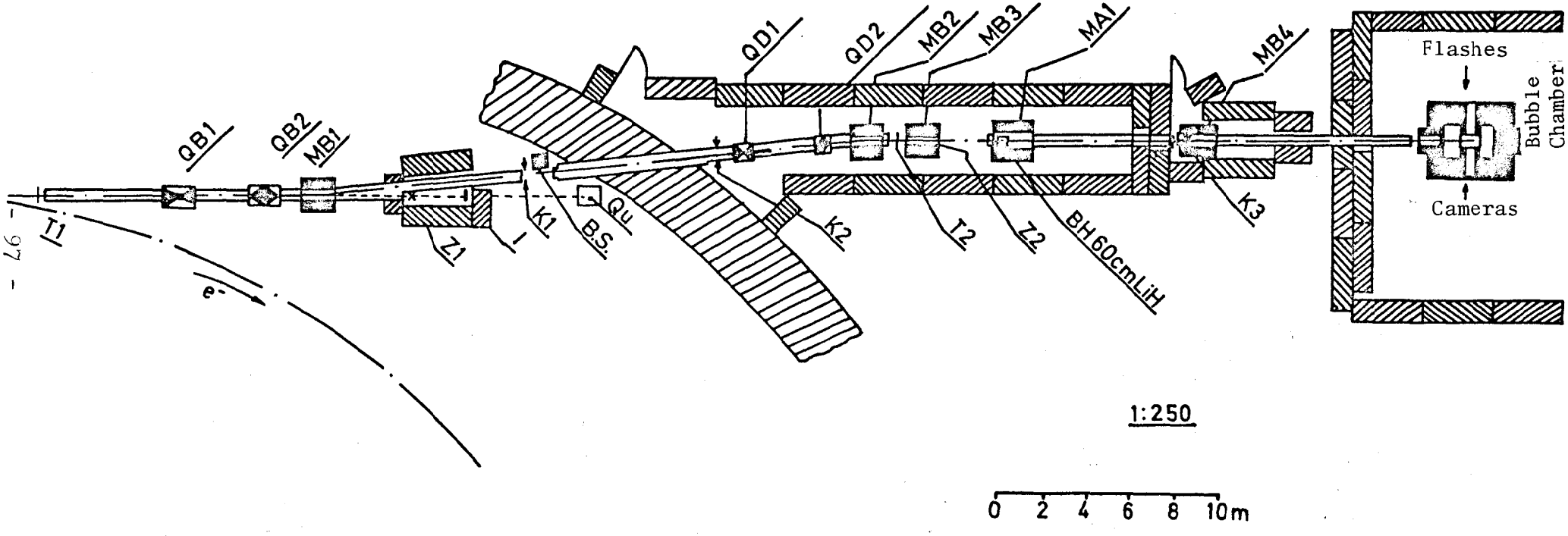

Fig. 1. Beam set-up.

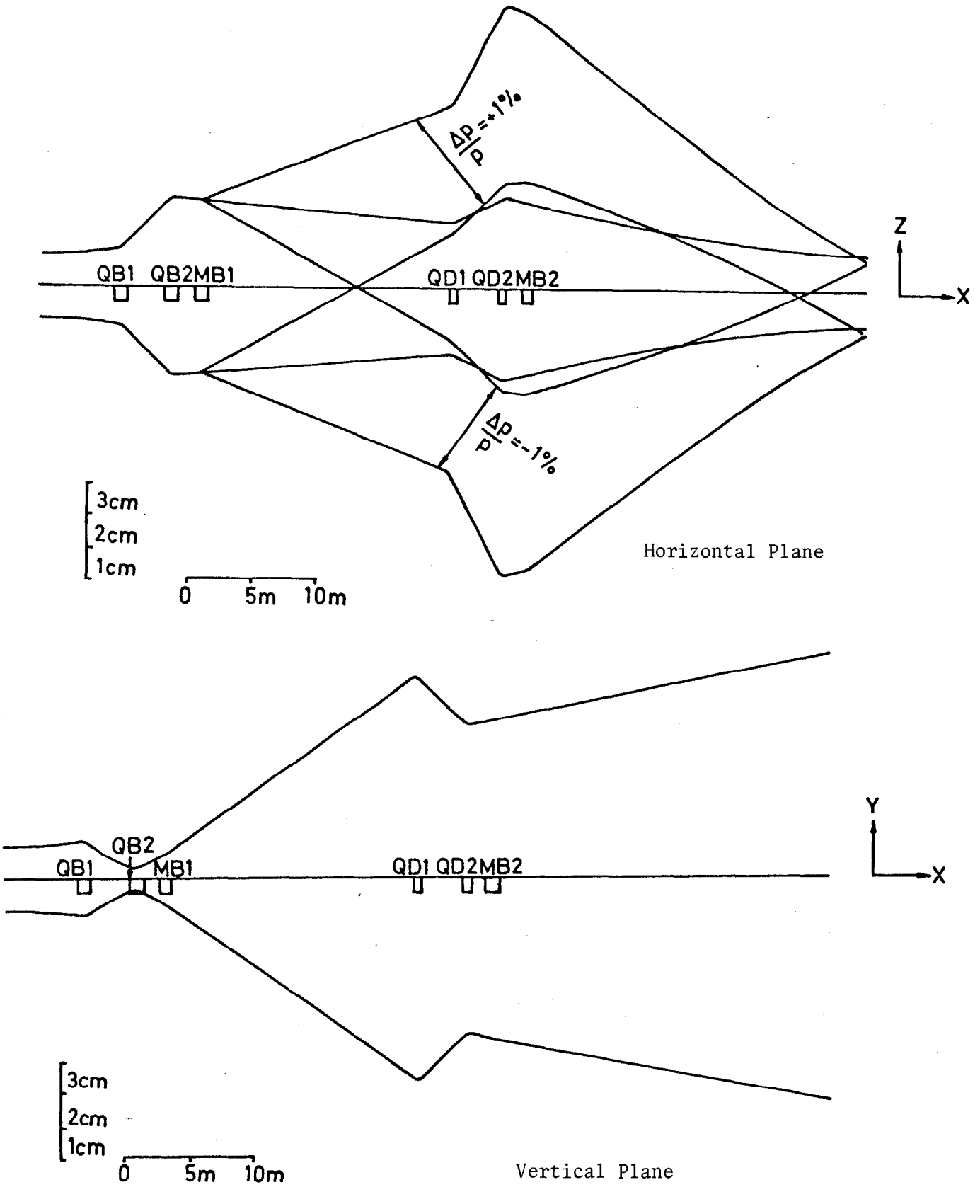

Fig. 2. Particle-trajectory envelopes.

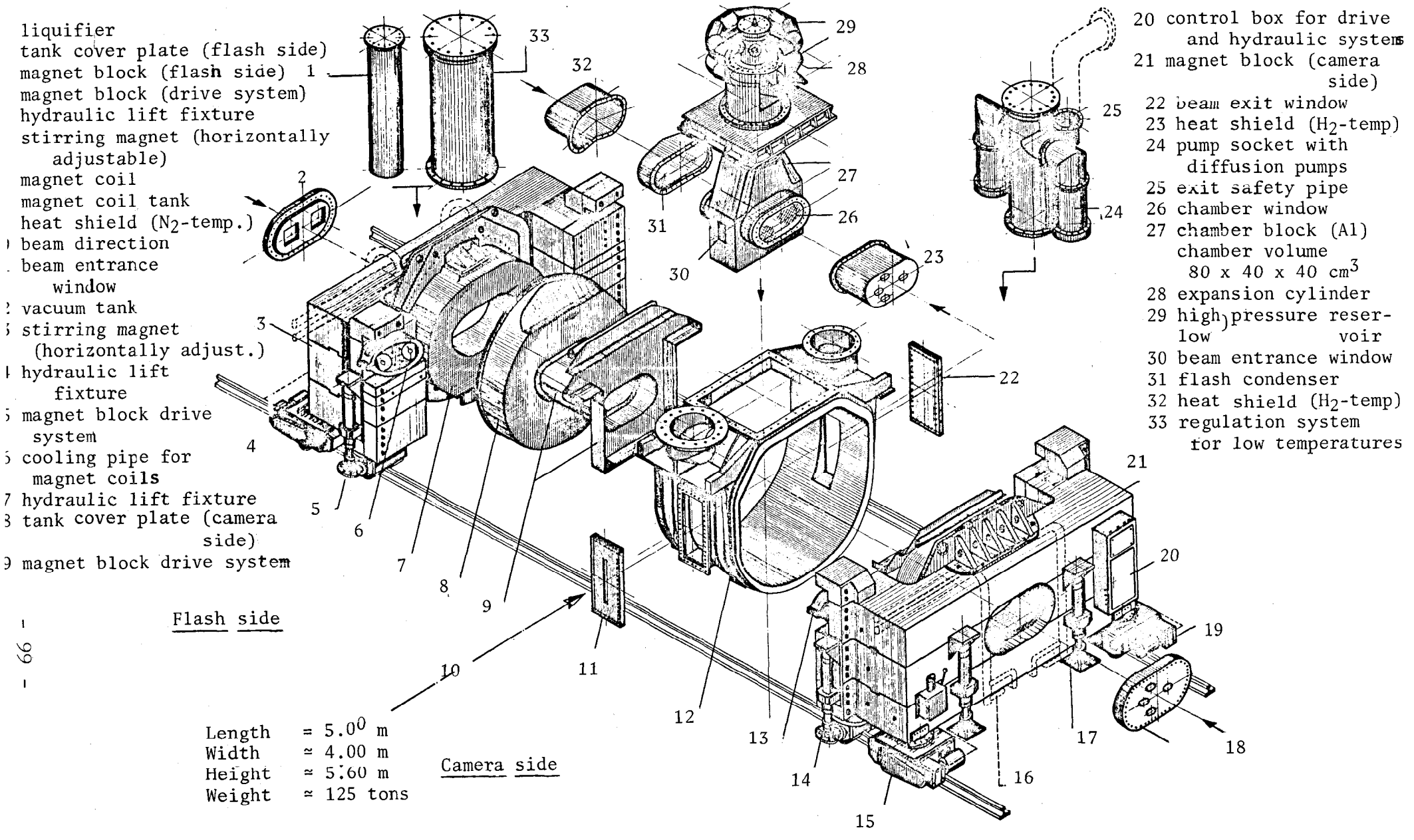

Fig. 3. Construction elements of the bubble chamber.

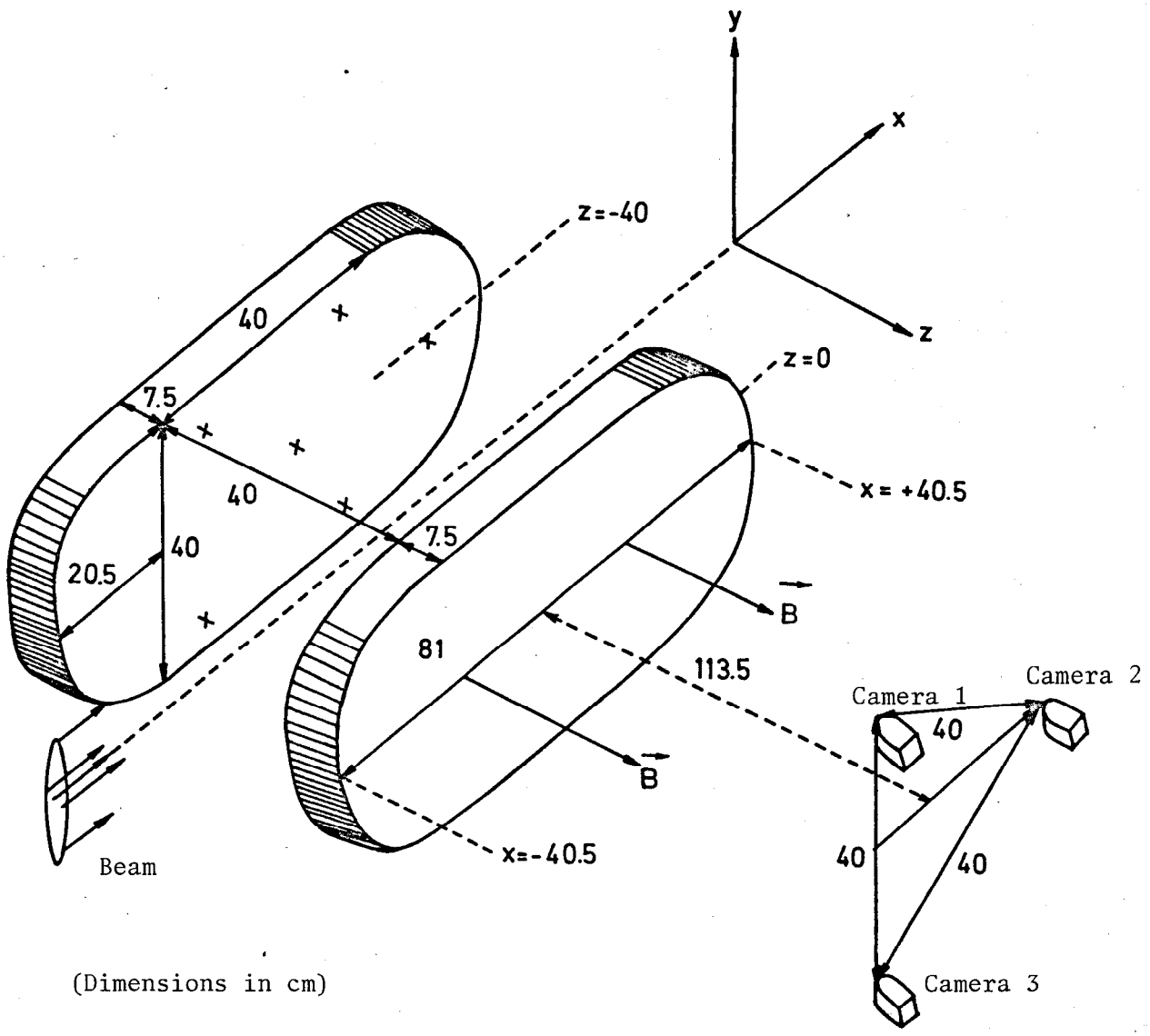

(Dimensions in cm)

Fig. 3. Schematic layout of the bubble chamber.
a. Chamber body with side windows and cameras
The point (x,y,z) =(0, 0,-20) is located
in the center of the chamber.

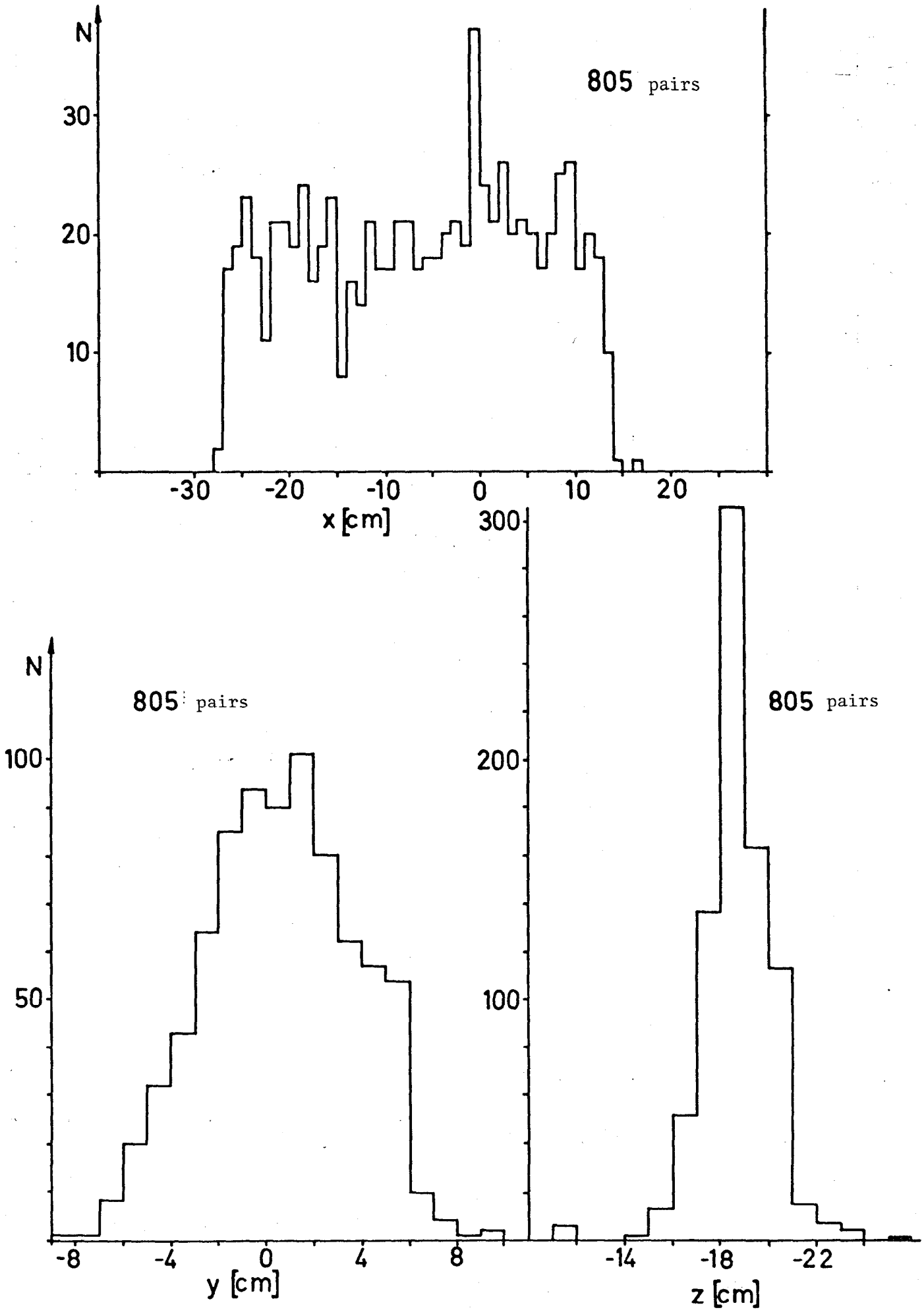

Fig. 4. Spatial distribution of the origins of electron pairs in the chamber.

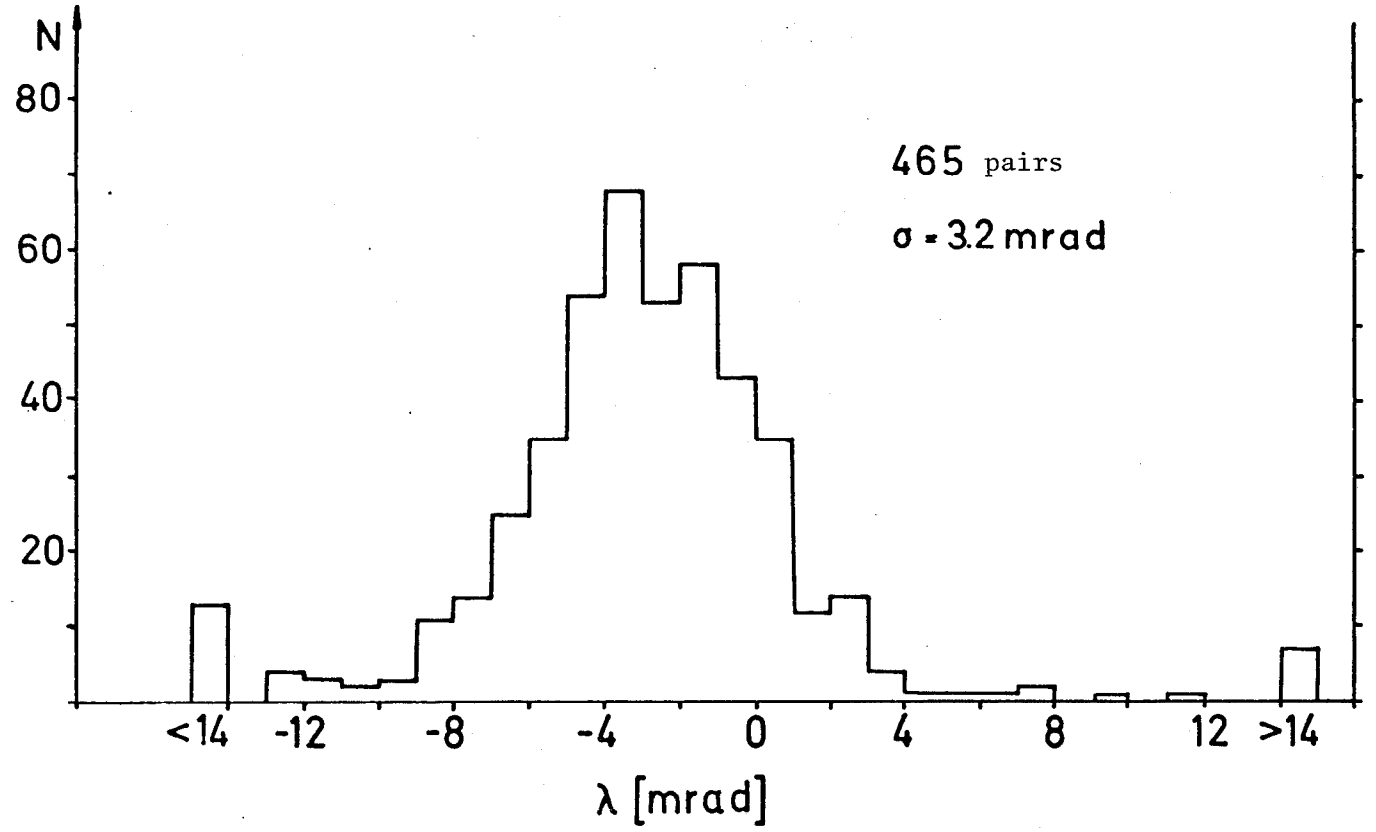

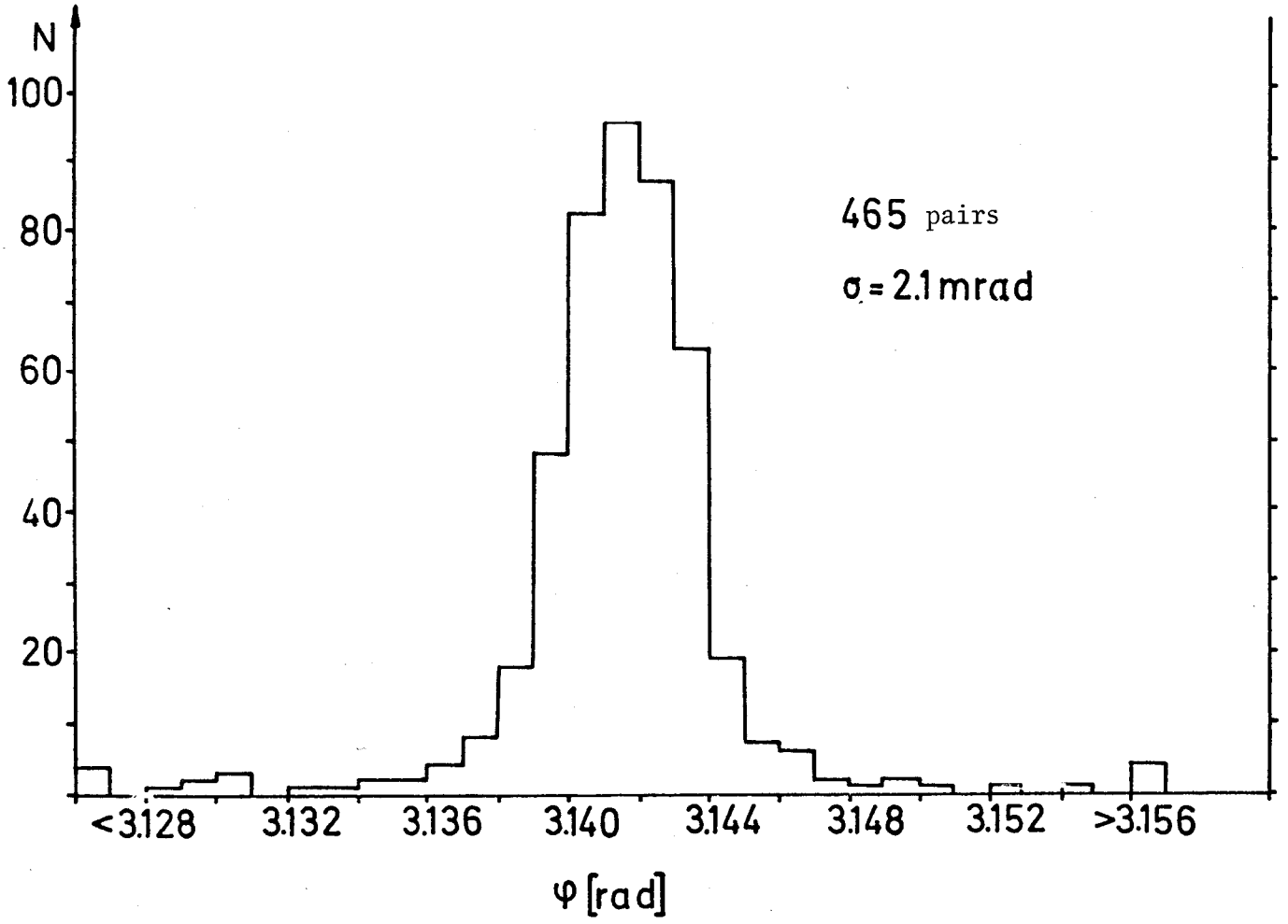

Fig. 5. Distribution of the direction of electron pairs with energies $\geq$ 0.5 GeV.

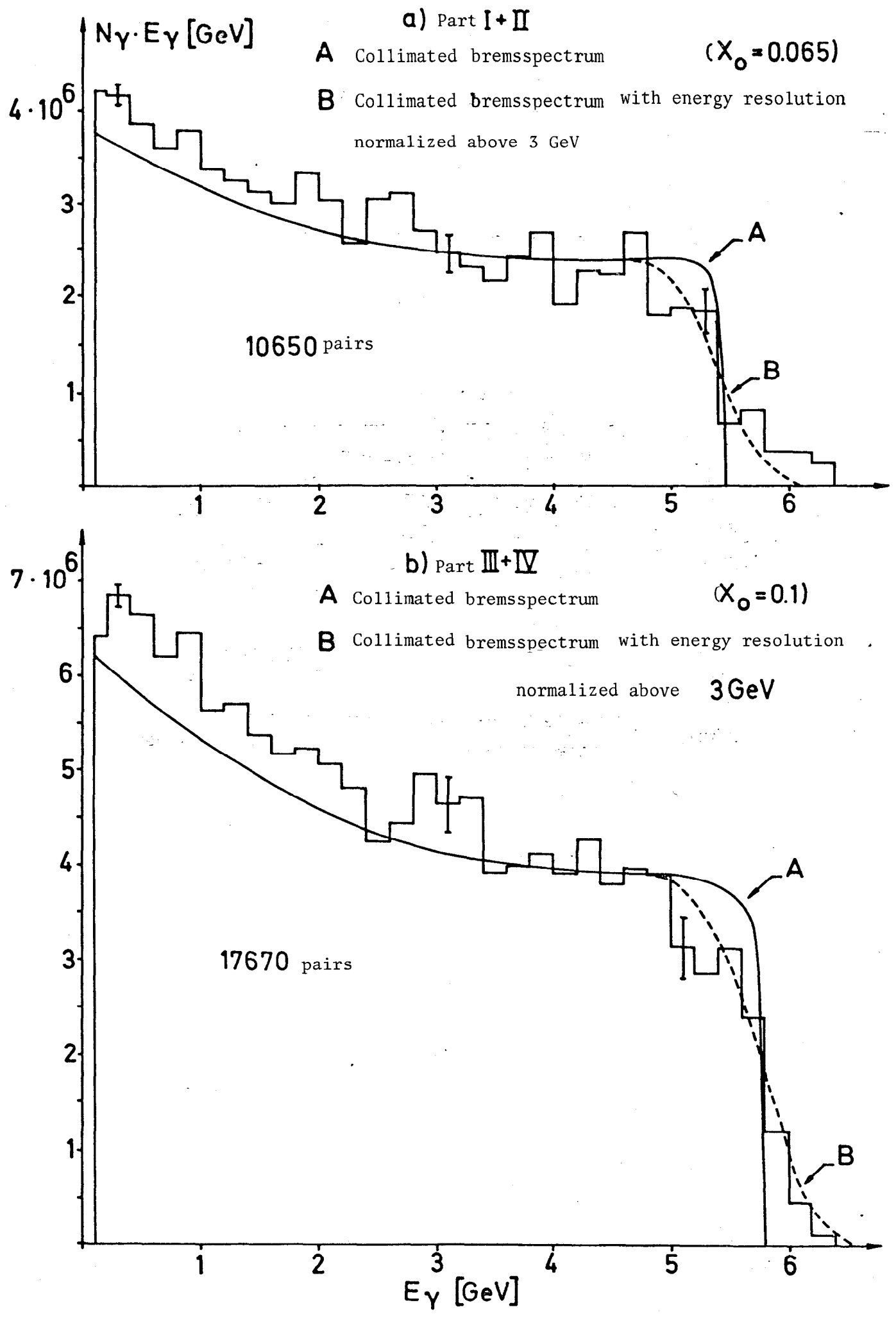

Fig. 6. Measured photon spectra ($E_\gamma > 0.1$ GeV)

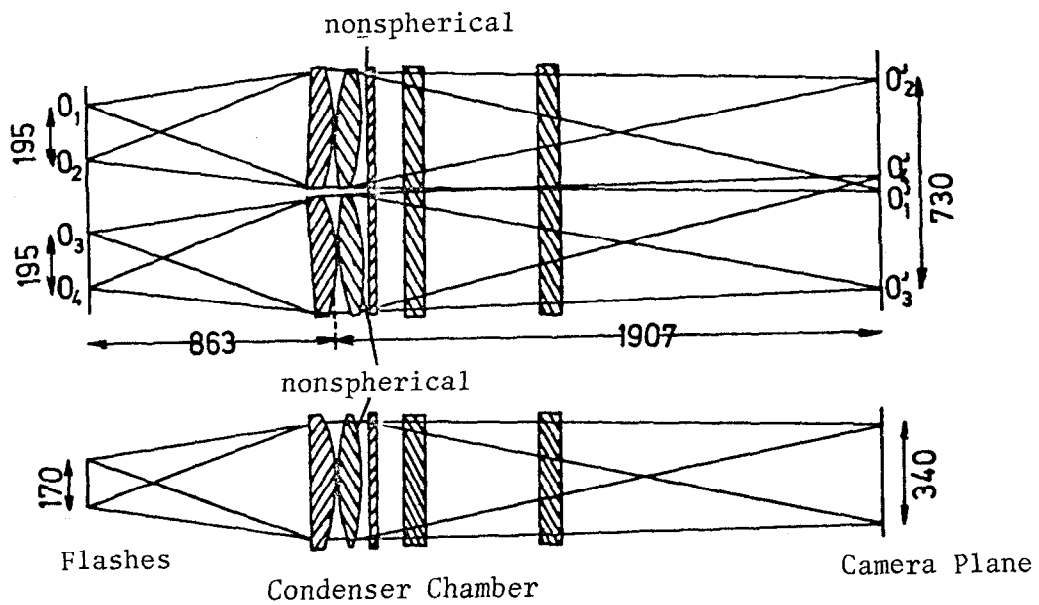

(dimensions in mm)

Fig. 7. Optical schematic of the bubble chamber.

Fig. 8. χ^2-distribution for the reaction $\gamma p \to p\pi^+\pi^-$.

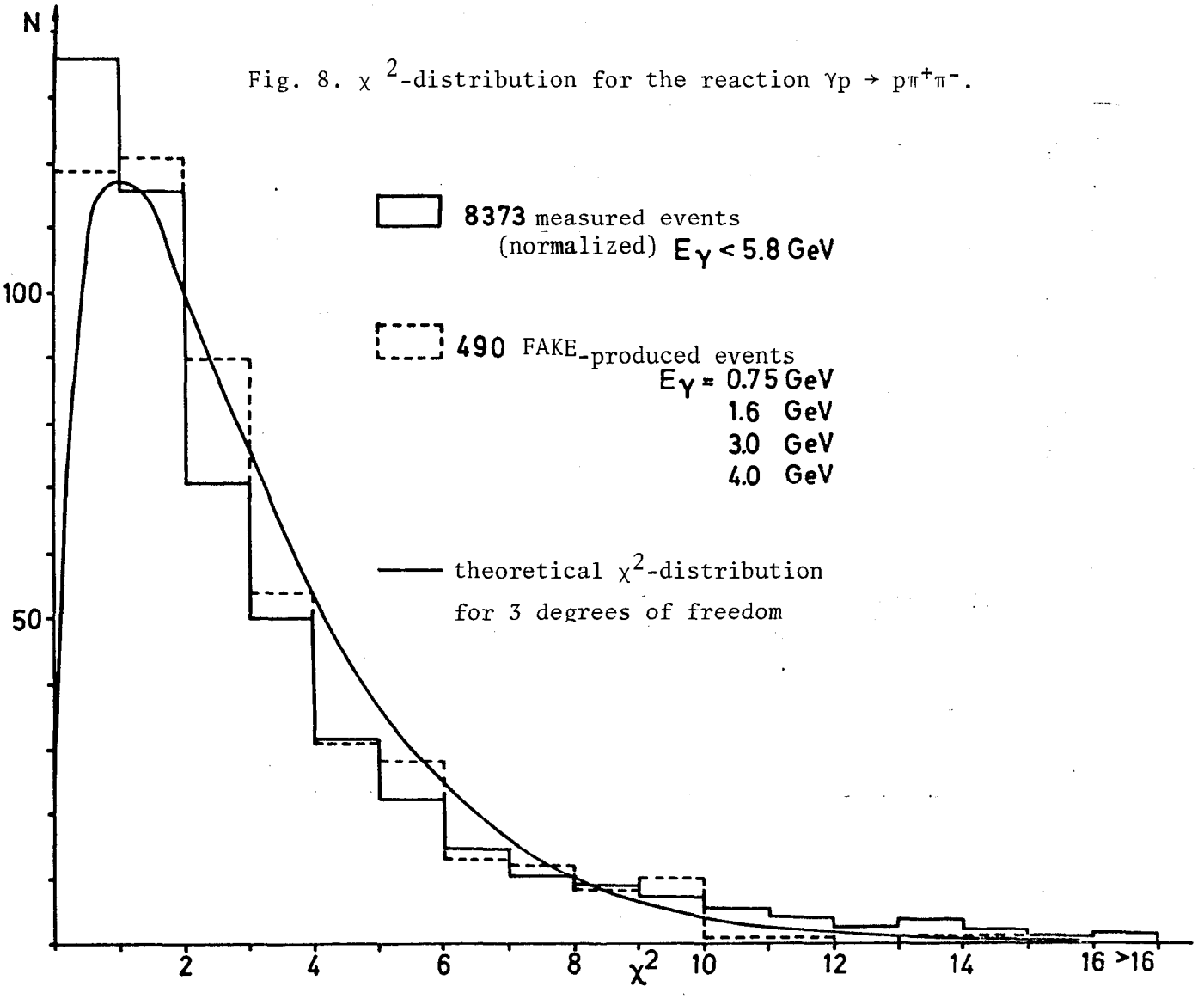

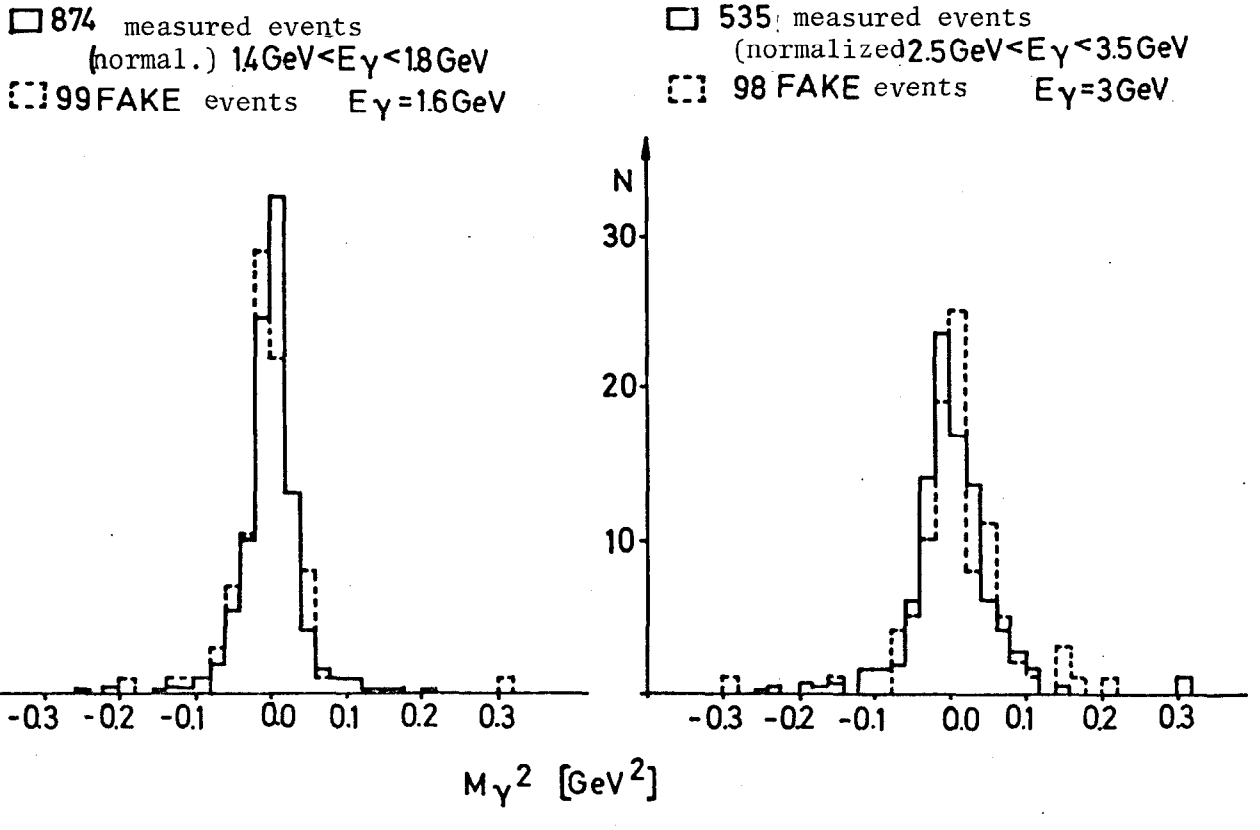

Fig. 9. Distribution of $M_{\gamma 2}$ for the reaction $\gamma p \to p\pi^+\pi^-$.

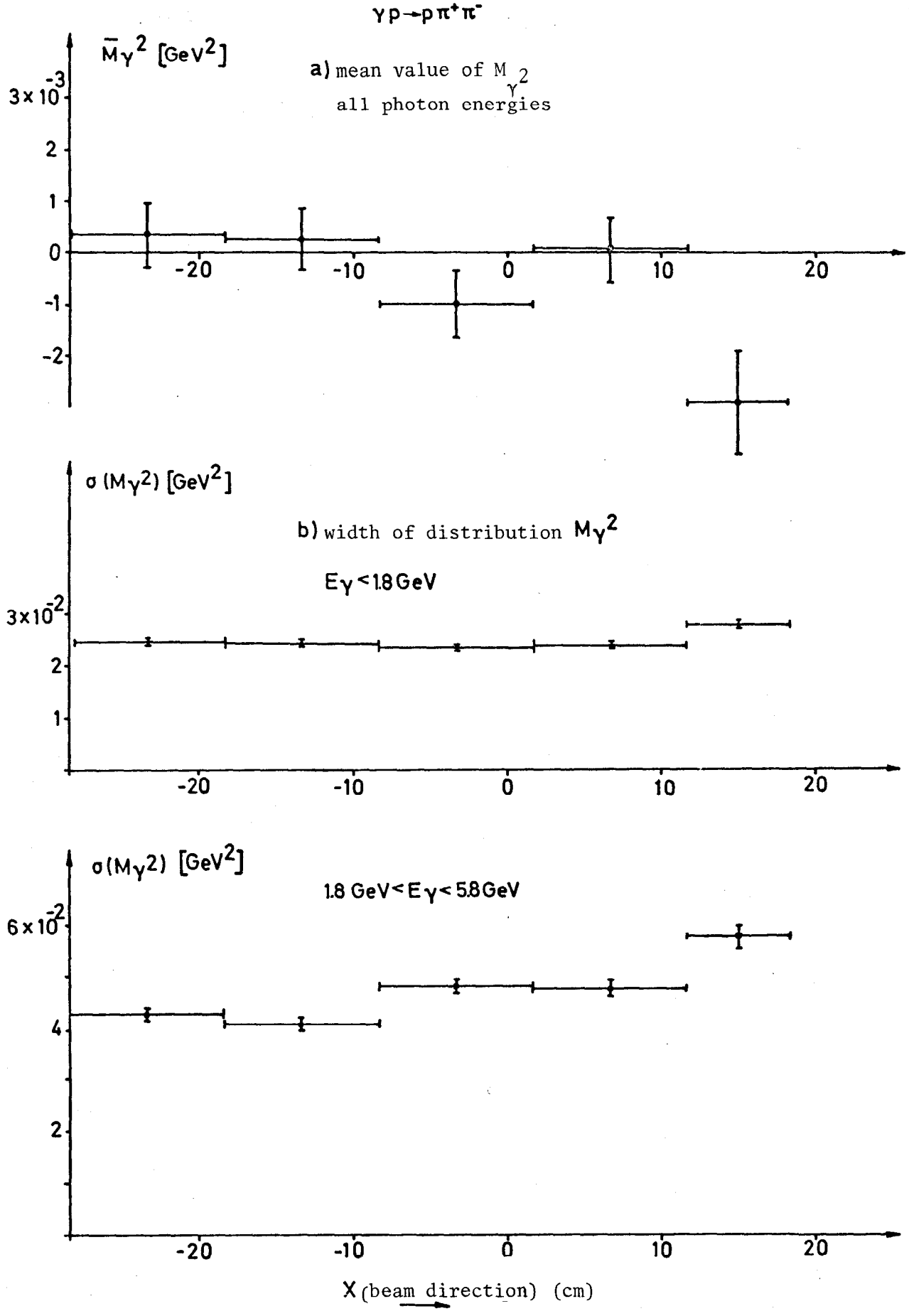

Fig. 10. Dependence of the unfitted photon mass on location in the chamber.

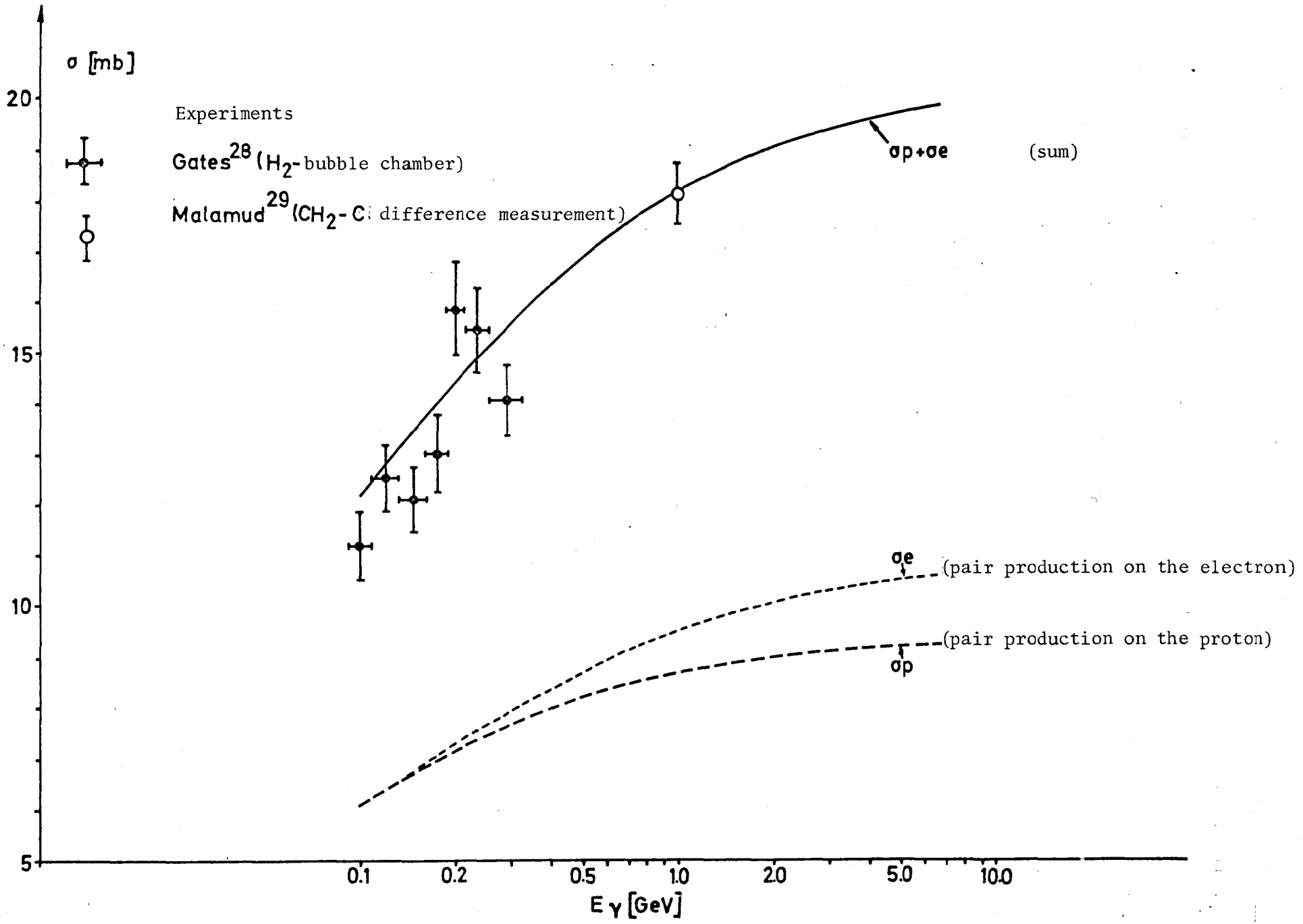

Fig. 11. Cross section for electron-pair production on hydrogen (according to Wheeler and Lamb) [36].

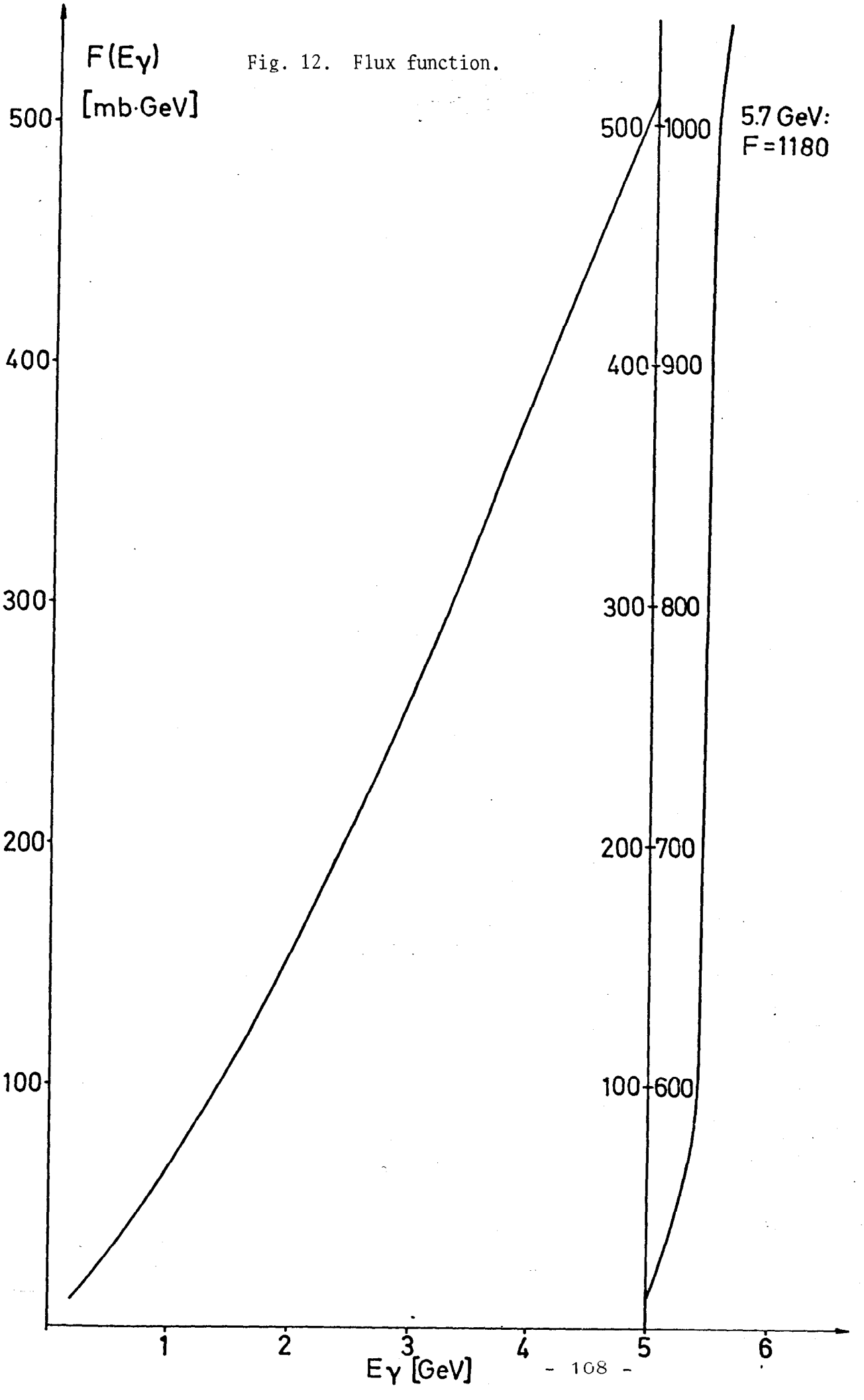

Fig. 12. Flux function.

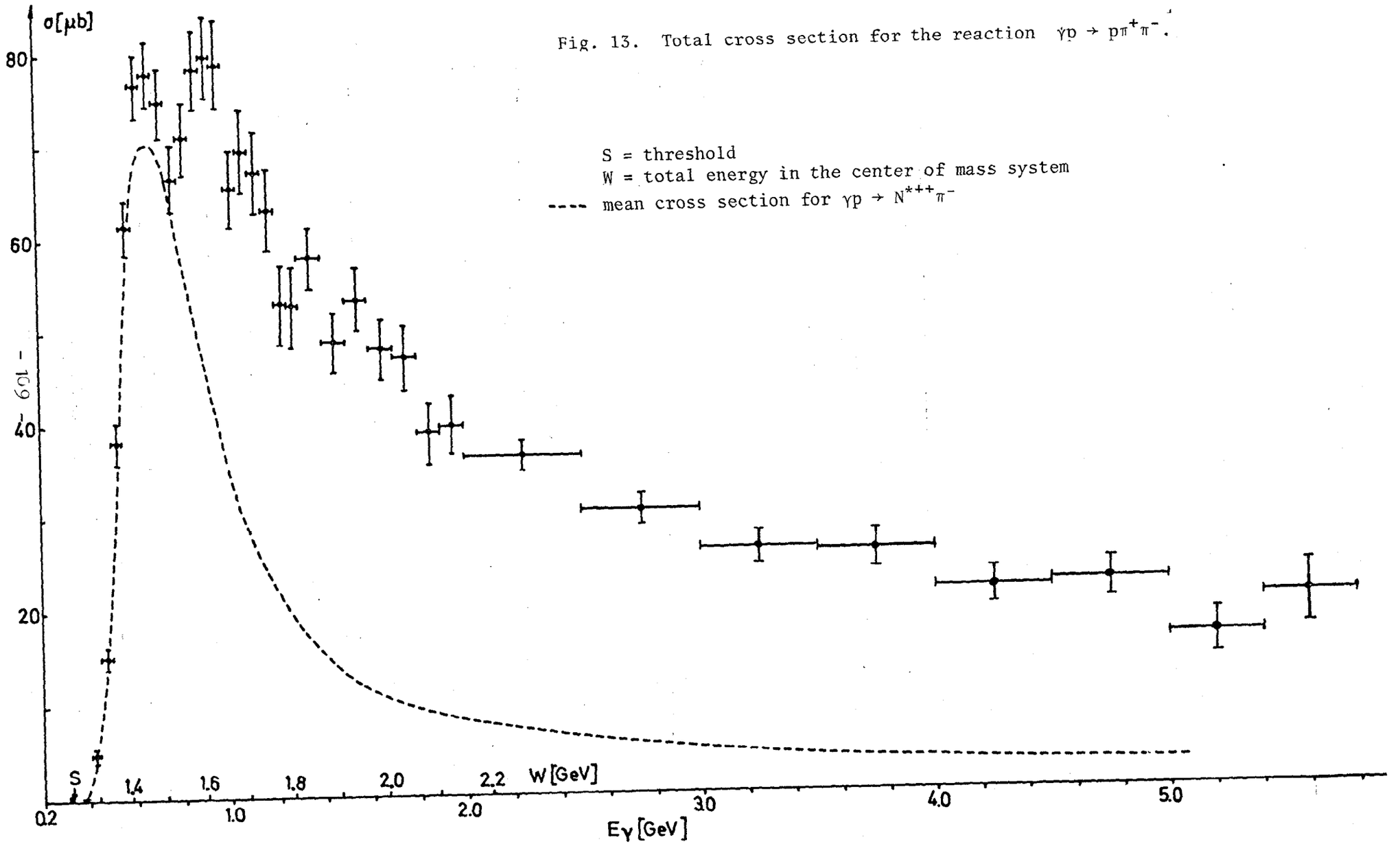

Fig. 13. Total cross section for the reaction $\gamma p \rightarrow p\pi^+\pi^-$.

S = threshold
W = total energy in the center of mass system
---- mean cross section for $\gamma p \rightarrow N^{*++}\pi^-$

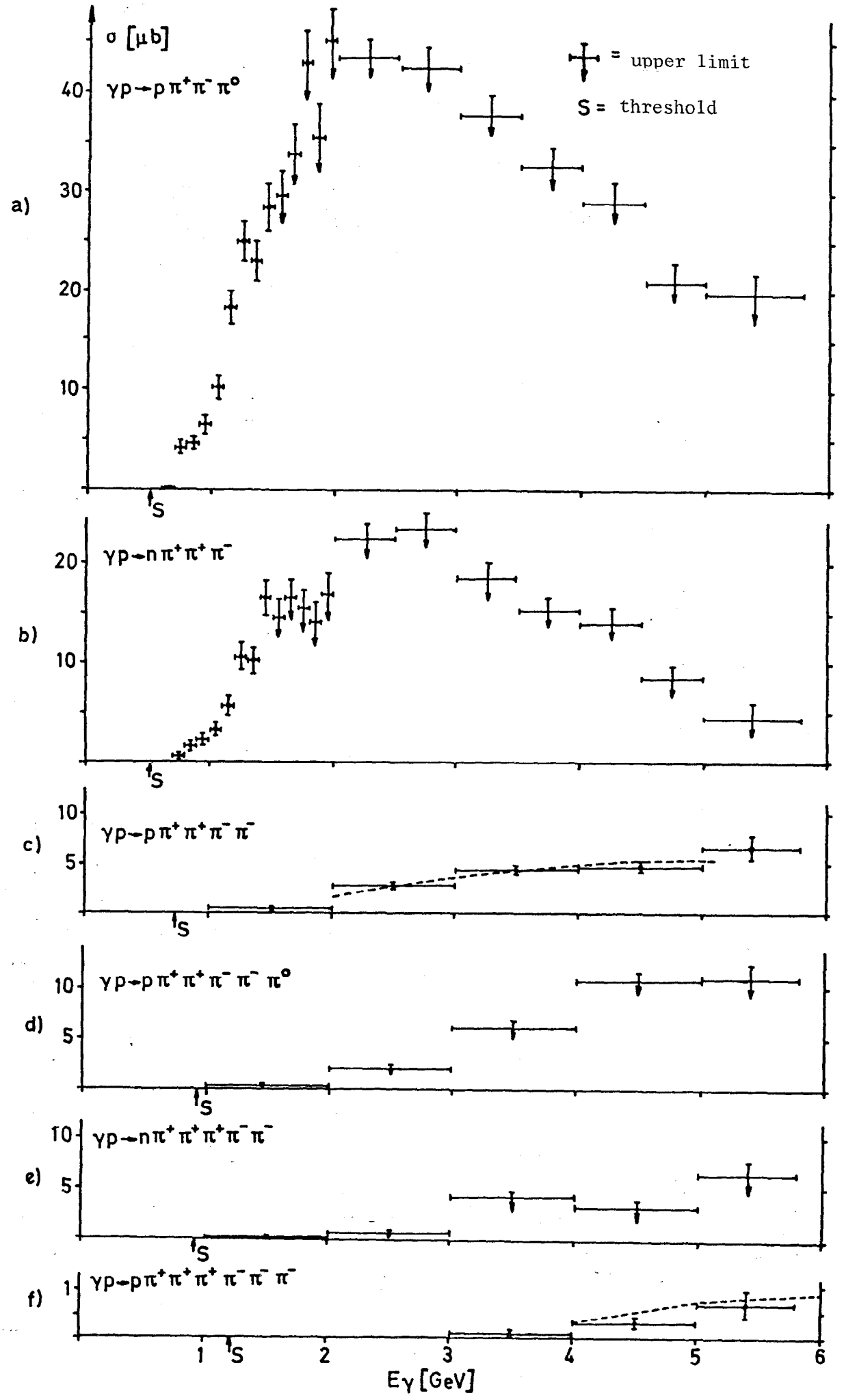

Fig. 14. Cross sections for multiple pion production.

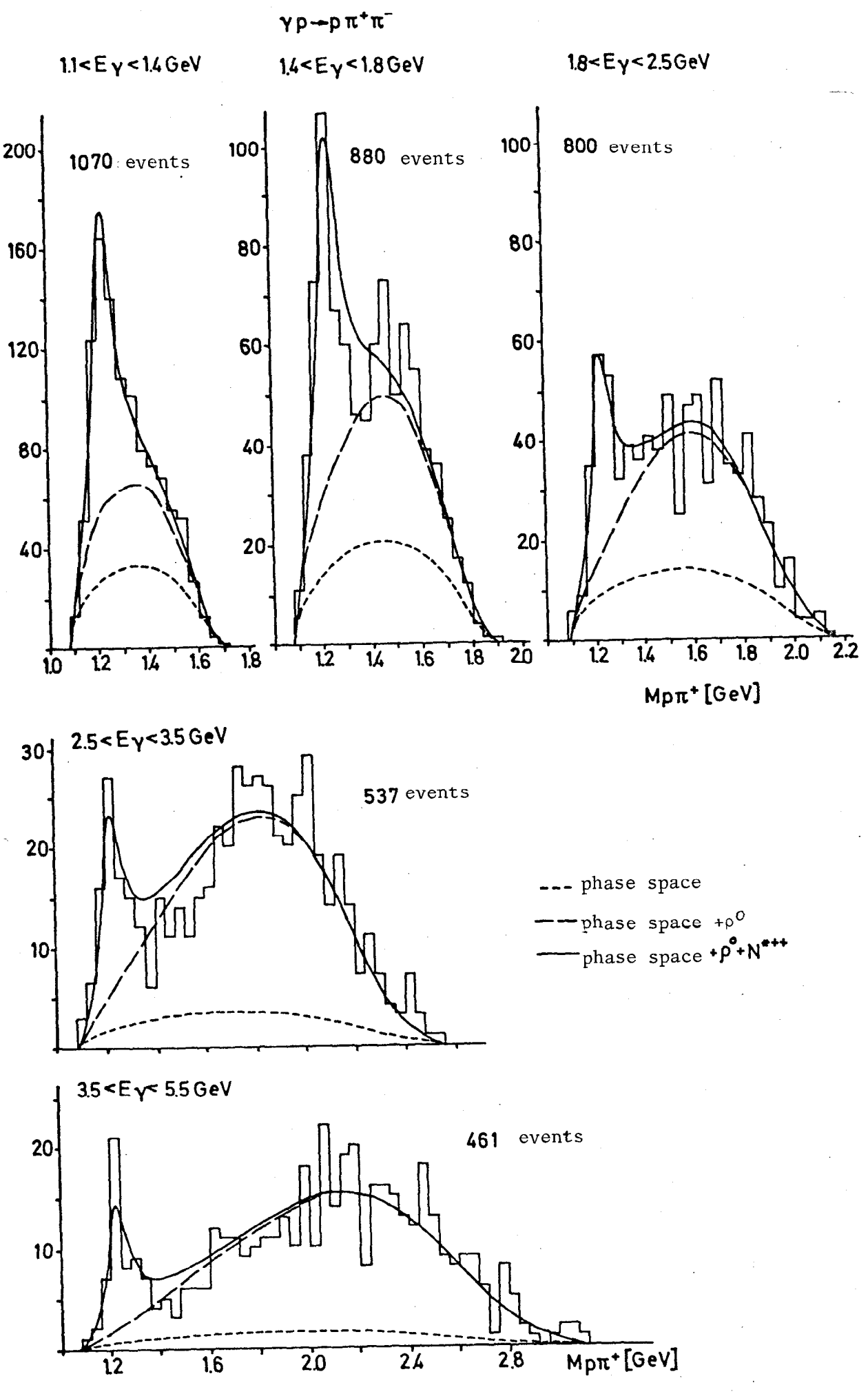

Fig. 15. Distribution of the effective mass $Mp\pi^+$.

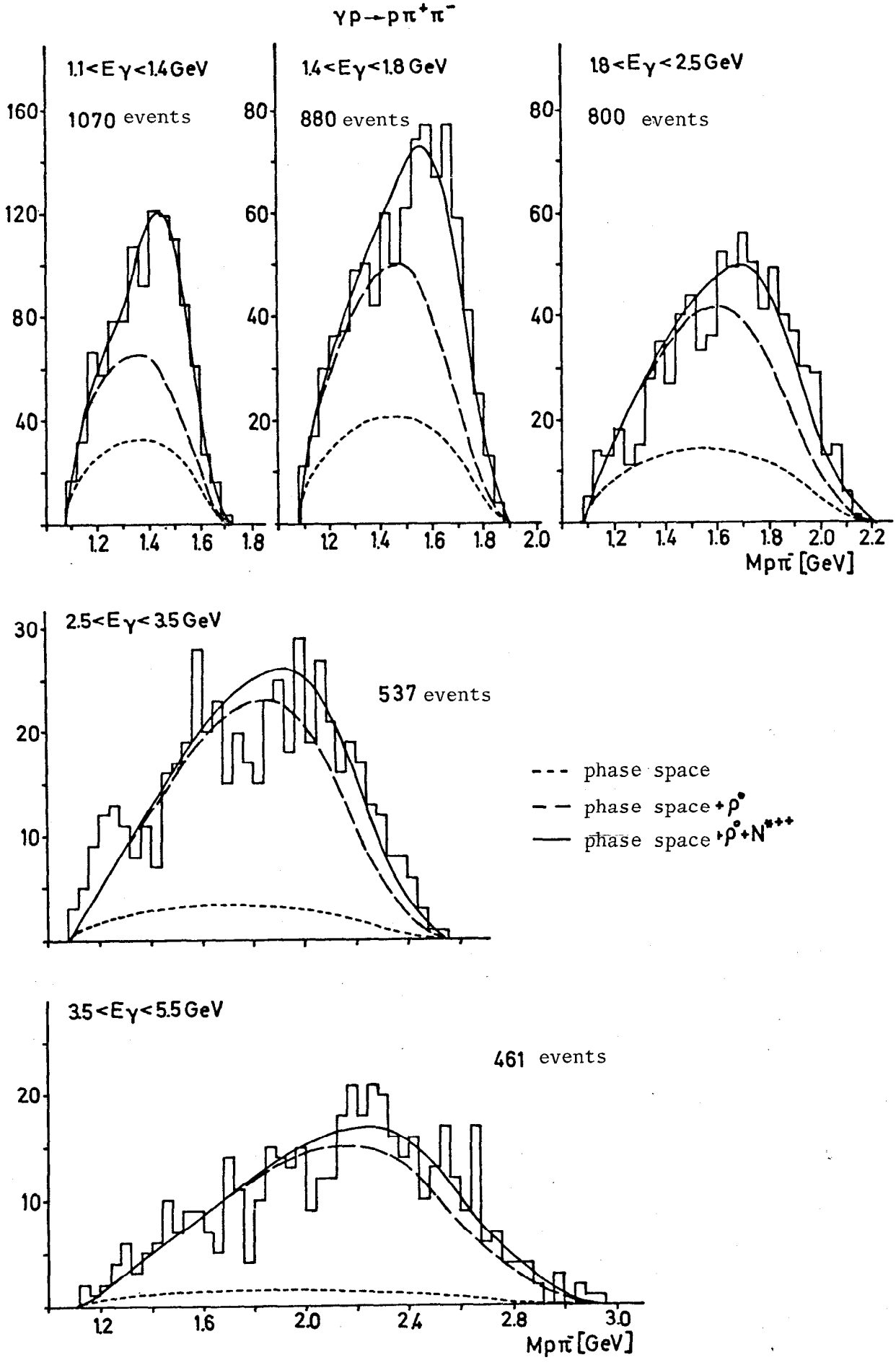

Fig. 16. Distribution of the effective mass $Mp\pi^-$.

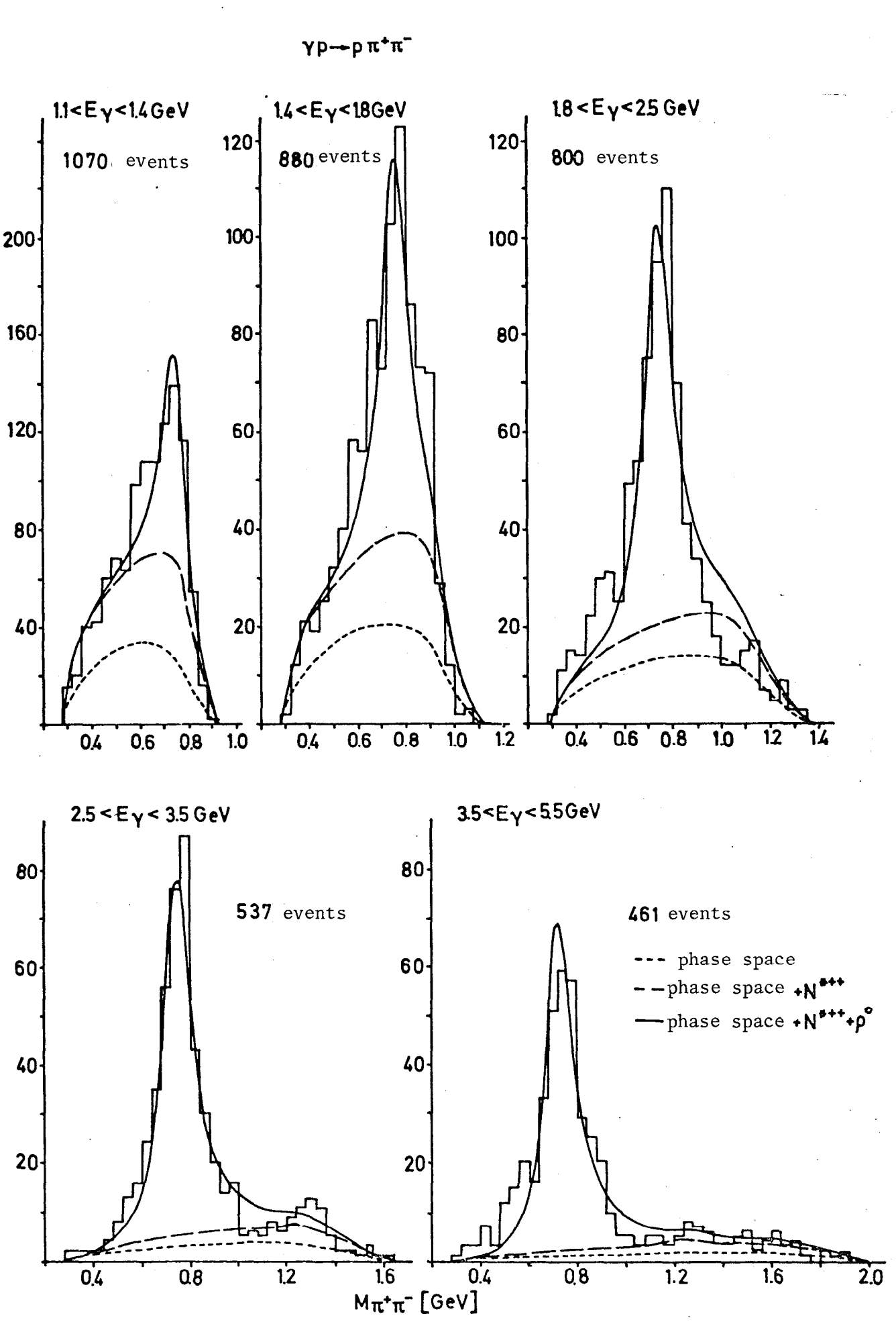

Fig. 17. Distribution of the effective mass $M_{\pi^+\pi^-}$.

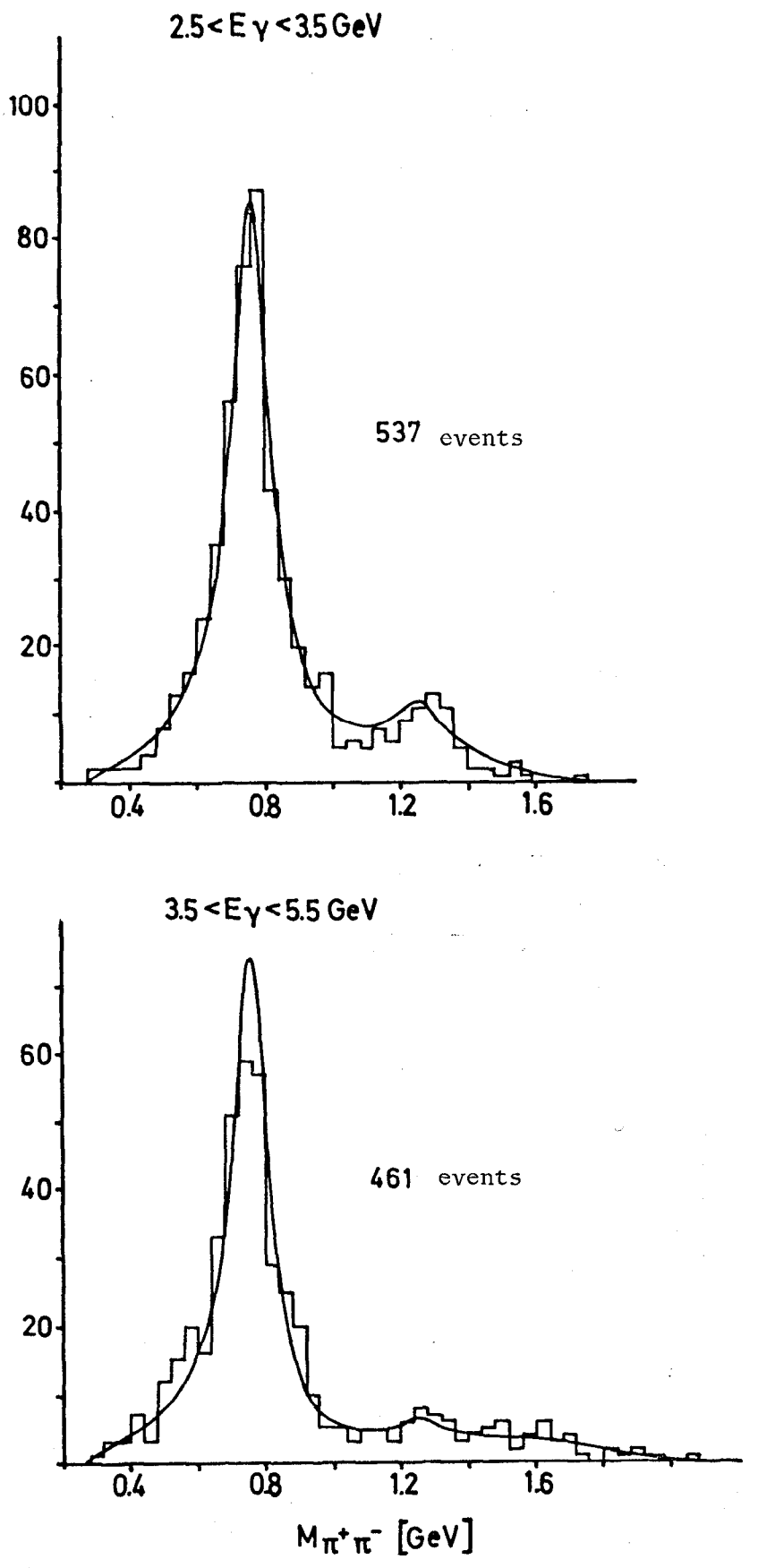

Fig. 17a. Distributions of the effective mass $M_{\pi^+\pi^-}$ above E_γ = 2.5 GeV. Fits with the interference term according to Söding.

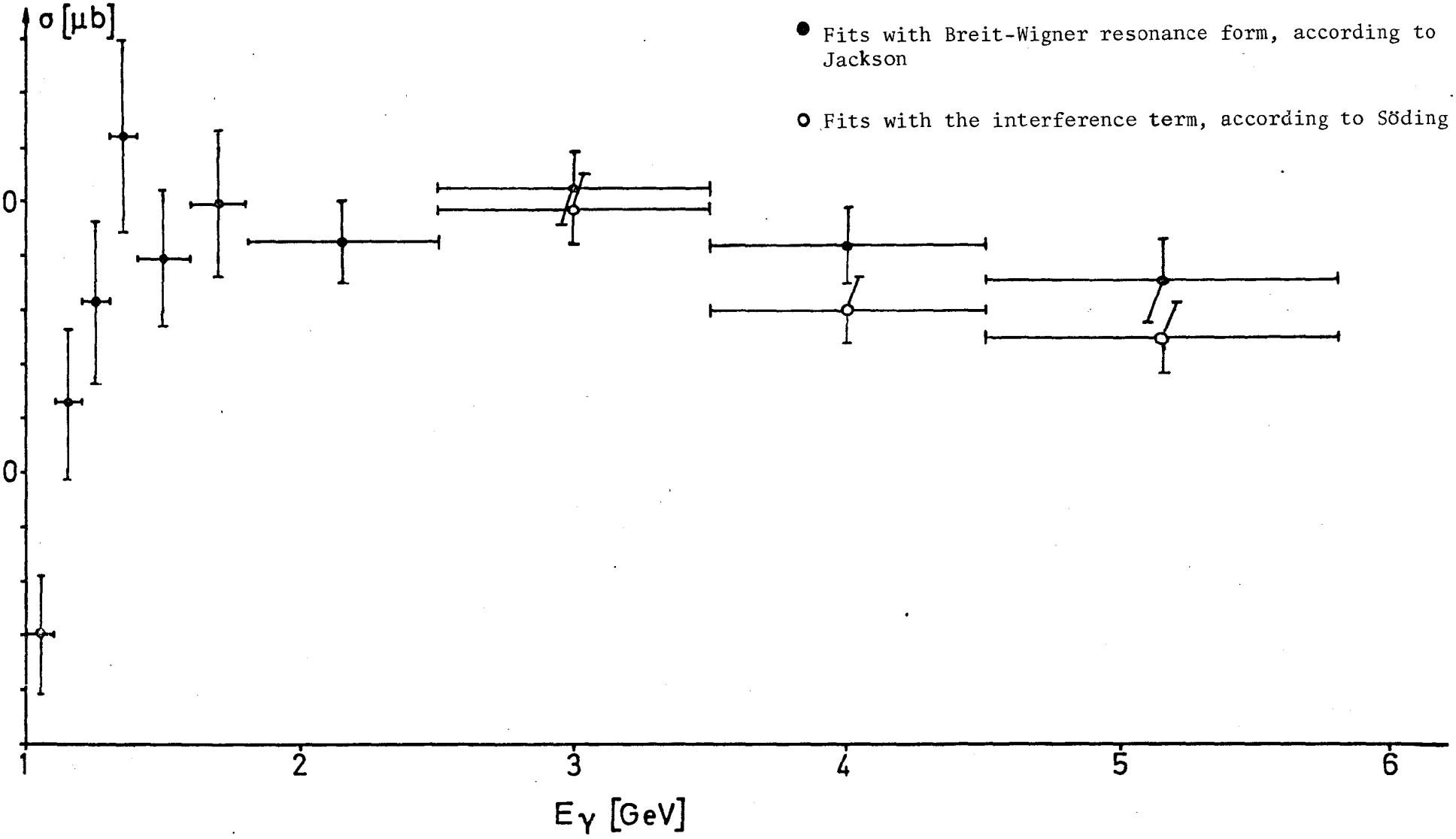

Fig. 18. Total cross section for the reaction $\gamma p \rightarrow p\rho^0$.

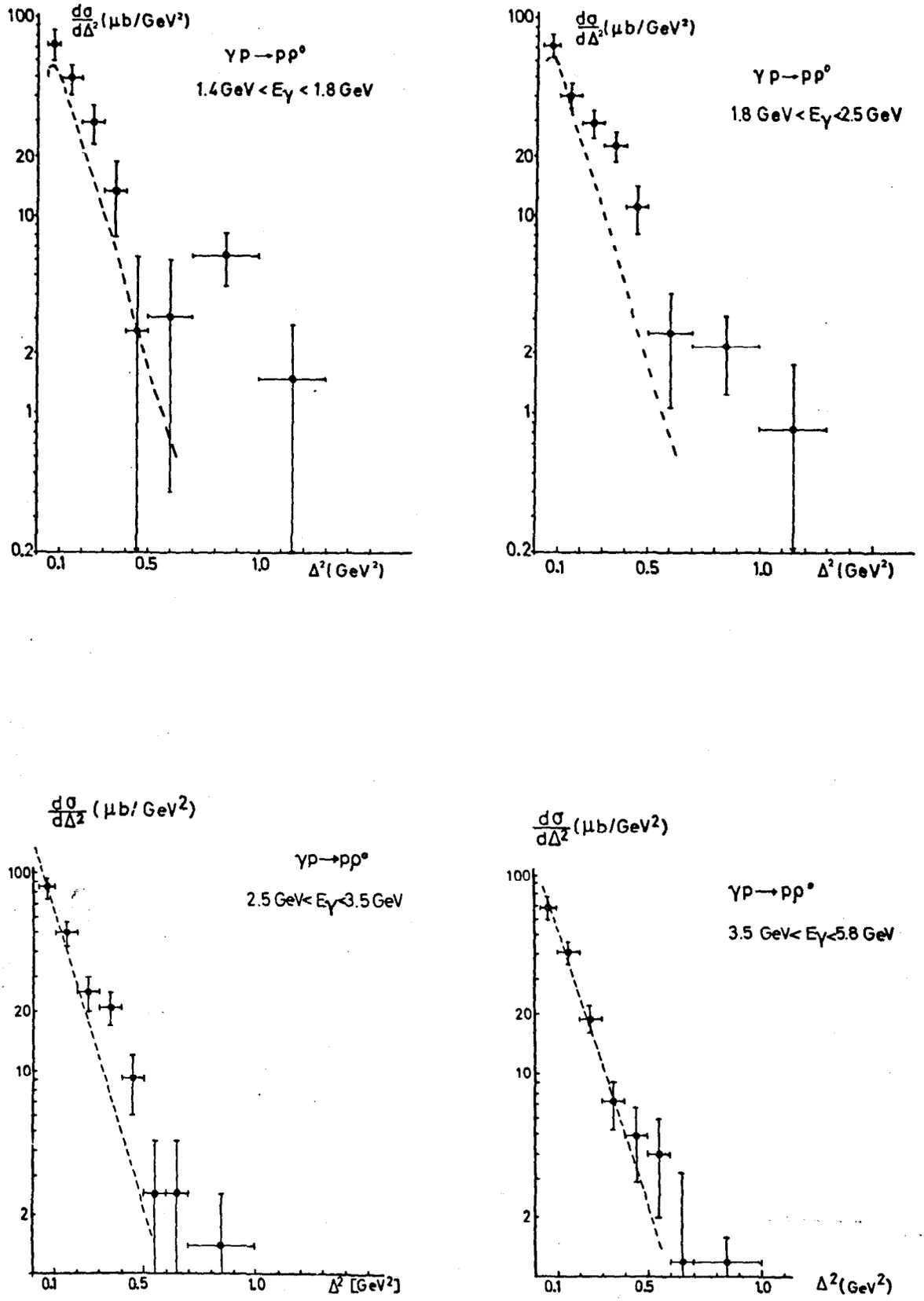

Fig. 19. Differential cross section $d\sigma_\rho/d\Delta^2$.

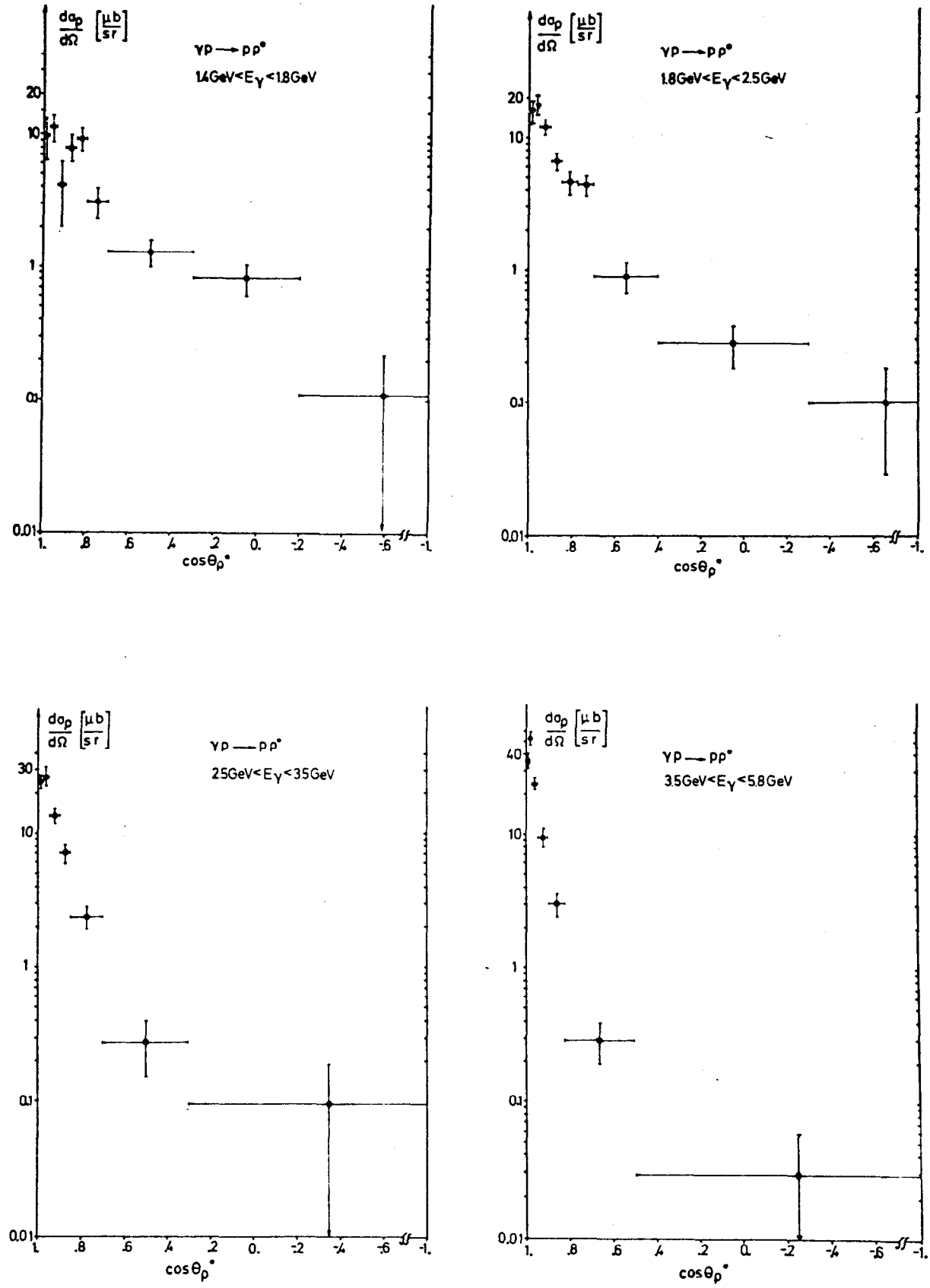

Fig. 20. Differential cross section $d\sigma_\rho/d\Omega$ in the center of mass system.

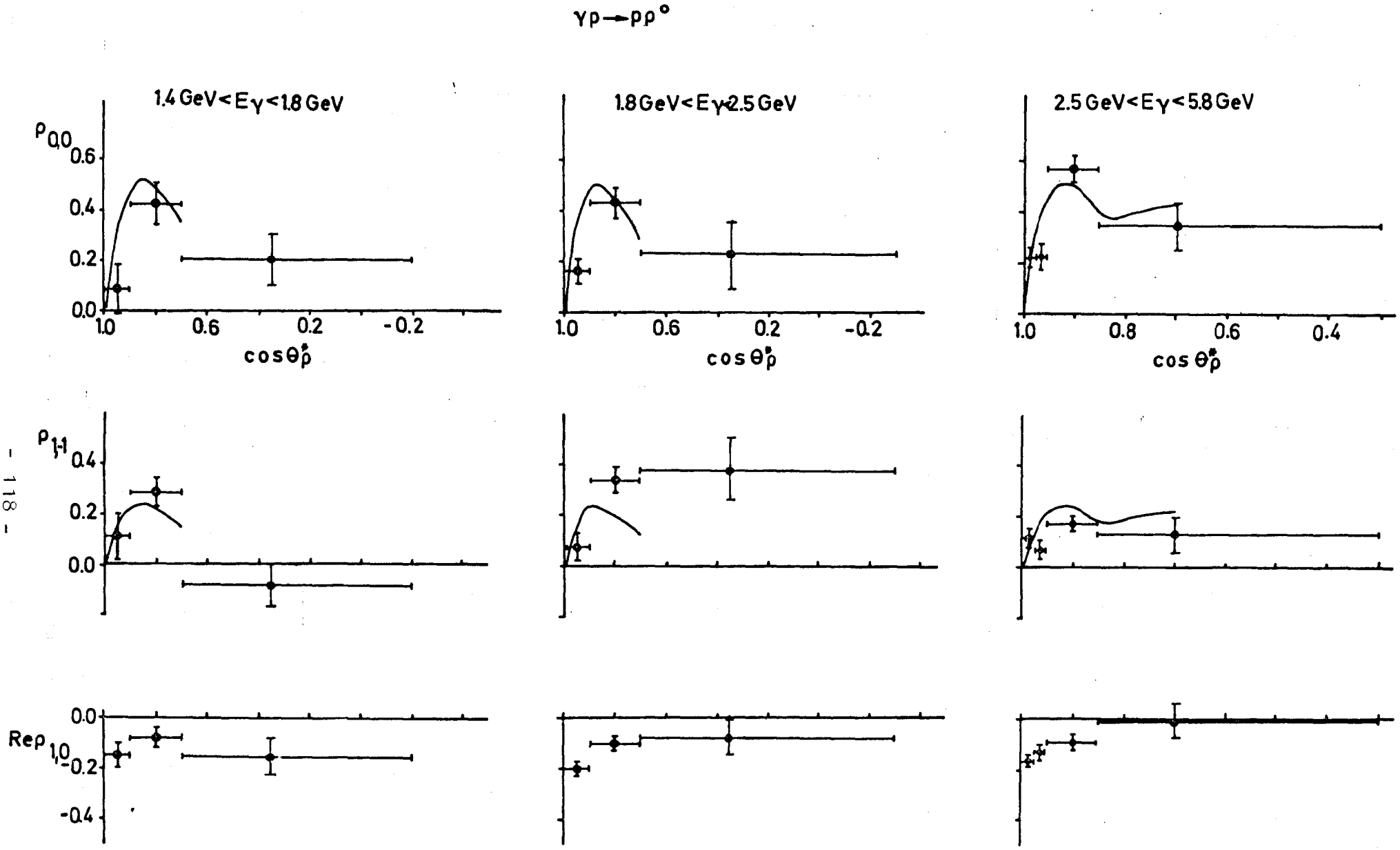

Fig. 21. Density matrix elements in the Jackson system. θ_ρ^* = production angle in the center of mass system. The curves are obtained from the strong absorption model.

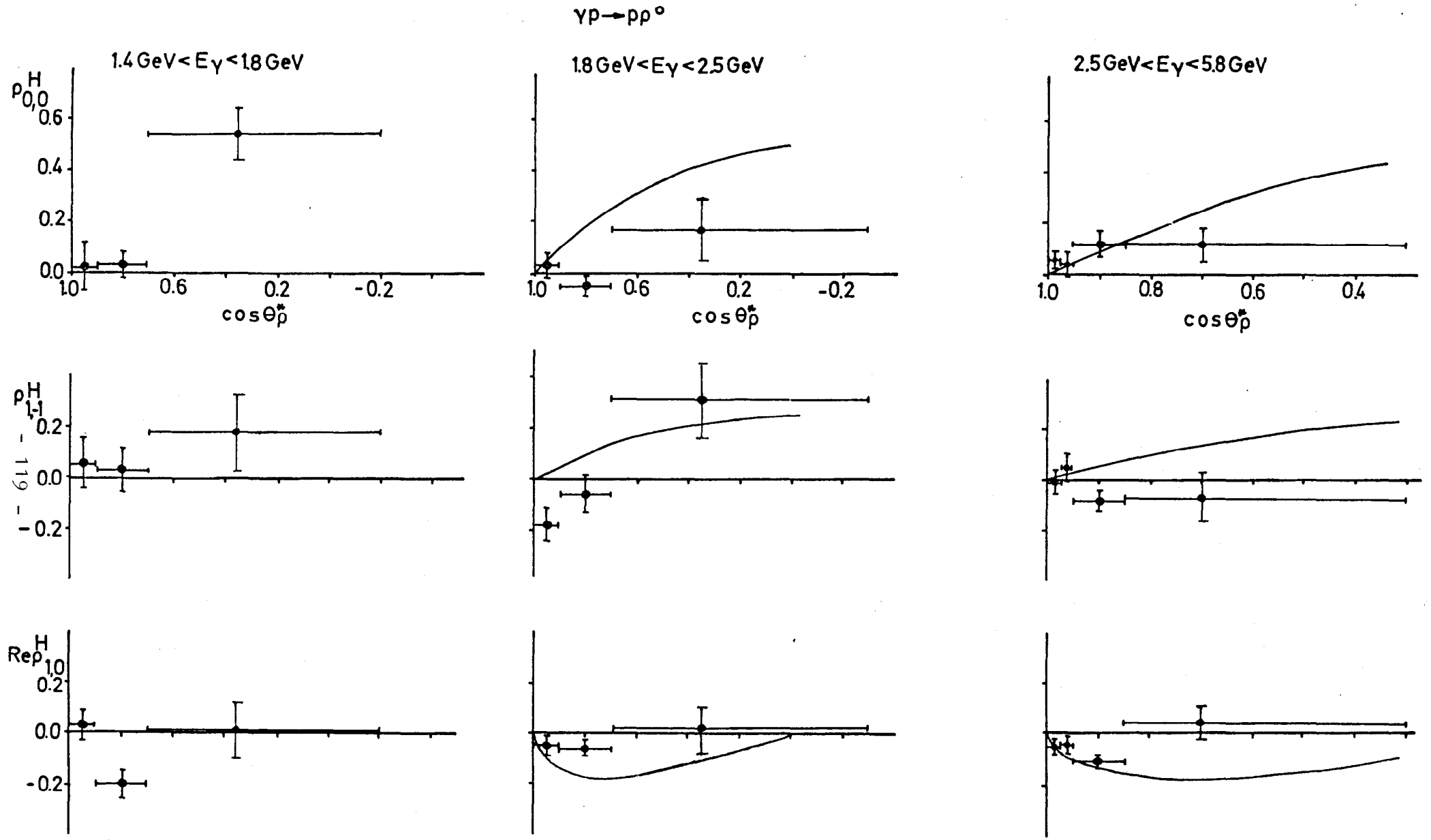

Fig. 22. Density matrix elements in the helicity system. θ_ρ^* = production angle in the center of mass system. The curves are obtained from the model by Krass.

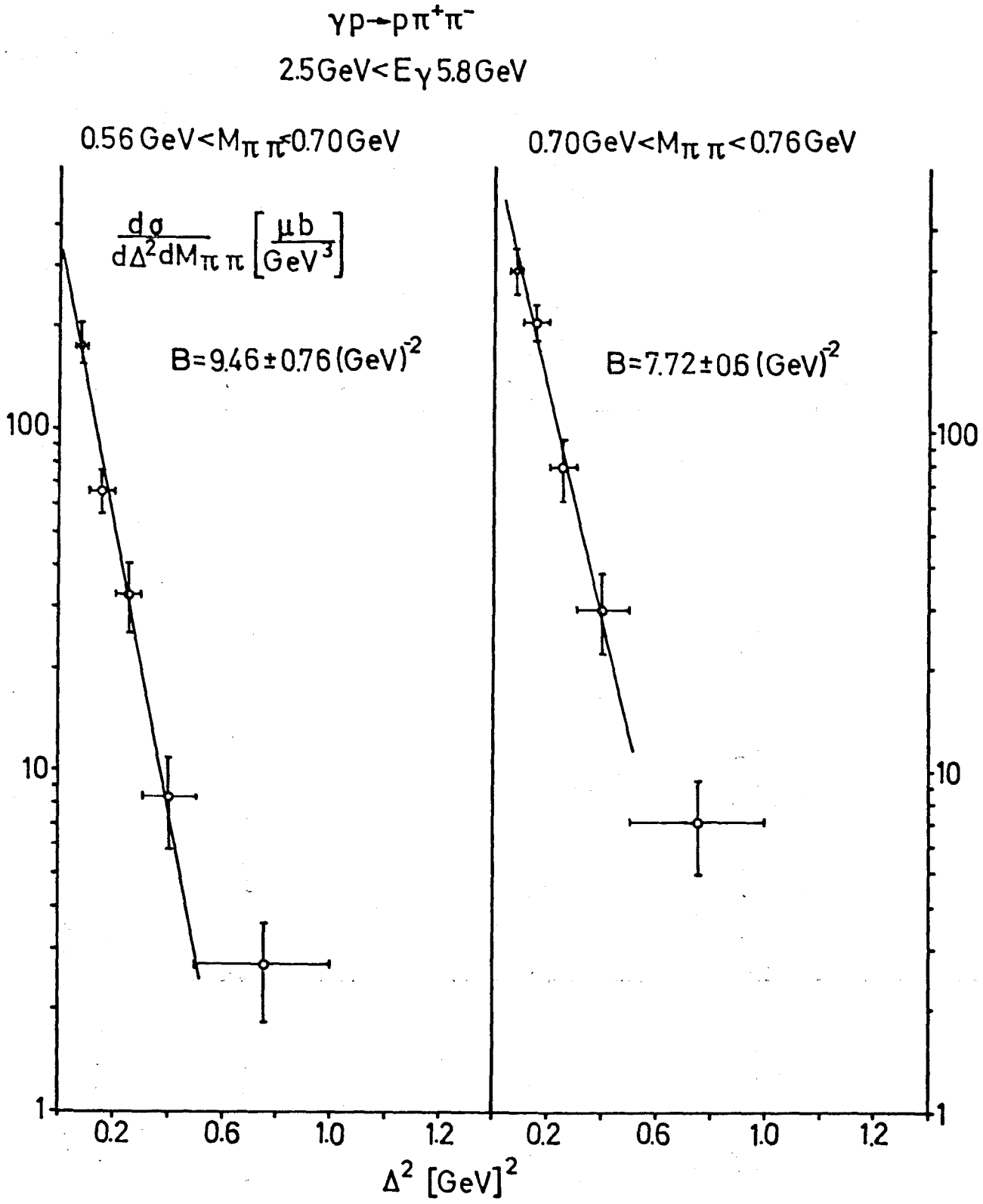

Fig. 23. Differential cross sections for dipion production in different regions of $M_{\pi^+\pi^-}$. Fit $Ae^{-B\Delta^2}$ for $\Delta^2 < 0.5$ GeV.

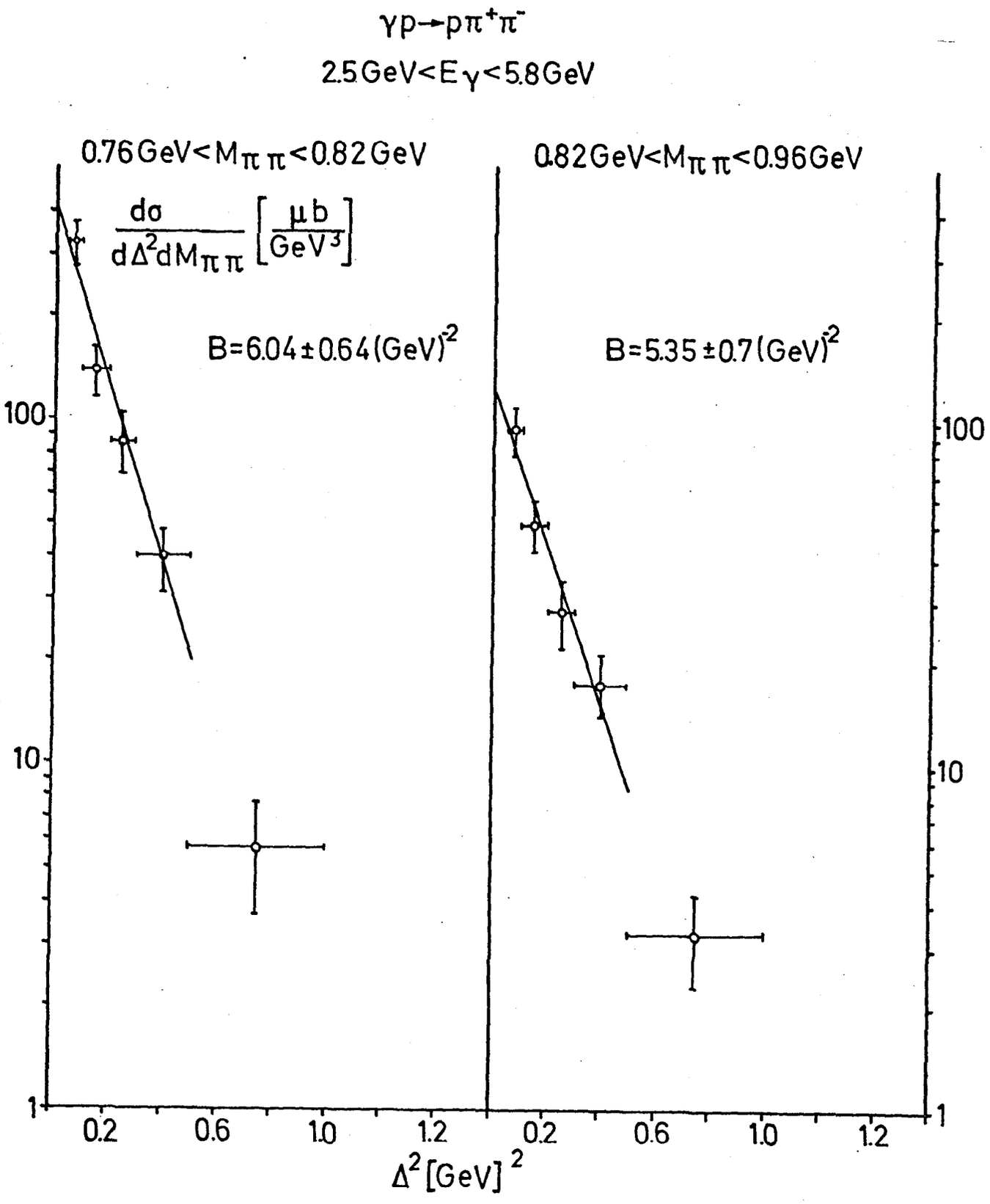

Fig. 24. Differential cross sections for dipion production in various regions of $M_{\pi^+\pi^-}$. Fit $Ae^{-B\Delta^2}$ for $\Delta^2 < 0.5$ GeV^2.

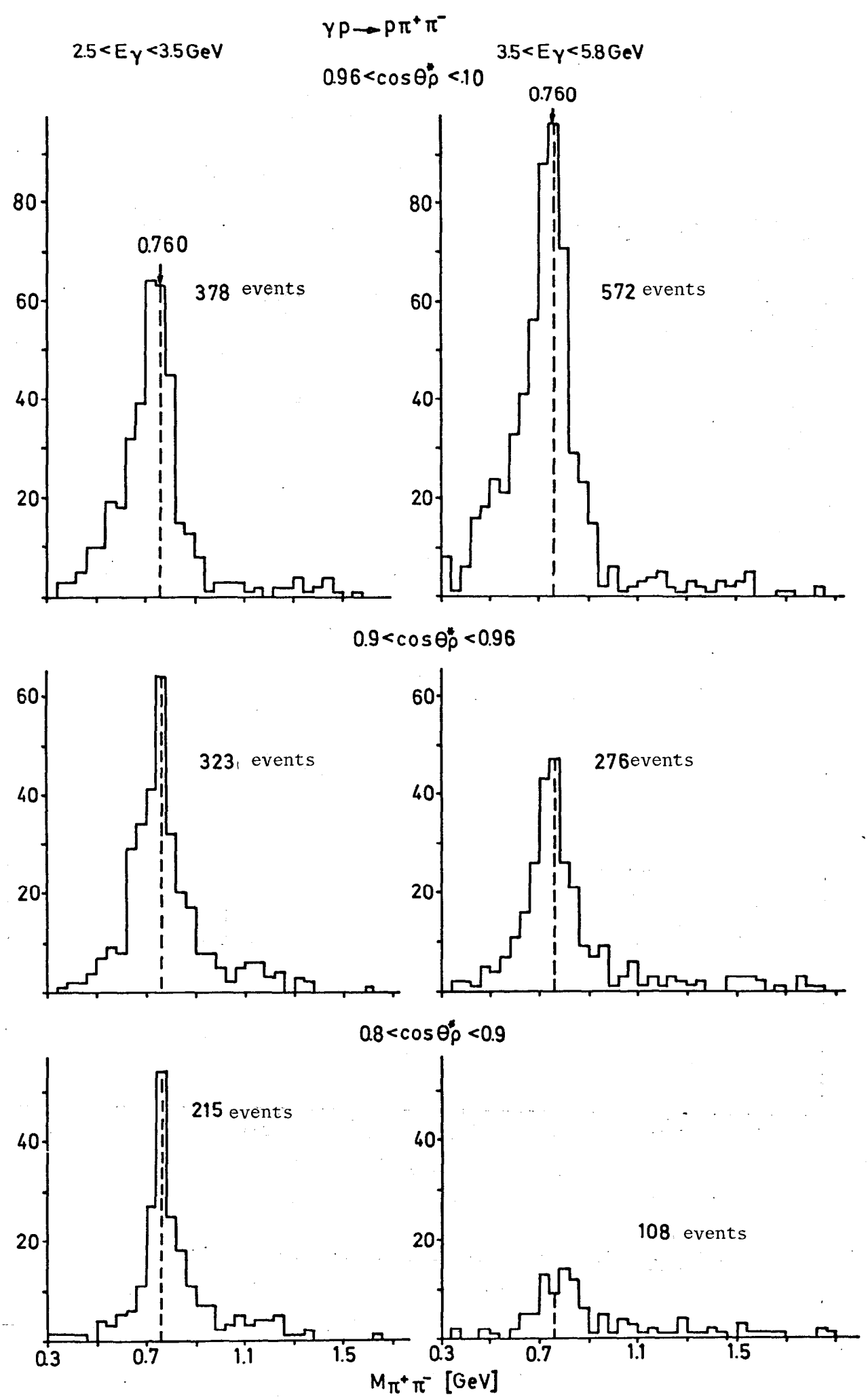

Fig. 25 Dependence of the $\pi^+\pi^-$-mass distribution on the production angle $\cos\theta^*_\rho$.

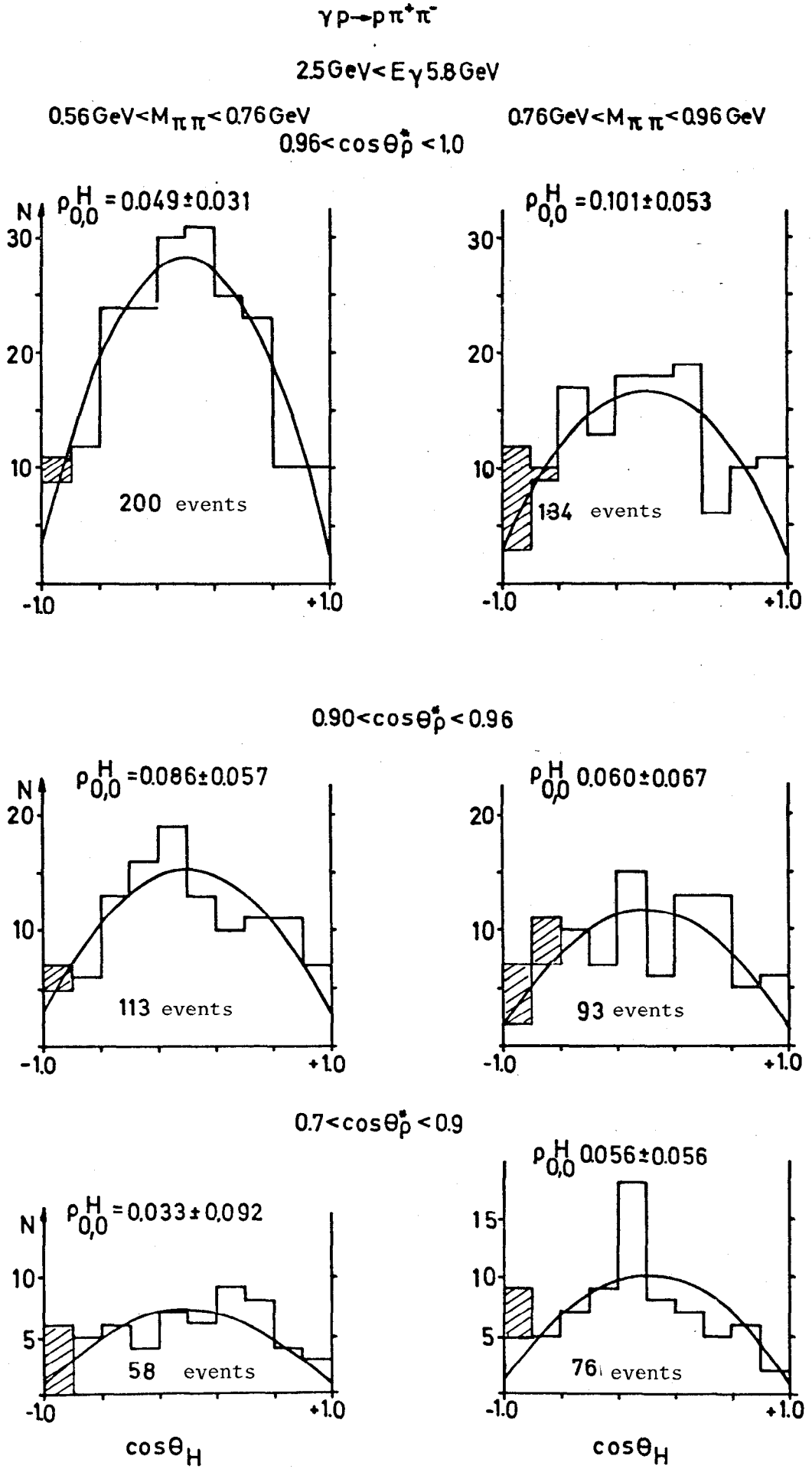

Fig. 26. Decay angle distributions W ($\cos\theta_H$) in the helicity system for two $\pi^+\pi^-$-mass regions.

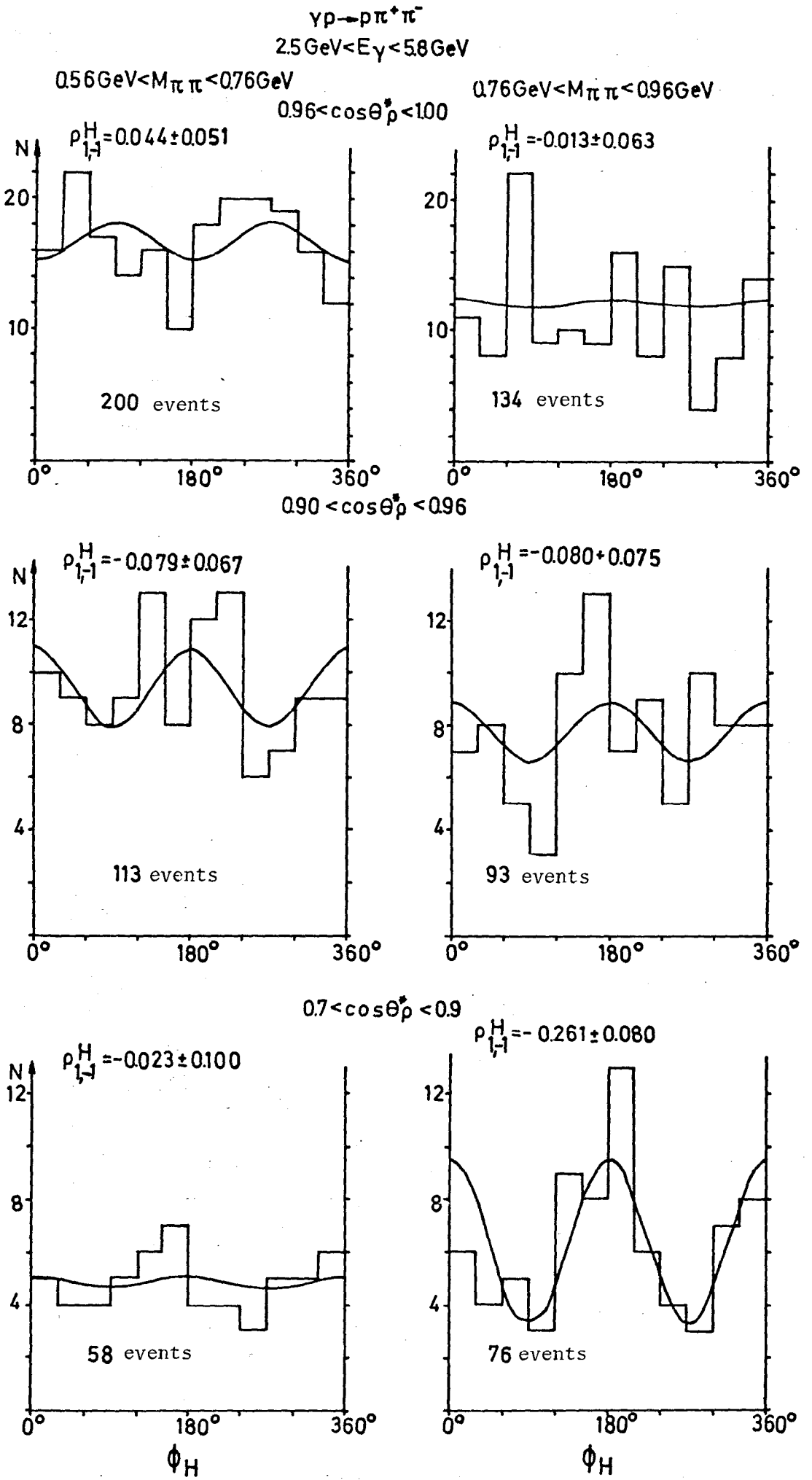

Fig. 27. Decay angle distribution W (ϕ_H) in the helicity system for two $\pi^+\pi^-$-mass regions.

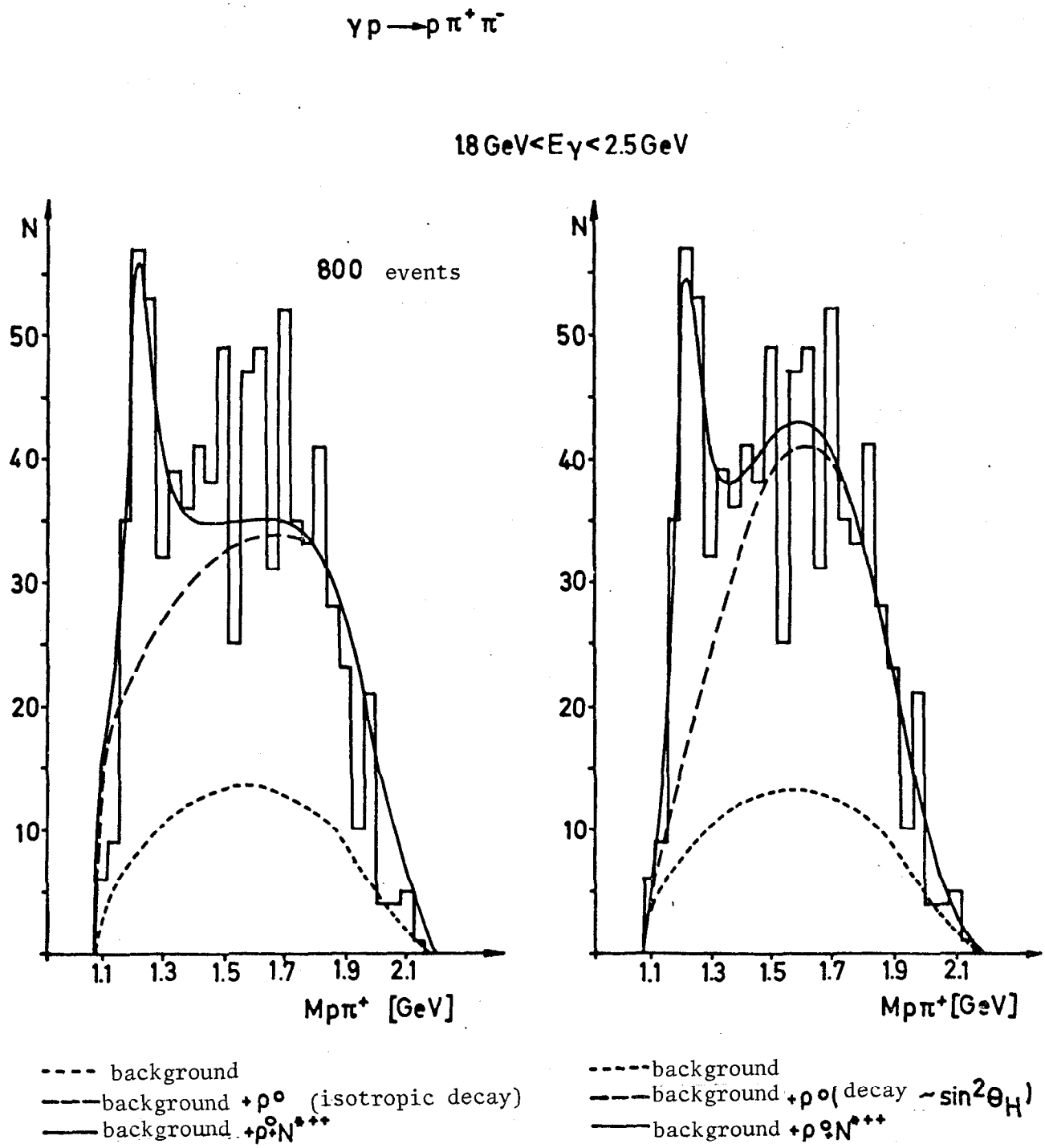

Fig. 28. Dependence of the fit in the $p\pi^+$-mass distribution on the decay angle distribution of the ρ-meson.